Interaction of Electrode Materials with Neuronal and Glial Cells

Von der Fakultät für Physik und Geowissenschaften

der Universität Leipzig

genehmigte

D I S S E R T A T I O N

zur Erlangung des akademischen Grades

Doctor rerum naturalium

Dr. rer. nat.

vorgelegt

von M.Sc. Alice Abend

geboren am 27.05.1991 in Leipzig

Gutachter: Prof. Mareike Zink

Prof. Athina Markaki

Tag der Verleihung: 23. Oktober 2023

Bibliographische Beschreibung

Abend, Alice

Interaction of Electrode Materials with Neuronal and Glial Cells

Universität Leipzig, Dissertation

123 Seiten, 172 Literaturangaben, 4 Abbildungen (exklusive des kumulativen Teils)

Referat

Steigende Zahlen von Patienten mit neurodegenerativen Erkrankungen sind ein überzeugender Grund, das menschliche Gehirn und seinen fortschreitenden Verfall zu untersuchen, wobei aber viele essenzielle biochemische Funktionen bisher noch nicht vollends geklärt sind. *In vitro* Forschung zur Hirnfunktion auf geeigneten Plattformen ist ein vielversprechender Weg, diese Lücke zu schließen. Eigenschaften der brain-machine Grenzfläche müssen erforscht werden, um neue Biomaterialien effektiv für lab-on-a-chip Anwendungen wie bspw. Multielektrodenarrays (MEAs) einzusetzen. Diese brain-on-a-chip Anwendungen können dazu dienen, die Zahl der Tierexperimente zu reduzieren, damit Forschung zu beschleunigen und Kosten zu senken. In dieser Hinsicht erfordert die Miniaturisierung von MEAs für eine detailliertere Messung von neuronalen Funktionen die Entwicklung von neuen Biomaterialien mit vorteilhaften elektrischen Eigenschaften. Die Wechselwirkung dieser Biomaterialien mit Zellen muss untersucht werden, um gute Zelladhäsion, Proliferation und elektrische Kopplung zu gewährleisten. Die vorliegende Arbeit dient der Charakterisierung der Wechselwirkung von humanen neuronalen Zellen und Gliazellen (neuronenartige SH-SY5Y und gliaartige U-87 MG Zellen) mit dem Elektrodenmaterial Titannitrid mit nanokolumnarer Oberfläche (TiN nano) und dessen Vorteile bezüglich elektrischer und bioaktiver Eigenschaften im Vergleich mit Gold (Au) und Indiumzinnoxid (ITO), welche derzeit für MEAs und Neuroelektroden verwendet werden. Das Ziel der Arbeit ist die Implementierung neuer aus der theoretischen Physik, Mathematik und Computerwissenschaft entlehnten Techniken, um eine bildbasierte Methode zu entwickeln, die auf minimalen Experimenten beruht und trotzdem wichtige Hinweise zur Biokompatibiliät eines Materials liefert. Das schließt die Analyse von Zellnetzwerken, Zellverteilung, Adhäsion und elektrochemischer Eigenschaften in mono- und co-Kultur ein. Dazu werden Autokorrelation, selbstlernende Algorithmen und die Analyse nächstgelegener Nachbarn eingesetzt, um einen Weg von klassischen biochemischen Assays weg zu einem rechnerischen Ansatz zu finden. Die Ergebnisse zeigen eine Überlegenheit von Tin nano als potenzielles Biomaterial für lab-on-a-chip Anwendungen und *in vivo* neuraler Stimulation. Die präsentierte bildbasierte Analysemethode für die Untersuchung von Zellverteilungen erweist sich als wertvolles Werkzeug für die Bewertung von Biokompatibilität. Sie ist universell einsetzbar für verschiedene Zelltypen und quantifiziert die Wechselwirkung von Zellen mit Biomaterialien.

Bibliographic Description

Abend, Alice

Interaction of Electrode Materials with Neuronal and Glial Cells

Universität Leipzig, Dissertation

123 pages, 172 references, 4 figures (without cumulative part)

Abstract

Rising numbers of patients with neurodegenerative diseases are a compelling reason to study the human brain and its progressive deterioration but many essential biochemical functions are still under investigation. Conducting research on brain function *in vitro* with suitable platforms is a promising solution to close these gaps. Characteristics of the brain-machine interface need to be investigated to effectively employ new biomaterials for lab-on-a-chip devices, such as multielectrode arrays (MEAs) for example. These brain-on-a-chip devices will potentially reduce the number of conducted animal experiments and therewith accelerate future research and reduce costs. In this context, miniaturization of MEAs for more detailed measurements of neuronal function calls for new biomaterials with advantageous electrical characteristics. The interaction of these biomaterials with cells needs to be investigated to ensure good cell adhesion, proliferation, and electrical coupling. This thesis aims to study and characterize the interaction of human neuronal and glial cells (neuron-like SH-SY5Y and glia-like U-87 MG cells) with the electrode material titanium nitride with nanocolumnar surface topography (TiN nano) and its advantages in terms of electric and bioactive properties compared to gold (Au) and indium tin oxide (ITO) which are currently employed for MEAs and neuroelectrodes. The overall goal of this study is the implementation of new techniques drawn from theoretical physics, mathematics, and computer science to establish an image-based method that relies on minimal experimental effort but nevertheless yields important evidence of biocompatibility of the material. Analysis includes the investigation of cellular networks, cell distribution, adhesion, and electrochemical properties in mono- and co-culture experiments. To this end, autocorrelation function, self-learning algorithms, and nearest neighbor analysis are deployed to move away from classical biochemical assays toward a more computational approach. Results show the superiority of TiN nano as a potential biomaterial employed for lab-on-a-chip designs as well as for *in vivo* neural stimulation. The proposed image-based analysis method for the investigation of cellular distribution turns out to be a valuable tool for the assessment of biocompatibility. It is universally applicable to cell types other than neuronal and quantifies the interaction of cells with biomaterials.

Contents

1. Introduction

The human brain is an extraordinarily complex system such that, unsurprisingly, its cellular architecture and function are not entirely understood. Surprisingly, some basic knowledge as the number of neurons and glial cells in different compartments of the brain is still under debate [1,2]. Thus, even seemingly easy questions concerning the brain are actually very difficult to answer. Diseases of the brain and the accompanying nervous system which are characterized by the progressive loss of neurons are called neurodegenerative disorders [3]. The number of patients diagnosed with neurodegenerative disorders such as epilepsy, Alzheimer's, and Parkinson's disease is growing such that neurological diseases are the leading cause of disability and the second major cause of death worldwide [4]. In the past 30 years, suffering from neurodegenerative diseases has increased in such a way that the number of deaths has grown by 39 % and disability-adjusted life years have increased by 15 % [4]. Aging is the primary risk factor for neurodegenerative disorders [5] and patient numbers will continue to rise due to an aging population caused by growing life expectancy [6,7]. The overlap of brain aging and the development of neurodegenerative disorders is still not fully understood [8]. The number of people affected by Alzheimer's disease is expected to double every 20 years to 81.1 million by 2040 and the number of patients with Parkinson's disease 50 years and older in the world's most populated areas will increase to 9.3 million by 2030 [9,10].

Research on neurodegenerative diseases is constantly developed further and treatment methods are improved. However, medical procedures are still mostly limited to weakening degeneration and symptoms instead of stopping or even reversing the neuronal damage [11,12]. Thus, early diagnosis is important but hindered due to the molecular and clinical heterogeneity of neurodegenerative disorders which is addressed by technologies to investigate the molecular pathways involved in the development of neurodegenerative diseases [13]. Recently, shared genetic and molecular pathophysiology mechanisms across major psychiatric and neurodegenerative diseases have been investigated to refine early treatment stages [14]. Research on neurodegenerative diseases has branched out and lately identified a role for T cells of the immune system for Alzheimer's disease, Parkinson's disease, and amyotrophic lateral sclerosis [15].

Great effort has been put into both *in vivo* and *in vitro* experiments with the aim to study the human brain and its progressive deterioration due to degenerative diseases but many essential biochemical functions are still under investigation [16]. *In vivo* animal models fail to represent the complexity of the human brain, lack crucial features, exhibit interspecies differences, are accompanied by high cost, low throughput, and optical non-transparency, and moreover, raise ethical concerns regarding animal experiments [17]. Mice and human brains are similar in terms of cell types and tissue architecture for evolutionary reasons but a recent study found that mice brain cells activate different genes in comparison with human neuronal cells

leading to the formation of receptors on different cell types resulting in diverse responses to drugs of human and mice cells [18,19]. *In vitro* culture models are easier to handle and offer the possibility to investigate cellular function and the cells' reaction to drugs for the development of new treatments [20,21]. On the other hand, many *in vitro* models are considered too simplistic for practical applications since they do not provide insights into behavioral responses or systemic responses such as organ-organ interactions [17]. Isolated *in vitro* cell cultures lack interplay with other cell types and do not account for cell-matrix interactions [22]. *In vitro* cultures can be appropriate for some, but not all, types of pharmacological studies as shown by Belle et al. comparing cortical rat neurons' *in vivo* and dissociated neurons' *in vitro* response to drugs [23]. However, *in vitro* experimental approaches permit the study of cellular interaction of neurons and glial cells with biomaterials which for example are employed as brain pacemaker devices for deep brain stimulation [24].

Neural probes need a stable interface between neural cells and biomaterial that guarantees reliable and selective recording and neural activation with minimal tissue damage and scarring [25]. The interaction of neuronal and glial cells with the surface of the neuroelectrodes is crucial for the brain pacemaker's functionality and therewith therapy success. Consequently, research on bioelectronics focuses on the development of materials and devices that enhance cell adhesion, proliferation, and physiological function, and yield stable long-term high-resolution transfer of electrical signals between the bioelectronic device and neuronal cells [26,27]. Employed electrode materials are often fabricated based on carbon and silicone compounds [28,29], but due to their high biocompatibility, chemical stability, and high electrical conductivity, noble metals such as gold and platinum are also often employed as electrode materials in conjunction with biological matter [30–32]. Neurons sense the surface topography of neuroelectrodes and are stimulated by the size, shape, and pattern of the biomaterial, which influence neuron adhesion, neurite alignment, and neurite formation [33]. A plethora of different surface topography designs have been developed and continuously improved to optimize the platforms for fundamental research on the development of brain cells as well as for practical biomedical applications. Such designs include for example microgrooves, micrometer-sized pillars, nanofabricated structures like nanowires, nanopillars, and nanotubes [34–41]. Novel materials in conjunction with bioengineering technologies enabled the research on biomimetic neural micro-environments [42,43]. These are complex neural 3D cultures composed of cells, biomaterials, and biological factors that model brain tissue architectures in the lab [42]. These systems are meant to bridge the gap between *in vivo* animal experiments and *in vitro* cell culture. These micro-environments are technically still *in vitro* culture systems but are developed with the aim to avoid the typical drawbacks of *in vitro* culture and provide some of the advantages of animal models, essentially making them the Swiss army knife of biomedical research. They can be used to study for example neurodevelopment or neuroregeneration processes.

2

In fact, brain-on-a-chip devices have proven to be beneficial to study neural function mimicking physiological interactions of different brain cell types [44–46]. Brain-on-a-chip has become an umbrella term for different research approaches to design engineered systems to cultivate neurons and observe their connections for a wide range of applications from pharmaceutical studies to research on neurodegenerative disorders [44]. The "brain" part in brains-on-a-chip can be derived employing *ex vivo* brain slices from vertebrates, *in vitro* derived brain organoids, or *in vitro* cultured neurons from human induced pluripotent stem cells. Lab-on-a-chip research is actually not limited to the investigation of the human brain but includes other tissue types such as heart, lung, kidneys, liver, bone, and skin [47–52]. Such organ-on-a-chip technologies combine microfabrication and tissue engineering to mimic important human physiologic functions and therewith prove to be useful for preclinical drug testing in terms of effectiveness and safety [53,54]. Research on brain-related lab-on-a-chip technologies has advanced considerably so they have been dubbed "mini-brain" models in a recent review article [55]. Neurons-on-a-chip technology is used to study neurite outgrowth, synaptogenesis, axon development, and network dynamics *in vitro* [56].

Multielectrode arrays (MEAs) as a type of brain-on-a-chip device are used for electrophysiological studies with electrically active cells which are found in neural networks such as the brain and associated nervous system and the cardiac system. MEAs usually consist of an array of micro-sized electrodes attached to the bottom of a multi-well plate. Cells are cultured on the electrodes for studies on cell differentiation and maturation, drug screening, toxicology studies, or modeling of neurodegenerative diseases. They offer the possibility to record and stimulate neuronal cells at different locations at the same time which renders them a widespread instrument to observe neuronal activity *in vitro* and *in vivo* [57]. More specifically, MEAs are used to observe cell health and function in a noninvasive way [58,59]. MEA biosensors detect changes in electrical current, impedance, and potential in electrophysiological studies. They are produced by microfabrication which includes methods like photolithography, screen printing, and laser patterning for example [60]. Proceedings in the manufacturing of MEAs nowadays make even 3D neural cell cultures and long-term recordings of up to 79 days possible [61,62]. Recent technological advances have even enabled large-scale neural recordings with single-neuron resolution which can be used in interoperative settings paving the way to comprehend the dynamics of clinically relevant neural activity [63].

The interaction of cells or tissue material with the surface of the MEA is a critical feature for the function of the biosensor. Only a stable and close attachment of the cells to the material's surface guarantees continuous and reliable electrical stimulation of cells and high-quality readouts in electrophysiological studies. A wide range of potential electrode materials has been explored in the search for biomaterials that provide a suitable brain-machine interface with focus on biocompatibility, mechanical mismatch, and electrical performance [64]. The Young's modulus of electrodes is usually in the range of several GPa but neuronal cells and

brain tissue are much softer which creates a mechanical mismatch at the brain-machine interface resulting in an inflammatory response of the cells and the formation of scar tissue leading eventually to the breakdown of signal recording and electrical stimulation of the biomedical sensor [65,66]. The dreaded glial scarring occurring at surgically inserted brain pacemakers for deep brain stimulation also impedes regeneration of neurons at the local surgical injury [67]. Research addresses this drawback with the development of soft and bio-inspired electrodes [68–71]. Cell adhesion also plays a major role in the functionality of biosensors and other biomedical applications [72]. Only stable coupling of the cells to the electrode material of MEAs enables long-term recording and stimulation. Various strategies to control neuronal adhesion have been developed with the goal of tissue repair and medical treatment in mind which rely on the understanding and controlling of the neuron-surface interaction [73].

Miniaturization of MEAs offers the possibility for more detailed cellular stimulation and neural recording on smaller length scales with denser arrays. But this downsizing of the electrodes gives rise to new requirements for materials like a lowered self-impedance since electrical impedance usually scales inversely with the electrode size, the smaller the electrode the larger is the impedance. Conductive polymers have been employed for this reason as they generally exhibit a lower impedance in comparison with inorganic materials [74,75]. However, also inorganic materials such as TiN for example can be used for the miniaturization of microelectrodes [76]. Further shrinking electrode sizes without the loss of detection sensitivity could be possible with TiN employing sophisticated surface morphologies which increase the material's surface area. The signal-to-noise ratio of MEAs also has a considerable influence on the quality of electrophysiological studies. Biocompatibility of biomaterials used for medical probes and implants is as important as it is time-consuming and laborious with standardized testing [77]. Safety assessment is often based on animal experiments or complex *in vitro* studies [78].

The goal of this thesis is to study and characterize the interaction of human neuronal and glial cells (neuron-like SH-SY5Y and glia-like U-87 MG cells) with different types of electrode materials, i.e. gold (Au), indium tin oxide (ITO), titanium nitride (TiN), and TiN with nanocolumnar surface topography (TiN nano), analyzing cellular networks, cell distribution, and adhesion in mono- and co-culture experiments. Suitability of electrode materials for applications in *in vivo* medical treatment of patients suffering from neurodegenerative disorders as well as *in vitro* lab-on-a-chip studies will be explored. The results of the individual experiments conducted for this thesis could hint at possible biocompatibility of the electrode materials. Diverse challenges like glial scarring at the interface between brain tissue and neuroelectrode after surgical treatment but also miniaturization of MEAs need to be solved. This thesis does not aim to offer complete solutions to these giant challenges but I want to demonstrate new methods and consider biological systems from a physics point of view. The proposed mathematical and physical methods are used to gain insight into cellular organization and pattern formation. I combine the results from these

4

novel approaches with data collected from tried and true methods such as single-cell adhesion force spectroscopy to understand cellular behavior at the interface with a biomaterial. I pursue a novel approach to analyze bioactivity of electrode materials using experimental data in conjunction with computational methods. This process is comparably fast, inexpensive, easy, and transferable to other applications. I combine diverse scientific disciplines borrowing knowledge from physics, mathematics, biology, and computational science to leave worn-out tracks and explore new paths.

2. Background

2.1. Neuronal Cells

Brains consist of different types of cells that do not only coexist but also communicate and form functional networks. These cells can be broadly categorized as neurons and glial cells. Neurons are responsible for environmental sensing and signal transduction in the nervous system or in other words "thinking". Glial cells on the other hand fill a rather supportive role for the neurons, providing insulation and nutrition for example. But the opinion of the scientific community on the characterization of glial cells viewed solely as support providers for neurons has started to crumble due to recent scientific studies which indicate a more influential role of glial cells than only neuronal support [79]. Glial cells are not regarded as passive support cells or even "packing material" to fill the gaps in the network made of neurons anymore.

Generally, human brains are made up of equal quantities of both cell types, i.e. about 85 billion neuronal and non-neuronal cells. However, different parts of the brain have different ratios of neurons to glial cells. The gray and white matter of the human cerebral cortex consists of about 20 % neurons and 80 % non-neurons, whereas we find the inverse ratio in the human cerebellum [2]. Hence, cellular architecture seems to be important for the compartmentalization and therewith function of brains. Neurons and glial cells form networks to perform specific tasks and complement each other's functions.

Information presented in this chapter is, if not stated otherwise, textbook knowledge and can be found in M. Bear's "Neuroscience Exploring the Brain" [80], C. Molnar's "Concepts of Biology" [81], and E. Kandel's "Principles of Neural Science" [82].

Neurons

Nerve cells, also called neurons, are the signaling units of the nervous system. They are able to receive and send electrical signals from other neurons which enables communication in the neuronal network. A schematic representation of a neuron is shown in Figure 1. The cells consist of a cell body (soma) containing a cell nucleus, endoplasmic reticulum, Golgi apparatus, mitochondria, and other cell organelles. Neurons generally form two types of processes: short dendrites and a single long axon. Dendrites resemble tree branches fanned out around the cell's soma, hence their name dendrite derived from the ancient Greek dendron meaning tree. Neurons use them mainly for signal reception. The axon is a long tubular structure extending far out of the cell soma which branches out at the end. It is used to carry signals to other neurons sitting at a distance from the sending neuron. The interaction site of neurons where the axon meets a dendrite or soma of another neuron is called the synapse. The electrical signal is converted into a chemical signal at the synapse releasing neurotransmitters that can cross the synaptic cleft (gap between the two

meeting cells). The incoming chemical signal is reconverted into an electrical signal at the receiving neuron and can be sent further to other cells or triggers an action in the receiving cell. The sent electrical signals, also called an action potential, can travel over considerable distances of 0.1 mm up to 1 m. All physiological signals and stimuli, such as vision and odor, for example, are transmitted in the nervous system by action potentials. The information is always carried in the same form no matter the type of information that needs to be transmitted. The only difference is the pathway that the signal takes in the nervous system. That is a key principle of brain function. Incoming electrical signals are categorized in the brain by the specific pathway on which they are carried which enabled us to differentiate between sensations of sight and smell for example.
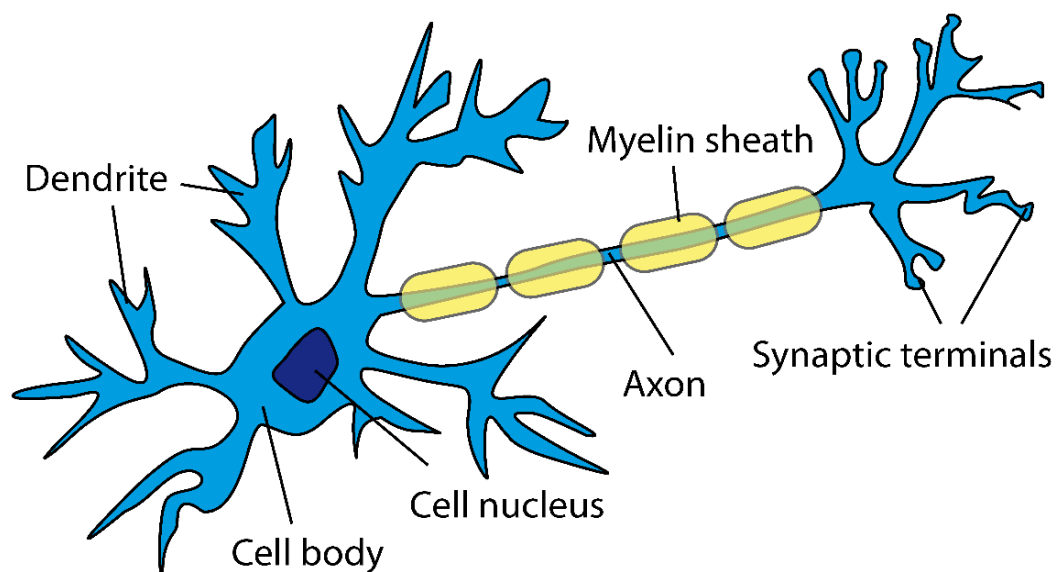

Figure 1: Schematic representation of a neuron including characteristic components.

Neurons are a rather diverse class of cell types and the classification of subtypes is based on several different features of the cells. Neurons are categorized into unipolar, pseudounipolar, bipolar, and multipolar for example according to the number of their processes also called neurites (axons and dendrites). See Figure 2 for an illustration. Classification based on the arrangement of dendrites into stellate cells (stars) and pyramidal cells (pyramids) or according to the number of spines on dendrites into spiny and aspinous is possible. Another option to classify neuronal cell types is the cell's function in the nervous system. Sensory neurons transfer information from the peripheral regions of the body to the central nervous system and are also called afferent cells. The opposite, efferent cells, carry information from the central nervous system to the motor organs of the body (muscles and glands for example). Hence, they are named motor neurons. The third type is named interneuron and its main task is to connect neurons with other neurons for extended signal transfer. The different types of neurons overlap and form even more subtypes. Recently, new studies revealed the possibility to categorize neurons according to RNA

sequences which makes the entire neuronal classification system even more sophisticated [83].
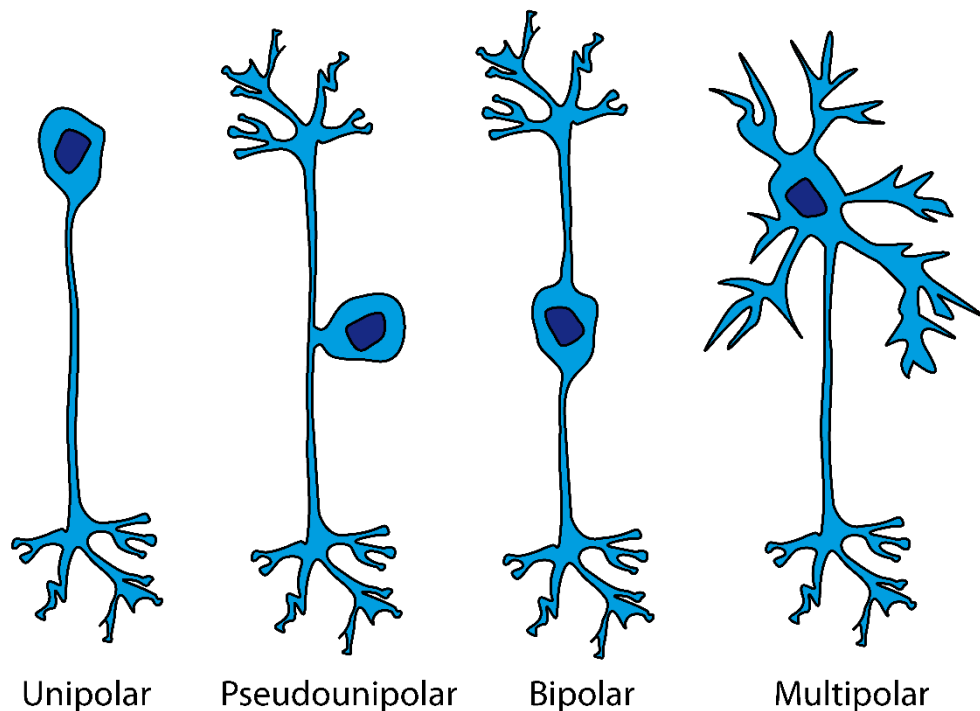

Unipolar   Pseudounipolar   Bipolar   Multipolar

Figure 2: Classification of neurons based on the number of processes.

Glial Cells

This neuronal cell type is named after the ancient Greek word for glue and was long believed to only provide a supporting role for neurons in the nervous system. They do not really glue neurons together but rather surround them and form some kind of matrix for them. Glial cells have different morphological characteristics in comparison with neurons. They exhibit different cell membrane properties which explains why they are not electrically excitable and they also lack the dendritic morphology of neurons. Glia supply nutrients and oxygen to neurons, provide electrical insulation, destroy pathogens, and remove dead cells. Their proper functions are vital such that many brains tumor are caused by mutations in glial cells.

Glial cells are categorized according to their function in the nervous system. A schematic representation of different types of glia cells is shown in Figure 3. Astrocytes mostly fill the extracellular space between neurons in the brain and regulate chemical content for example by enveloping synapses and inhibiting the spread of neurotransmitters or removing neurotransmitters from the synaptic cleft. They also regulate the concentration of ions and chemicals in the extracellular fluid. Astrocytes form the blood-brain barrier, blocking toxic compounds from entering the brain and therewith filling a vital role in our life. Myelinating glia, like

oligodendrocytes and Schwann cells, form membrane layers insulating neurons' axons which are called myelin sheaths. Myelin promotes the speed of signal propagation along the axon of neurons. Satellite glia are found in the peripheral nervous system and provide structure and nutrient supply for neurons there. There are also glial cells that serve macrophage functions, degrading dead cells and protecting the brain from entering microorganisms. These are called microglia.
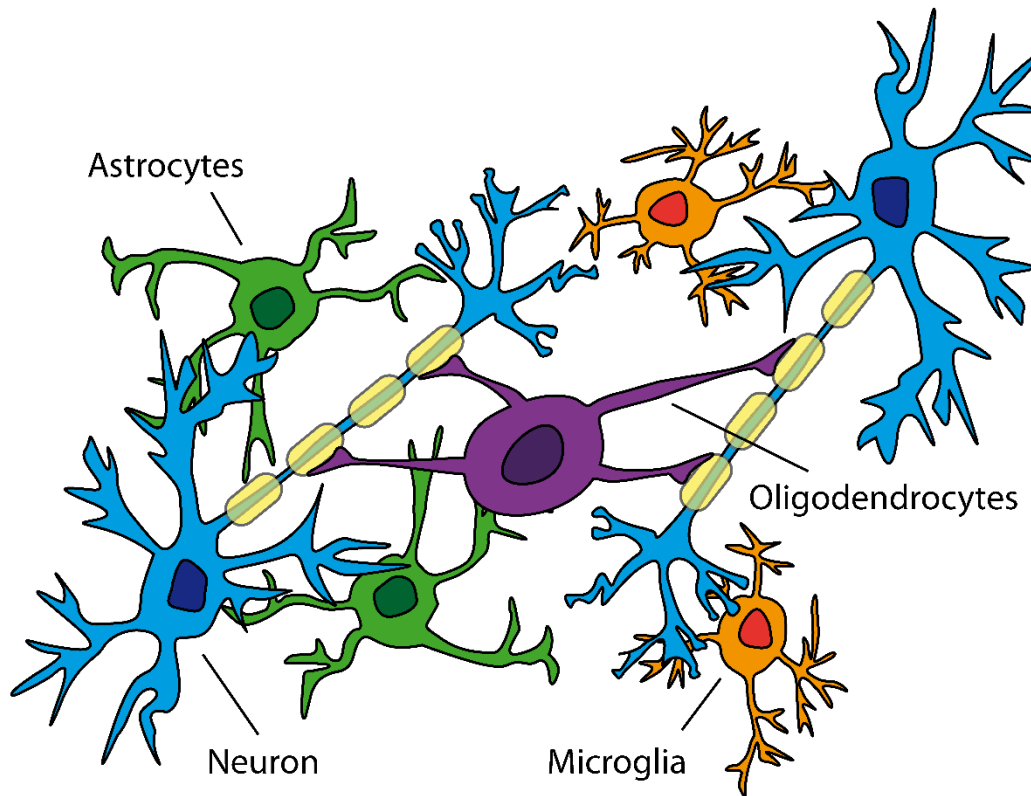

Figure 3: Schematic representation of different types of glial cells. Astrocytes are shown in green, oligodendrocytes in purple, and microglia in yellow.

Overall, there exists quite a range of glial cell types but their diversity is much lower in comparison to neurons which exhibit great variability in morphology and distribution [84]. Non-neurons are much more evolutionary conserved and constrained in their development. Current research is working on the answer to the question of why that is the case. Possibly, restricted glial variation is simply a consequence of late glial cell differentiation or it is due to physiological constraints in the sense that small changes in glial cells could lead to severely compromised brain function. This would emphasize the view of glial cells as more than just glue holding neuron networks together.

2.2. Cell Adhesion and Biocompatibility on Biomaterials

Biomaterials

Biomaterials are generally defined as non-living materials which are designed to be used in conjunction with biological systems. There is also an IUPAC definition describing biomaterials as "materials exploited in contact with living tissues, organisms, or microorganisms" [85]. A comprehensive overview of biomaterials is available from W. Wagner in "Biomaterials Science – An Introduction to Materials in Medicine" [86] from which information presented in this and the following section is drawn if not stated otherwise.

The research field of biomaterials science addresses both diagnostics and treatment and is about 70-80 years old. Nowadays, biomaterials come in many shapes and sizes and are made of a variety of materials such as metals, ceramics, polymers, and hydrogels for example. Biomaterials are used for medical disease treatment but also for *in vitro* cell culture research and assays. The common denominator of these systems is the interface between artificial (or natural but modified) materials and biological matter. The specific properties of biomaterials are always governed by their intended application. Implants for bone structures might need to be more rigid than devices inserted into the brain for instance. Also, specific cell types interact differently with a material's surface depending on cell shape and morphology. Endothelial cell types tend to grow in dense cell layers whereas neuronal cells are more likely to form mesh-like network structures with nodes. Cells need biomaterials that enhance or at the least maintain their physiological morphology, growth patterns, and function. Concepts have evolved over time and biomaterial implementation has come from simply adapting industrial materials over the design of new passive materials with desired physical and chemical properties to fabrication of bioactive substrates which trigger biological response and self-assembling materials to integrate even more functionalities and allow *in situ* assembly or disassembly.

Biocompatibility

The "ability to be in contact with a living system without producing an adverse effect" [85] is known as biocompatibility. The concept of biocompatibility is central to the development of biomaterials since materials can only become biomaterials because they are biocompatible. This common definition of the term biocompatibility is in principle not wrong, but rather impractical for most applications since it is quite blurry. Can we answer the question on biocompatibility of a certain material with a simple yes or no or is there a biocompatibility spectrum? Biomaterials are not inherently biocompatible since it all depends on the interaction with biological matter and different cell types might react differently to the chosen material. Hence, not only is the answer to questions of biocompatibility generally not binary, but also the specific application of the material plays a role. Additionally, time and intensity

11

of the interaction of biomaterial and biological matter also influence biocompatibility. Cells sense their environment and signal transduction pathways are triggered in contact with biomaterials to evaluate whether the material provides suitable conditions in accordance with the cells' normal biological activity. Cells can only survive on non-toxic materials that do not trigger immunological rejection [87–89]. This is the absolute minimum quality that a biomaterial needs to provide. On top of that, materials are required to yield a suitable performance depending on the intended use of the biomaterial device. These properties need to be tested before the application of a biomaterial in medical devices or *in vitro* assays to ensure both patient safety and robust results in cell culture experiments. Otherwise, adverse effects induced by the employed materials could lead to serious consequences.

In vitro biocompatibility tests comprise cytotoxicity assays, cell adhesion measurements, and studies on cell activation and death. Tests are categorized as direct contact cell culture, extract dilution, and indirect contact diffusion. Generally, direct cell culture methods are used to assess biocompatibility of a new material. Cell types for these experiments are chosen according to the later intended use and application field of the material. Results are compared with positive or negative control materials. Extract dilution tests require solvent extraction of the biomaterial and are used to gain knowledge on cytotoxicity for regulatory compliance. These first tests are followed by more application-specific analyses. A drawback of such *in vitro* tests is the usually comparably short cell culture duration. This could result in problems for medical applications of biomaterials as long-term implants but might not affect short-term *in vitro* applications of biomaterials. *In vitro* tests of biomaterials are followed by *in vivo* assessment of biocompatibility with the main goal to examine the functionality of a substrate for its intended use. The analysis is twofold: The general tissue biocompatibility is investigated and the applicability of the final device is tested. *In vivo* tests generally require animal models [90,91].

Characterization of the surface of biomaterials including parameters such as topography and roughness is a mandatory step towards the optimization of the materials for their intended application. Cellular adhesion on the biomaterial's surface is a vital factor for biocompatibility and finding correlations between cellular behavior and material surface properties propels biomaterials science forward. New insights into the interaction of cells with biomaterials give rise to the opportunity to tune the material's physic-chemical properties for physiological cell function [87,92].

Cell Adhesion and Bioactivity

For biomedical research, cell-substrate adhesion plays a major role in medical implant as well as lab-on-a-chip designs. The functionality, applicability, and longevity of the device depend on the interaction of cells with the biomaterial surfaces which is governed by cell adhesion processes. Different applications of biomaterials give rise to specific requirements for cell adhesion. Sometimes strong cellular adherence is desired for example in scaffolds for tissue regeneration. However, applications like

artificial heart valves need to be designed in such a way that blood and plasma cells do not stick to the device. Here, strong cellular adhesion would lead to thrombosis and embolism [72,93]. In case of neuronal tissue, surface topography, stiffness, and electrical properties of biomaterials play a vital role in cell adhesion and neurite outgrowth [94].

Cell adhesion is a dynamic process that connects a single cell with its environment. Generally, one can distinguish between cell-cell adhesion and cell-matrix adhesion. Cell-cell adhesion describes the attachment of one cell to another cell and cell-matrix adhesions occur wherever a cell adheres to the extracellular matrix (ECM). Ligand proteins in the plasma membrane of a cell link its cytoskeleton to an adjacent cell or the ECM. Adhesion is a vital property of cells since it does not only hold multicellular organisms together but also serves as a means for intercellular signal transduction pathways which in turn regulates for example gene expression, cytoskeletal dynamics, cell differentiation, and survival [72,87,92].

Cell adhesion is crucial for communication and regulation of cells and therewith influences the development and sustenance of tissues. Abnormal cellular adhesion behavior is associated with various diseases such as arthritis, osteoporosis, atherosclerosis, and even cancer [72,95–98].

The ECM proteins found in *in vivo* tissue are missing on biomaterials made of metals or ceramics. Hence, cells usually deposit these proteins, such as fibronectin and laminin for example, onto the substrate surface enabling the cells to form adhesion spots via anchoring ligands in their plasma membrane. Early adhesion can occur in seconds via focal complex formation when cells get in contact with biomaterials. Mature adhesion complexes are formed subsequently from this soft binding step linking cellular adhesion receptors in the plasma membrane to ECM molecules [99,100]. Nascent adhesions are formed within some ten seconds and these early adhesions mature into focal adhesion points on a time scale of minutes [99,101–105].

More specifically, a type of cell adhesion molecule named integrin is generally responsible for cell-ECM adhesion. Integrins are transmembrane proteins linking the extracellular matrix to the intracellular cytoskeleton of a cell. The type of cell-ECM junction is called focal adhesion if the integrin binds to actin filaments in the cells and hemidesmosome if integrins are attached to intermediate filaments. Integrins have an active and a passive state and need to be activated before adhesion points can form. This can happen via inside-out and outside-in activation whereby extracellular matrix proteins bind to integrins from outside of the cell or intracellular activator proteins such as talin, in case of focal adhesions, for example, attach to the integrins from the inside of the cell membrane. Either way, integrins undergo conformational changes and switch from their inactive to an active state enabling signal transduction in both ways across the plasma membrane. Complex protein assemblies form on the intracellular tail of integrins upon activation. Cell-ECM junctions involving integrins are capable of mechanotransduction, i.e. cells can sense and also respond to mechanical cues across the junction. Processes involved in cellular adhesion play a

much larger role in cell function than simple mechanical attachment. Integrins help cells to convert mechanical and biochemical signals and therewith enable them to actively interact with their environment. Assembly and disassembly of cytoskeletal links inside the cell and formation as well as cutting off of extracellular attachments on the outside allow the cell to migrate. This dynamic adhesion process also involves the clustering of integrins upon their activation to form large complex structures resulting in mature cell-ECM junctional complexes. The "cell adhesion model" states that the strength of cellular adhesion is related to the number of chemical bonds on its membrane surface [106–109].

In vitro adhesion of cells to a substrate is a dynamic process that can be divided into three stages: initial attachment of the cell to the substrate, flattening and spreading of the cell, and formation of focal adhesion junctions involving organization of the cell's actin fibers. The cell sediments on the substrate and electrostatic interaction between the cell and biomaterial occur. Afterward, the cell starts to form integrin bonds with the substrate surface forming single receptor-ligand pairs and the cell body flattens and starts to spread. The last stage is characterized by fully matured focal adhesions and a maximum spread cell area accompanied by reorganization and distribution of the cell's actin cytoskeleton [72,110].

Cell adhesion is studied with a variety of techniques focusing on different aspects of the mechanical interactions between cells and the ECM [72,109]. Firstly, attachment and detachment events need to be distinguished. Cell attachment studies, as their name already suggests, investigate the bond formation between cells and the ECM on a substrate whereas detachment experiments focus on the load application to remove cells from a substrate. Secondly, cell adhesion studies can be performed on either single cells or entire cell populations. Experiments concerning cell attachment processes are for example carried out using polyacrylamide gel-based traction force microscopy, micropatterning technique, microfluidics, and wash assays. Cell population detachment events are measured with centrifugation, flow chambers, or using spinning disk techniques. This thesis involves single-cell detachment experiments with a focus on whole-cell detachment instead of single-bond breaking. Here, atomic force microscopy (AFM)-based single-cell force spectroscopy has been used to investigate detachment force and work for both neuron-like and glia-like cells on electrode substrates with different adhesion times [111–113].

Atomic Force Microscopy

Atomic force microscopy (AFM) is a multifunctional tool that can be used for imaging, rheological measurements, and adhesion experiments on both hard- and soft-matter specimens [114–124]. A comprehensive overview of atomic force microscopy functions and applications in a biological context is available from V. Morris's "Atomic Force Microscopy for Biologists" [125]. Briefly, the working principle of an atomic force microscope is based on a tiny (micrometer-sized) leave spring made of metal called cantilever that interacts with the specimen. The cantilever is mounted on a

piezo element and can probe or manipulate the sample. The light beam generated by a laser diode in the AFM is pointed to the tip of the cantilever and is reflected onto a quadrant photodiode. If the cantilever exerts a force on the specimen or the other way around, the beam path changes, and the reflection spot on the photodiode is displaced. Hence, a registered signal at the photodiode is associated with a deformation of the cantilever due to an exerted force. The deflection force F needs to be calculated from the deflection signal of the photodiode (voltage u) using Hooke's law assuming a linear relation:

$$F = k \cdot s \cdot u$$

(1)

where k is the spring constant and s is the sensitivity of the cantilever. These quantities can be derived from the calibration of the cantilever before the experiment using for example the thermal noise technique [126,127].

For this thesis, single-cell force spectroscopy measurements were performed to study the adhesion of neuronal cells on electrode material substrates. To this end, a single cell (neuron-like or glia-like cell) was attached to the tip of a cantilever using Poly-D-Lysine and then pressed for either 5 s or 30 s onto an electrode material substrate (gold, indium tin oxide, titanium nitride). After this adhesion time, the cantilever with the attached cell was lifted up again in the z-direction and the maximum force and work to completely detach the cell from the substrate was extracted from the resulting force-distance curves.

2.3. Cell Networks

Organization of Cells

The organization of cells and formation of growth patterns on biomaterials is an indicator of the interaction and response of the cells to the material. Hence, it can be viewed as a marker for biocompatibility. Materials that are biocompatible will promote proliferation and formation of *in vivo*-like cellular organization of the specific cell type. The desired cellular organization on the surface of biomaterials always depends on the specified application of the material or device. Biomaterials intended to be used as implants for example should promote the organization of cells that is comparable to healthy *in vivo* cells to yield optimal tissue regeneration at the interface between the implanted biomaterial and biological matter. Otherwise, scar tissue might develop at the implantation site diminishing the functionality of the device or even rendering it essentially useless. This phenomenon can occur after the implantation of pace makers for deep brain stimulation for example when glial cells form an insulating layer covering the implanted electrodes. A biocompatible electrode should promote the growth and reorganization of neurons into physiological patterns conserving healthy cytoarchitecture and brain function.

Complex signal transduction in the nervous system is enabled by the connections formed between single neurons via synapses and axonal pathways. The neurons need to be organized in local circuits which communicate between different brain regions. Disturbance and damage of this structural network usually lead to cognitive dysfunction. Hence, the organization and formation of healthy growth patterns are of great importance for neuronal cells. Neuronal structures are nowadays studied in depth merging neuroscience with the science of complex networks. Not only the elementary components of the systems, i.e. the cells but also the interactions between these components have come into focus. A comprehensive overview of the topic can be found in the literature for example in O. Sporn's "Networks of the Brain" [128] and A. Fornito's "Fundamentals of Brain Network Analysis" [129].

K-means Cell Clustering Algorithm

Machine learning algorithms can be utilized to analyze patterns in networks. Networks of neuronal cells grown on biomaterials are characterized by the positions of the individual cells on the substrate. Unsupervised machine learning algorithms can now identify agglomerations of cells in the network and group them into clusters. Hence, these algorithms can be used to compare growth patterns and spatial cellular distributions in a standardized way reducing human errors in the analysis. The position of every single cell is treated as a data point on a 2d plane.

An unsupervised machine learning algorithm based on K-means clustering is implemented in the work of this thesis to assess cellular distribution and growth patterns. The algorithm is used to sort data into a predefined number of clusters [130–132]. It randomly initializes data points as cluster centers (centroids) and then iteratively assigns data points to the cluster whose centroid has the shortest Euclidean distance to the data point. During each cycle, the centroids are recalculated based on new data point assignments to clusters. This process continues until the algorithm attains a stable situation, meaning the centroids do not move anymore and the reassignment of data points to the clusters stops. More specifically, the algorithm tries to minimize the so-called within-cluster variation W. It is defined as the sum of squared distances between data points and their corresponding centroid:

$$W(C_k) = \sum_{x_i \in C_k} \|x_i - \mu_k\|^2$$

$$(2)$$

where x_i is the position of a cell (data point) in cluster C_k with μ_k as the mean value of all data points in this cluster. The sum of all within-cluster variations for each cluster in the data set is defined as the total within-cluster variation:

16

$$totW(K) = \sum_{k=1}^{K} W(C_k)$$

<div align="right">(3)</div>

This sum needs to be iteratively minimized until a stable point is reached. K (uppercase) is the total and optimal number of clusters in the data set and needs to be specified by the user before running the sorting algorithm. The lowercase k serves as the index of summation for the clusters in the above-mentioned equations. The K-means algorithm is named after the number of clusters K into which data is sorted. Selecting the appropriate value for the optimal number of clusters for a given data set is challenging but vital to obtain meaningful results from a K-means algorithm. The so-called elbow method can be used to solve this problem.

The elbow method is a heuristic approach to identifying the optimal number of clusters in a data set. It makes use of the fact that the total within-cluster variation $totW(k)$ decreases for an increasing number of clusters k. The total within-cluster variation is calculated for several different choices of cluster number k. This method looks for an "elbow", i.e. a kink, in the graph of total within-cluster variation as a function of the number of clusters. The elbow marks the point where the decrease of the within-cluster variation slows down. This is considered to be the optimal number of clusters K for the given data set. The elbow method is based on the work by Thorndike [133]. But since this approach is only heuristic, the elbow method is not always a reliable source of information for the optimal number of clusters in data sets. Hence, backup procedures are needed to verify the results drawn from the elbow method.

Another possible approach to identify the optimal number of clusters in a data set is based on gap statistics. This method relies on the comparison of the within-cluster variation of real data with results from hypothetical uniform data sets [134]. The so-called gap value $Gap(k)$ is calculated from the total within-cluster variation of the real data set $totW(k)$ and the same quantity drawn from fabricated uniformly distributed data sets $totW_{\mathrm{uni}}(k)$:

$$Gap(k) = \log totW_{\mathrm{uni}}(k) - \log totW(k)$$

<div align="right">(4)</div>

The total within-cluster variation of the uniform data $totW_{\mathrm{uni}}(k)$ is extracted from a simulation of 50 individual uniform data sets of the same size as the real data set. The standard error $s(k)$ associated with the generated data sets is also measured. Finally, the optimal number of clusters K is obtained from this equation:

$$K = \min\{k \in \{1, \ldots, k_{\mathrm{max}}\}\colon Gap(k) \geq Gap(k+1) - s(k+1)\}$$

<div align="right">(5)</div>

Following Tibshirani et al. [134], for this thesis $s(k)$ is based on the standard deviation $sd(k)$ of the 50 Monte Carlo simulated data sets as follows:

$$s(k) = \sqrt{1 + \frac{1}{50}} \, sd(k)$$

(6)

Practically, the smallest k value for which equation (5) holds is the optimal number of clusters K. Hence, the Gap value is maximized so that $Gap(k)$ lies within one standard deviation from the Gap value at $k + 1$.

Once the optimal number of clusters is found for a given data set, the K-means algorithm can sort the data points, i.e. positions of cells grown on biomaterials for this thesis, into their associated clusters. It is advisable to check and verify the final sorting of data points into clusters. Just because the K-means algorithm starts with the correct number of clusters as input, the outcome of the algorithm does not necessarily yield the best possible sorting of data points. There are several procedures to review the quality of K-means results such as the silhouette method.

The silhouette method is based on the work of Rousseeuw [135] and assigns a quantity called silhouette coefficient to the generated clusters that measures the clusters' tightness and separation. The graphical display shows which data points lie well within a cluster and which ones are outside of clusters or at their edge. It is a tool to compare the relative quality of clusters. The silhouette coefficient $SilCoef$ is calculated as following for each data point i:

$$SilCoef(i) = \frac{x(i) - y(i)}{\max\{x(i), y(i)\}}$$

(7)

where $x(i)$ is the smallest mean distance to a data point in any other cluster and $y(i)$ is the mean intracluster distance. This equation yields values from -1 to +1. -1 means the data point is assigned to the wrong cluster, 0 corresponds to the data point sitting right at the edge of a cluster, and +1 represents a data point assigned to the correct cluster. Hence, high-quality cluster results of the K-means algorithm are represented by a high average silhouette coefficient. Running the algorithm with various start values of a number of clusters k and plotting the mean silhouette coefficient of the data set as a function of the number of clusters k is also an additional way to verify the choice of the optimal number of clusters.

Radial Autocorrelation Function

The radial distribution function is a key quantity in statistical mechanics and is used for example to measure the correlation between atom or molecule pairs. It is built on the hard-sphere model which describes model particles of fluids and solids as hard impenetrable spheres that cannot overlap spatially. The radial distribution function

which is also called pair correlation function quantifies how particle density varies depending on the distance from the reference particle.

In other words, this function yields the probability of finding a second particle at a distance r from the reference particle. This is illustrated in Figure 4 where the black sphere depicts the reference particle and three blue particles are found at a distance r. This principle can also be applied to pixels in a binary image instead of hard spheres. The pair correlation function can then be used to measure the probability of finding a black pixel at a distance r from the reference black pixel on a white background. This yields information on the typical object size and distance between objects. Here, objects are not the individual pixels in an image but rather pixel agglomerations as shown in Figure 4.
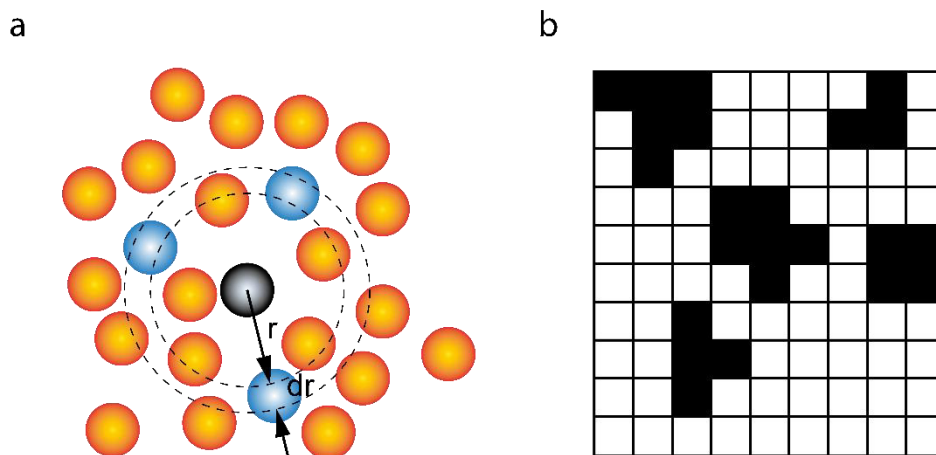

Figure 4: Illustration of radial distribution function using the example of a (a) hard sphere model and (b) pixel graphics.

Spatial radially averaged autocorrelation can be used to measure the spatial distribution and organization patterns in an image. Historically, Berryman and Blair proposed the method to analyze porous materials via image processing techniques combined with Fourier transform and radially averaging methods [136,137].

For the work of this thesis, spatial radially averaged autocorrelation has been applied to fluorescent images of cell nuclei on biomaterials. Hence, the black pixel agglomerations on white background represent the nuclei of either neuron-like or glia-like cells. As the autocorrelation function exhibits typical object sizes and distances for each image, it measures the probability of finding cell clusters and their distribution in the experiments. Cell agglomerations are characterized by small or no gaps at all between the cell nuclei in an image. Thus, the closer the cells sit together, the more probable is it to detect the cell cluster as a single large object instead of individual small cell nuclei. A comprehensive illustration of the radially averaged autocorrelation function and its meaning for evenly distributed data and clustered data is available from Baker et al. [138]. Briefly, the first minimum of the function gives an estimate of the typical object size in the image and the first maximum depicts

the typical object spacing. Homogeneously distributed objects result in a pronounced undulation of the curve. More heterogeneous data, i.e. various object sizes and non-homogenous spatial distribution is represented by a rather flat curve with very subtle minima and maxima.

Nearest Neighbor Analysis

Nearest neighbor analysis is another tool in physics and material sciences to study for example structure and organization of materials on the molecular or even atomic level. The nearest neighbors of each atom in a material are identified and bond angles, as well as spatial arrangement of atoms, are determined. The same method is also applied in theoretical physics to study for example lattice models with particles and analyze phase transitions, energy, entropy, and thermodynamic quantities. Additionally, nearest-neighbor models play a role in Monte Carlo simulations and density functional theory. Thus, it is a versatile physical method to understand complex systems in condensed matter physics, statistical mechanics, and even quantum field theory. However, applications in a biological context to identify spatial cellular distribution and network patterns are also feasible.

In the context of this thesis, nearest-neighbor analysis is used to measure the distribution of co-cultured neuron-like and glia-like cells grown on electrode biomaterials based on fluorescent images. The center-to-center distance d of a cell nucleus to the next nearest cell nucleus is computed for every cell using the Euclidian norm:

$$d = \sqrt{(x_1 - x_2)^2 + (y_1 - y_2)^2}$$

$$(\, 8 \,)$$

Where x and y denote the positions of data points (here centers of cell nuclei) in two dimensions. This technique provides a numerical value that reflects to which extent cells cluster together. Moreover, nearest-neighbor analysis gives insight into the spatial distribution of cell types. It shows whether cells sit in close proximity to cells of their own type or whether they are attracted to the other cell type in co-culture. Statistical significance of the results of nearest-neighbor analysis should also be taken into account. Organization of co-cultured cells of different types on a substrate might just be random and the next neighbor analysis could just show noise instead of real co-localization [139]. To this end, the cumulative distribution of center-to-center nearest neighbor distances of neuronal to glial cells is computed and compared with simulated randomized data sets that are of the same size as the original data.

2.4. Multielectrode Arrays

Function and Applications

Multielectrode arrays (MEAs) are devices consisting of electrode grids attached to glass or plastic chips that are used to monitor the activity of cells and biological tissues. MEA devices vary in form, chip size, electrode thickness and number, grid density, and conducting path layout but they all follow the same principle to enable parallelized and correlated electronic cellular read-out with multiple interaction points. Their customizable design and non-invasive function make MEAs a valuable tool for long-term observation of cellular networks. They can be used to analyze for example the electrical activity of neuronal and muscle cells making them useful for applications in electrophysiological and drug development studies. Cellular processes such as neurotransmitter release and muscle contraction can be observed in real-time on multielectrode arrays. Moreover, electrical stimulation of cells and recording of their immediate response is also possible. Clinical applications of MEAs include the monitoring of electrical activity of the heart in patients with cardiac disease, as well as muscle stimulation in paralyzed patients. Historically, MEA techniques have been around since at least 1972 when Thomas et al. successfully conducted action potential measurements [140]. A comprehensive overview of *in vivo* and *in vitro* multielectrode array technologies is available from Spira et al. [141] and Tanwar et al. [60].

The quality of signal recording and transduction in multielectrode arrays is defined by the spatial resolution and coupling efficacy of the device. Good spatial resolution of data recording is achieved using a dense array of small-sized electrodes. Ideally, the diameter of an electrode should be smaller than the average size of a cell that is seeded onto the MEA. Dense arrays of small electrodes enable detailed observation of cellular networks. However, high-density MEAs with sub-cellular spatial resolution give rise to new challenges to signal read out and material design. Several thousand interaction points need to be read out simultaneously and continuously over long periods of time. Possible solutions include for example CMOS (complementary metal oxide semiconductor) techniques that essentially use multiplexing methods with electronic switches to reduce the number of necessary connections between electrodes and amplifiers [142,143]. Miniaturization of electrodes leads to an increased self-impedance and eventually to enhanced thermal noise (Johnson-Nyquist noise). This issue can be addressed with an increased surface area of electrodes using (nano) porous materials or surface roughening fabrication techniques. For the work of this thesis, titanium nitride with nanocolumnar surface modification has been tested as a possible material for high-density multielectrode arrays with lowered self-impedance. The second issue that defines the usability of MEAs is the coupling of cells to the device. Cells seeded onto MEAs form adhesion points on the substrate material whereby a cleft filled with cell culture medium (or a similar ionic solution) is formed between the cell membrane and the electrode array. In an electrical circuit analog of the neuron-electrode-interface, this cleft gives rise to

the so-called seal resistance [141]. During an action potential, ions flow in the cleft and the quality of signal recording of the electrode is characterized by the seal resistance. MEAs usually show seal resistance vales of 100 kΩ up to several MΩ which makes an amplitude of up to 1 mV of an action potential (100 mV) measurable [141]. Signals with lower amplitudes remain undetectable or cannot be distinguished. To solve this issue, multielectrode arrays with improved cell-electrode contact are needed.

A limiting factor of medical *in vivo* application of implantable multielectrode arrays is the fundamental mismatch of stiff electrodes (Young's modulus of Si: 150 GPa) and soft biological tissue (elastic modulus of brain tissue: 100 kPa) [64]. The insertion of electrodes into the brain leads to an acute inflammatory response resulting in tissue swelling. The trauma response also involves necrosis of tissue at the insertion site. Activated microglia invade the site within one day and release chemokines, cytokines, and neurotransmitters. After about 6-8 days, the microglia have cleared the injury site from cellular debris by phagocytosis, and excess fluids are reabsorbed [144]. The acute immune reaction is followed by a chronic response which involves continued inflammation leading to glial scarring due to adhesion of activated microglia at the implant and additional astrocyte activation [144]. The glial scar essentially insulates the implanted electrodes from neurons and therewith increases the impedance and decreases recordable signal intensities.

Electrochemical Impedance Spectroscopy

The quality of signal recording and transduction of systems of cellular networks grown on multielectrode arrays can be assessed using electrochemical impedance measurements. To this end, an alternating voltage is applied to the system, and the resulting current is measured. Ohm's law is then used to compute the system's impedance from the voltage and current. This procedure is done for several frequencies on a spectrum (frequency sweep), hence the name electrochemical impedance spectroscopy. The impedance is a complex quantity $Z(\omega)$ and can be written as follows [145]:

$$Z(\omega) = \frac{\tilde{V}(\omega)}{\tilde{I}(\omega)} = \left| \frac{\tilde{V}(\omega)}{\tilde{I}(\omega)} \right| (\cos \varphi(\omega) + i \sin \varphi(\omega)) = Z_{\mathrm{r}} + i\, Z_{\mathrm{i}}$$

(9)

Where ω is the angular frequency related to the frequency f by $\omega = 2\pi f$, and φ is the phase angle between the input and output signals. i denotes the imaginary number and the variables $\tilde{V}(\omega)$ and $\tilde{I}(\omega)$ are complex time-invariant numbers accounting for the amplitude and phase of the sinusoidal functions for the voltage and current. The real part of the impedance Z_{r} is called resistance and the imaginary part Z_{i} is known as reactance.

A valuable tool to measure the signal recording and transduction quality of a cell-MEA system is the relative impedance Z_{rel} which quantifies the cellular contribution to the impedance magnitude spectra. It is obtained from measurements of electrodes covered with cells and corresponding blank values:

$$Z_{\mathrm{rel}} = \frac{|Z|_{\mathrm{covered}} - |Z|_{\mathrm{cell\text{-}free}}}{|Z|_{\mathrm{cell\text{-}free}}}$$

(10)

Electrochemical impedance spectroscopy measurement results in terms of spatial resolution are limited by technical characteristics of the used multielectrode array. Employed electrode materials and electrode areas influence the quality of recorded signals or more precisely the signal-to-noise ratio (SNR) which is a measure of the strength of the measured signal in comparison with background noise [146].

3. Results and Discussion

3.1. Proliferation and Cluster Analysis of Neurons and Glial Cell Organization on Nanocolumnar TiN Substrates

The content of this chapter has been published in the manuscript "Proliferation and Cluster Analysis of Neurons and Glial Cell Organization on Nanocolumnar TiN Substrates" [147].

DOI: 10.3390/ijms21176249

Reprinted with permission from Alice Abend, Chelsie Steele, Sabine Schmidt, Ronny Frank, Heinz-Georg Jahnke, and Mareike Zink, *International Journal of Molecular Sciences* 21, 6249 (2020). Copyright 2020 by MDPI.

Article

Proliferation and Cluster Analysis of Neurons and Glial Cell Organization on Nanocolumnar TiN Substrates

Alice Abend [1], Chelsie Steele [1], Sabine Schmidt [2], Ronny Frank [2], Heinz-Georg Jahnke [2,*] and Mareike Zink [1,*]

[1] Soft Matter Physics Division and Biotechnology & Biomedical Group, Peter-Debye-Institute for Soft Matter Physics, Leipzig University, Linnéstr. 5, 04103 Leipzig, Germany; alice.abend@uni-leipzig.de (A.A.); cs73gygu@studserv.uni-leipzig.de (C.S.)

[2] Centre for Biotechnology and Biomedicine, Molecular Biological-biochemical Processing Technology, Leipzig University, Deutscher Platz 5, 04103 Leipzig, Germany; sabine.schmidt@bbz.uni-leipzig.de (S.S.); ronny.frank@bbz.uni-leipzig.de (R.F.)

* Correspondence: heinz-georg.jahnke@bbz.uni-leipzig.de (H.-G.J.); zink@physik.uni-leipzig.de (M.Z.); Tel.: +49-(341)-9731246 (H.G.J.); +49-(341)-9732573 (M.Z.); Fax: +49-(341)-9731249 (H.-G.J.); +49-(341)-9732479 (M.Z.)

Abstract: Biomaterials employed for neural stimulation, as well as brain/machine interfaces, offer great perspectives to combat neurodegenerative diseases, while application of lab-on-a-chip devices such as multielectrode arrays is a promising alternative to assess neural function in vitro. For bioelectronic monitoring, nanostructured microelectrodes are required, which exhibit an increased surface area where the detection sensitivity is not reduced by the self-impedance of the electrode. In our study, we investigated the interaction of neurons (SH-SY5Y) and glial cells (U-87 MG) with nanocolumnar titanium nitride (TiN) electrode materials in comparison to TiN with larger surface grains, gold, and indium tin oxide (ITO) substrates. Glial cells showed an enhanced proliferation on TiN materials; however, these cells spread evenly distributed over all the substrate surfaces. By contrast, neurons proliferated fastest on nanocolumnar TiN and formed large cell agglomerations. We implemented a radial autocorrelation function of cellular positions combined with various clustering algorithms. These combined analyses allowed us to quantify the largest cluster on nanocolumnar TiN; however, on ITO and gold, neurons spread more homogeneously across the substrates. As SH-SY5Y cells tend to grow in clusters under physiologic conditions, our study proves nanocolumnar TiN as a potential bioactive material candidate for the application of microelectrodes in contact with neurons. To this end, the employed K-means clustering algorithm together with radial autocorrelation analysis is a valuable tool to quantify cell-surface interaction and cell organization to evaluate biomaterials' performance in vitro.

1. Introduction

The human brain is such a complex system that its composition and architecture are still not fully understood. Even the number of neurons and glial cells in the brain remains questionable [1,2]. Besides structural heterogeneities within the brain and related unsolved questions in neuronal science [3], in light of the currently increasing numbers of cases of neurodegenerative diseases such as Parkinson's disease, the study of cell behavior and cellular function in the brain is more important than ever before [4].

In vivo animal studies of diseases, such as Parkinson's disease, are difficult to assess because they comprise a varying age of onset, symptoms, and rate of progression. This heterogeneity requires the use of a variety of animal models to study different aspects of the disease [5]. Alternatively, organotypic cultures offer the possibility to investigate brain tissue slices ex vivo [6]. However, especially for adult mammalian tissues, organotypic preservation is difficult and tissue distortion often takes place within a few days in culture. As shown by Kallendrusch et al., nanostructured surfaces employed as tissue scaffolds, such as titanium dioxide nanotube arrays, can overcome this issue and allow us to culture adult tissue slices of the brain for at least 10 days [7].

In vitro cell cultures are much easier systems to use to assess cellular function/dysfunction and the effect of drugs to develop new treatments and tailored therapies [8,9]. Moreover, cell cultures also offer good testbeds to study the interaction of neurons and other brain cells in contact with biomaterials employed, e.g., for application as brain pacemaker devices for deep brain stimulation [10]. The interaction of the neurons with the surface of the pacemaker's electrodes plays a major role in the functionality of the device and, consequently, therapy success [11]. Thus, research focuses on the fabrication of biocompatible materials that promote cell adhesion, proliferation, and physiological function and provide stable charge transfer at the brain/machine interface [12]. These materials are, for example, based on metals [13], carbon [14,15], or silicone compounds [16]. Commonly used electrode materials for the electrochemical analysis of biological samples, such as cells and tissues, are noble metals, like gold and platinum, because of their high conductivity, chemical stability, and biocompatibility [17–21].

Not only the material itself but also the surface topography plays an important role in the interaction with cells [22]. Surface topography designs vary from simple microgrooves [23,24] and micrometer-sized pillars [25,26] down to nanofabricated structures [27], nanowires [28,29], nanopillars [30], and nanotubes [31], and can also be combined with novel surface coatings [32,33].

Beyond that, there are alternative electrode materials that offer application-specific advantages, like optical transparency (indium tin oxide, ITO [17]) or an increased surface area (titanium nitride, TiN [34]). The latter allows the shrinking of microelectrode size without losing detection sensitivity due to a lowered self-impedance of the electrode [35–37]. These materials offer great perspectives for in vitro lab-on-a-chip devices, such as multielectrode arrays (MEA). For example, as shown by Jahnke et al., MEAs have already been successfully employed for in vitro screenings of hallmarks of neurodegenerative diseases by impedance spectroscopy [38]. Additionally, microelectromechanical systems (MEMS) and microsystems composed of the above-mentioned materials have enabled the study of neurons from the single unit to the scale of large populations and neural circuits (for an overview, see Ref. [39,40]). Lab-on-a-chip formats even allow the combination of electrical function with optical analysis and biochemical patterning to enhance cell-surface interaction [41].

For any in vitro cell cultures with the aim to determine the interaction of biomaterials with cells, it is of great importance to define quantitative measures that determine if a biomaterial is bioactive and supports proliferation on the surface. Research methods to examine the compatibility of the electrode material often involves immunostaining of relevant cellular components. In addition, the number of cells and cell division rates can easily be determined. However, how cells organize on the surface, if they homogeneously spread or agglomerate, is often neglected, and a quantitative measure of cellular organization is missing. For example, under physiologic conditions, neurons such as SH-SY5Y—an established human neuroblastoma cell line to study Parkinson's disease—tend to cluster on a surface [42].

Radial autocorrelation functions and cluster formation algorithms can offer powerful tools to quantify the spatial organization of particles up to cells on two-dimensional surfaces, as well as three-dimensional environments. While radial autocorrelation functions have been employed before to determine spatial correlations of particles in supercooled liquids [43], Pan et al. [44] showed that autocorrelation functions calculated for cultured cells can also be used to quantify cell sizes.

Here, we show how proliferation assays, in combination with a quantitative cellular organization analysis performed by radial autocorrelation functions and clustering analysis, can be used to quantify cellular performance on potential biomaterials. In our study, we investigated the

behavior of neurons and glial cells on different surfaces such as TiN substrates and nanocolumnar TiN, which exhibit an increased surface area compared to TiN with larger grain sizes. The interaction of cells with this nanocolumnar TiN has never been studied before, and good biocompatibility would offer great potential for the development of miniaturized multielectrode arrays as described above. Our results show a clear superiority of these materials in terms of cell division rate and the cellular organization of neurons in contrast to cell behavior on gold and ITO surfaces. The latter two materials were employed for control experiments as these materials are considered non-toxic and are often the materials of choice for electrodes in contact with neurons [45]. Future applications of the presented nanocolumnar TiN materials aside, our combined analysis tool of clustering algorithms and radial autocorrelation calculations allows for a fast evaluation of biomaterials' performance in vitro, by simply measuring cell positions from fluorescent images.

2. Results

2.1. Topographies of Electrode Materials

Before investigating the interaction of neurons and glial cells with different electrode materials, the topographies of the surfaces were characterized by atomic force microscopy (AFM), as shown in Figure 1. The gold substrates exhibited the smoothest surface features with a root-mean-square (RMS) roughness of (2.95 ± 1.63) nm, comparable to the thin TiN coating with (2.98 ± 1.24) nm. By contrast, ITO showed the highest RMS roughness of the tested materials with a value of (8.36 ± 0.99) nm, also significantly exceeding the thick TiN layers (in the following, termed TiN nano and nanocolumnar TiN) with a RMS roughness of (6.42 ± 0.99) nm. With respect to the surface area increase (viz. the dimensionless ratio of surface area to projected area), TiN nano showed the highest increase with 1.27 ± 0.08 of the projected surface area, while the other materials were below 1.1 (Au: 1.02 ± 0.01, ITO: 1.10 ± 0.02, TiN: 1.07 ± 0.01).
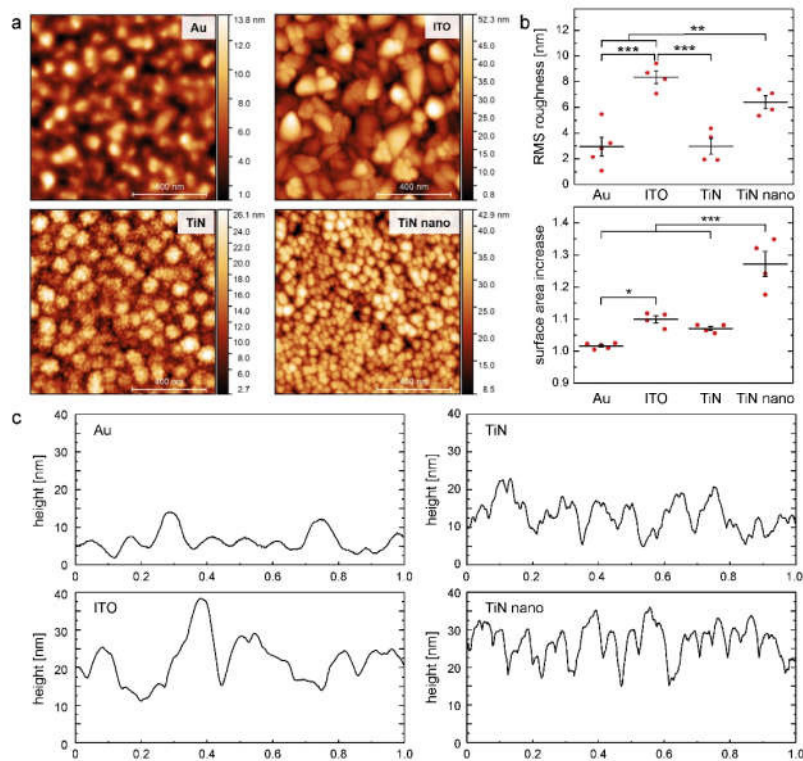

Figure 1. Atomic force microscopy characterization of the tested electrode materials: (**a**) 1 × 1 μm images of gold (Au), indium tin oxide (ITO), titanium nitride (TiN), and TiN nano with nanocolumnar

structure; (**b**) area-derived metrics of the AFM images (root-mean-square (RMS) roughness and ratio of surface area to projected area (surface area increase)); the horizontal lines represent the mean values of the data points (red dots), while the vertical lines show the standard errors (mean ± se, ANOVA with Tukey's post-hoc test, * = $p < 0.05$, ** = $p < 0.01$, *** = $p < 0.001$); (**c**) one-line profiles of AFM images.

Besides the different surface roughness, varying-grain-sizes of the different surfaces became visible (see Figure 1). While Au exhibited smooth transitions between the grains with a mean grain size of (82 ± 10) nm, ITO showed clearly distinguishable crystallites with a larger mean grain size of (109 ± 19) nm. Besides different film thicknesses of the TiN layers due to different sputter times: 150–200 nm for TiN and 500–550 nm for TiN nano, their surface morphologies differed remarkably. While TiN exhibited a cauliflower motif with a mean grain size of (90 ± 11) nm and subgrains of (17 ± 4) nm, TiN nano appeared to have a nanocolumnar structure with sharply delimited single-type grains with a size of (38 ± 9) nm, being the origin of the high surface area increase.

2.2. Cell Growth on Electrode Materials

In order to investigate neuronal and glial cell behavior on potential electrode materials, the human neuroblastoma cell line SH-SY5Y and the human glioblastoma cell line U-87 MG were grown on the four different electrode materials presented above. Cells were fluorescently labeled, imaged, and subsequently counted one and three days after seeding for the glial cell type, while the number of neuronal cells was investigated 1 and 3 days after differentiation. The results of the average cell numbers for each substrate are shown in Figure 2.
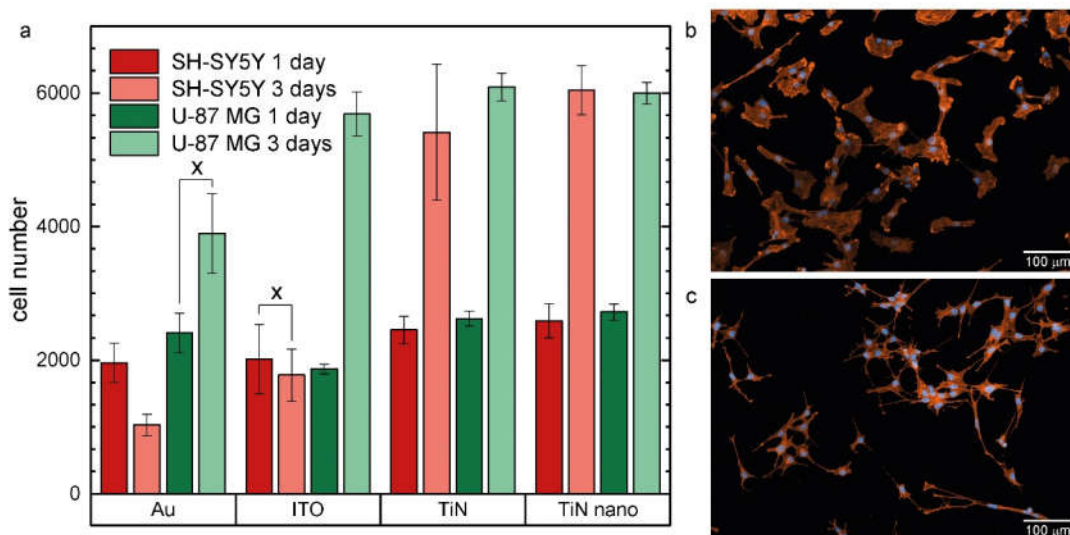

Figure 2. (**a**) Average number of SH-SY5Y and U-87 MG cells grown on different electrode materials (Au, ITO, TiN, nanocolumnar TiN) after one and three days in culture. Values marked with x are not statistically significant ($p > 0.05$); (**b**) fluorescent image of U-87 MG cells cultured on TiN nanocolumnar surfaces for 1 day. Cell nuclei are blue and actin fibers are colored orange. The scale bar represents a length of 100 μm; (**c**) fluorescent image of SH-SY5Y cells grown on a TiN nanocolumnar substrate for 1 day plus additional 72 h incubation with culture medium supplemented with staurosporine to induce cell differentiation. Colors and scale bar as in (**b**).

For the neuronal cells, within the first day after differentiation, the number of cells on all four substrates shows no statistical difference. Around 2000 cells adhered to all surfaces. However, after 3 days on ITO, the cell number remained constant and even halved on Au, while on TiN and TiN nanocolumnar surfaces, cells proliferated with an around three-fold increase to approximately 5400 cells on TiN and 6000 cells on nanocolumnar TiN.

Similar results were found for the glial cells: 1 day after seeding, similar cell numbers were seen for Au (2400 cells), TiN (2600 cells), and TiN nanocolumnar substrates (2700 cells) and fewer cells on ITO (1800 cells). Two days later, cell numbers more than doubled to approximately 6000 cells with Au as the only outlier on which we counted approximately 4000 cells, thus 2000 cells less than on the other materials.

Comparing the experimental results for the neuronal SH-SY5Y and glial U-87 MG cells, we observed a similar growth behavior on TiN and TiN nanocolumnar substrates for both cell types. Here, seeding the same number of cells led to equal numbers of cells for short and longer culture times. The situation for gold and ITO materials seems to be completely different. The SH-SY5Y cells did not proliferate as fast on these materials as the U-87 MG cells. We found about three times more U-87 MG cells on ITO substrates as SH-SY5Y cells for the longer growth time. For the gold material, that factor rose to four, while the SH-SY5Y cell population decreased, and the U-87 MG cell number grew.

2.3. Radial Autocorrelation of Cell Positions

We performed a radially averaged autocorrelation analysis for the cell nuclei positions for all 48 samples, viz. glia and neuronal cells cultured on Au, ITO, TiN, and TiN nanocolumnar substrates for 1 and 3 days. Representative results of the radially averaged autocorrelation functions are presented in Figure 3. As shown by Baker et al. [46], the undulating autocorrelation curves represent a homogeneous distribution of objects and uniform object size. The first minimum of the curves marks the typical size of objects in an image, whereas the first peak gives an estimate on the object spacing. On the other hand, flattened autocorrelation curves indicate an inhomogeneous distribution of objects and several different object sizes in an image. The point where the curve bends from a steep slope to an almost constant regime characterizes the average size of objects.
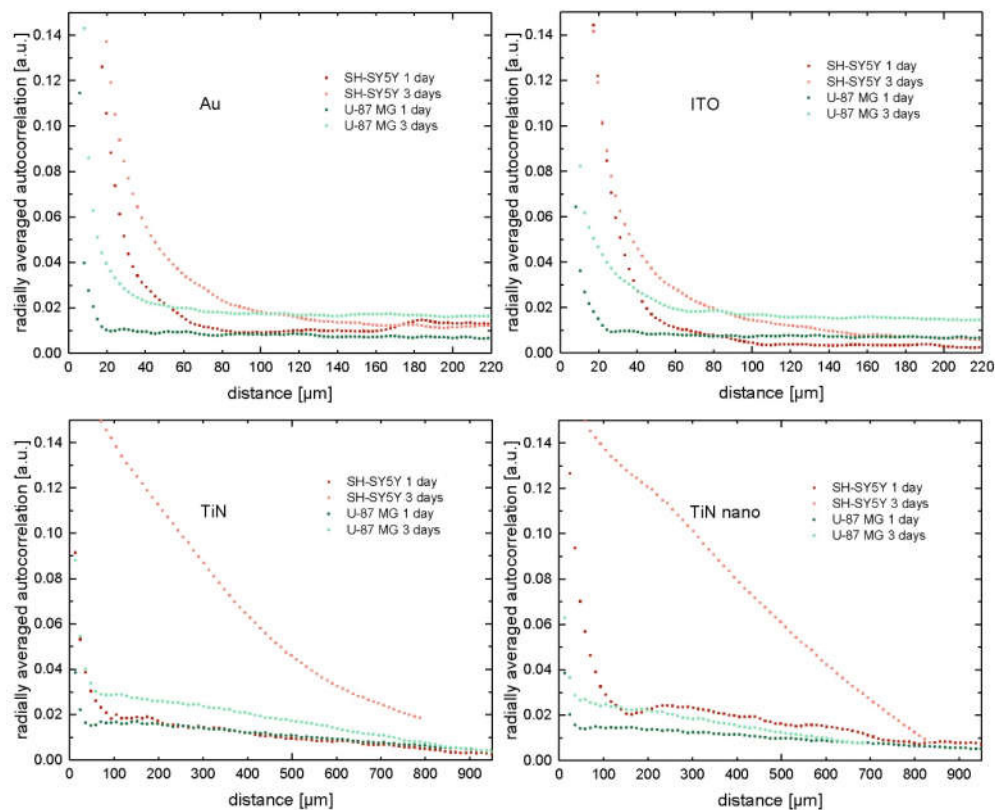

Figure 3. Radially averaged autocorrelation analysis for cell nuclei positions obtained from 12 individual experiments with U-87 MG cells (green) and SH-SY5Y cells (red) cultured on different materials.

We see rapidly decreasing autocorrelation functions for the U-87 MG cells on all materials (green curves in Figure 3). The graphs of the 1 day culture experiments show a small but noticeable undulating form with distinct first minima (20 μm for gold and ITO, 50 μm for TiN materials). Additionally, for gold, the curve displays a peak at about 30 μm and for ITO and both TiN materials, around 70–80 μm, which mark the distance to the next object. Comparing the graphs to the original fluorescent images, we notice an even distribution of U-87 MG cells, viz. the cell population was homogeneously spread over the entire surface. In fact, the observed correlation length of approximately 20 μm for the U-87 MG cells cultured on gold for 1 day corresponds to objects composed of two cell nuclei in the fluorescent image, while single-cell nuclei were also present on the substrate. By contrast, the radially averaged autocorrelation curves of glial cells cultured for 3 days on gold do not show the undulations anymore. Looking at the associated cell images revealed that the cells still grew uniformly distributed over the entire substrate area. Nevertheless, small cell agglomerations of various sizes became visible. We see objects of about 20 to 40 μm in diameter, which corresponds to agglomerations of 2 to 5 cells in the images of glial cells cultured on gold substrates for 3 days. Thus, U-87 MG cells proliferated rapidly, as can be seen from Figure 2, and grew homogeneously distributed on all tested materials. Such behavior became visible in the autocorrelation curves after 3 days of culture, which are shifted toward larger distances in comparison to their 1 day counterparts, indicating the existence of (on average) larger cell agglomerations. A very similar behavior of glial cells became present on the ITO substrates. After one day of culture, mainly single cells and pairs were homogeneously distributed on the surface, reflected by the autocorrelation curve minimum around 20 μm, while, after 3 days, smaller aggregates—still homogeneously distributed—were seen, represented by a shift in the autocorrelation minimum toward larger correlation distances around 40–50 μm. Additionally, we observed larger cell agglomerations (50 μm) on TiN and TiN nanocolumnar substrates in comparison to their gold and ITO counterparts after 1 day of culture. These objects are still homogeneously distributed. The correlation length is shifted for TiN and nanocolumnar TiN after additional growth time, and the comparison with fluorescent images reveals cell agglomerations of various sizes up to about 100 μm.

However, in the case of the SH-SY5Y cells (red curves in Figure 3), we see considerably different results. While, after 1 day, the correlation length, viz. the first minimum where the steep slope transits into an almost constant regime, was found for 60 μm (Au), 70 μm (ITO), 90 μm (TiN), and 160 μm (nanocolumnar TiN), there are noticeable shifts in the correlation curves to longer distances for longer culture times on all substrate types. This long-range correlation indicates the growth of cell clusters of various sizes. We do not see any undulating graphs for the gold and ITO substrates. Comparison with fluorescent images revealed cell agglomerations of various sizes, which correlate with the position of the minimum of the autocorrelation graphs. However, for the neuronal cells grown on TiN and nanocolumnar TiN for 1 day, the autocorrelation curves, in fact, show the undulating form as similarly seen for glial cells on Au. However, this behavior vanished after additional culture time, and we noticed correlation lengths of up to 500 μm for TiN samples and even larger values for nanocolumnar TiN. Figure 4 shows the autocorrelation curves for all experiments of SH-SY5Y cells with three days of culture time. The three graphs with the prominent steep decrease correspond to experiments where the cells formed especially large agglomerations of about 1200–2000 μm. Overall, we see cluster formation of greatly varying sizes on different substrate types but also between individual experiments on the same material.
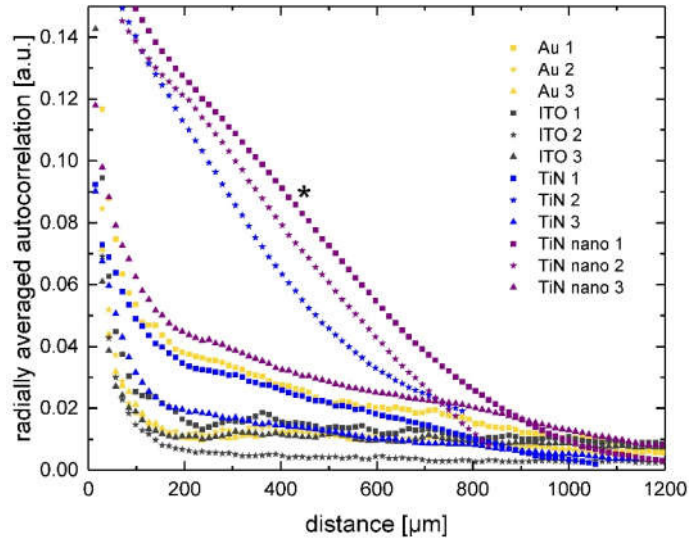
Figure 4. Radially averaged autocorrelation function of cell nuclei positions of SH-SY5Y neuronal cells after 3 days of culture on various substrate materials. The experiment and data points marked with * serves as an example of the K-means cluster analysis shown in Figures 5 and 6.

2.4. Cell Clustering Results

To further investigate the spatial distribution and the formation of cellular clusters on the substrates, we employed a K-means algorithm as described in the Methods. As we saw that the glial cells were almost evenly distributed over the surface of all materials, we only considered the neuronal cell distributions here. One example of such an analysis is shown in Figure 5. Each data point represents a single SH-SY5Y cell grown on a TiN nanocolumnar surface—corresponding to the autocorrelation graph marked with a * in Figure 4. The algorithm sorted the cells into four clusters, indicated by the different colors. Although there seems to be an overlap of clusters, every cell belongs to exactly one cluster and is not counted twice. The ellipses mark the area of the clusters surrounding the cluster centroid, while there are only a few outliers visible. In order to validate if the calculated cluster number is correct, we compared the results by employing the elbow method and gap statistics as described in the Materials and Methods. The corresponding elbow graph denotes the optimal cluster number at the point where the steep decline bends over to a flattened regime. Here, we found this bending point of the elbow graph (Figure S1) for an ideal cluster number of four for the example of neuronal cells on a TiN nanocolumnar substrate—in line with the results from the K-means algorithm. Moreover, our results from gap statistics (see Figure S2) corroborate four as the ideal cluster number by showing a maximum peak at k = 4.
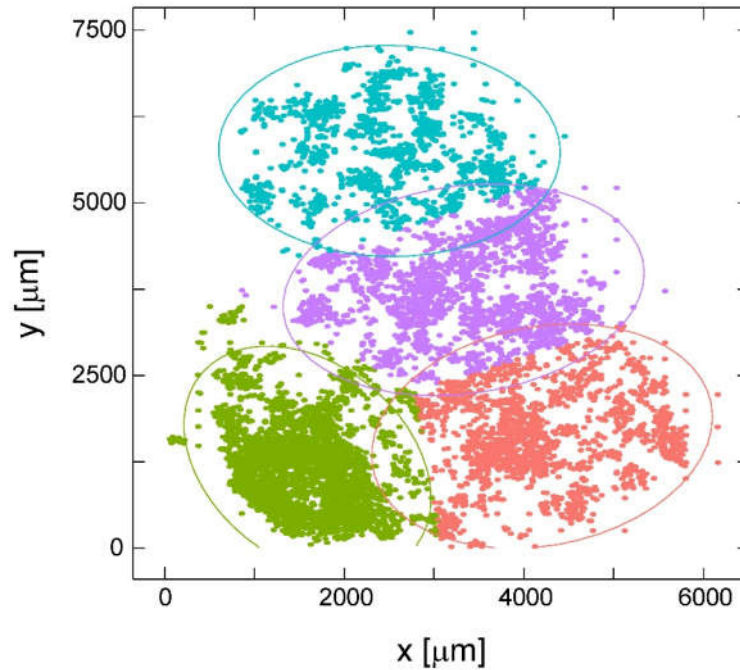
Figure 5. Result of K-means clustering of SH-SY5Y cells grown on TiN nanocolumnar substrates after 3 days. Each data point represents a single cell. The different colors denote cluster 1 (red), cluster 2 (green), cluster 3 (blue), and cluster 4 (purple). The cell distribution corresponds to the autocorrelation function marked with * in Figure 4. Note that the graph does not represent the entire substrate area of 0.22 cm², but only the area covered by cells.

Additionally, we used the silhouette method (see Materials and Methods) to verify our choice of the optimal number of clusters for each experiment and validate if the cells are sorted into the right cluster. Figure S3 shows the average silhouette coefficient as a function of cluster numbers. The peak of the curve marks the optimal number of clusters. In this example, it is four, which corroborates our choice of four clusters. If the silhouette width turned out to be lower than a certain threshold, which was chosen to be 0.35 after several test simulations, the cluster number was considered wrong. Thus, other cluster numbers were iteratively tested until the silhouette width exceeded the value of 0.35. Figure 6 shows the silhouette plot for neuronal cells on nanocolumnar surfaces corresponding to the cluster analysis of Figure 5 (here, the calculated silhouette width was 0.48). This indicates a high-quality clustering result as there are very few falsely grouped cells, which would be indicated by negative silhouette coefficient values.
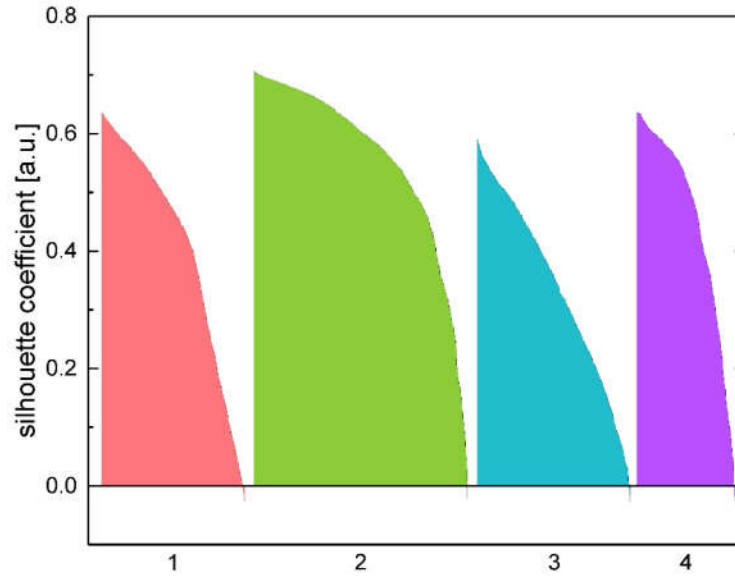
Figure 6. Silhouette width plot associated with the example experiment shown in Figure 5 (neuronal cells on TiN nanocolumnar surfaces after 3 days). The four clusters are color-coded. Positive values indicate a high-quality cell sorting result.

Besides the cluster analysis shown above for neuronal cells on TiN nanocolumnar surfaces after 3 days, we used the K-means clustering algorithm to investigate cluster formation on all substrate materials. As shown in Figure 7, we can see a great difference in the clustering behavior of SH-SY5Y cells: The density of the cell clusters is much lower on gold and ITO substrates than on TiN-containing substrates. The clusters do not grow significantly denser on gold and ITO with longer cell growth times. By contrast, the clusters of cells grown on TiN and TiN nanocolumnar substrates double their density on average for the longer growth time.
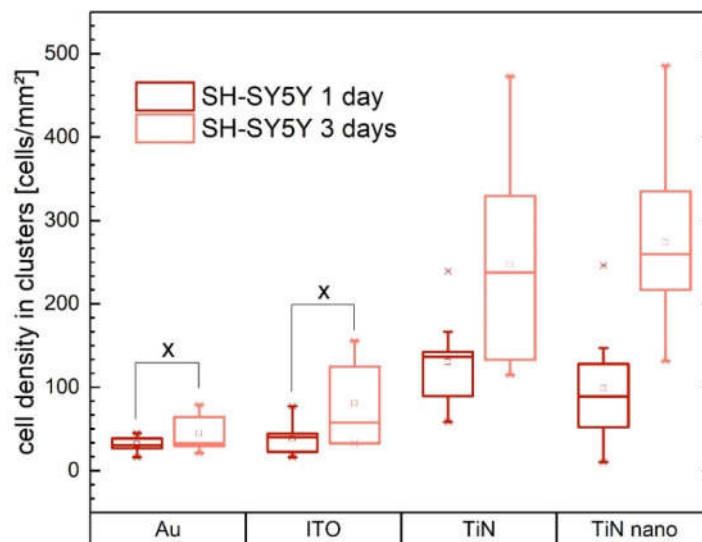

Figure 7. Cell density in clusters of SH-SY5Y cells grown on different electrode materials (Au, ITO, TiN, TiN nano) after one and three days of growth as a result of K-means clustering. Values marked with X are not statistically significant ($p > 0.05$).

3. Discussion

In our study, we investigated the proliferation and organization of neuronal (SH-SY5Y) and glial (U-87 MG) cells on planar and nanocolumnar TiN, which offer great potential for application as a multielectrode array material. Results were compared to cell behavior on ITO and gold surfaces as both materials are well-known to promote adhesion of neurons and are used for neural stimulation systems and brain/machine interfaces [47,48]. Furthermore, by employing radial autocorrelation functions in combination with clustering analysis, we quantified the cellular arrangement on the surfaces. We found that high cell numbers, viz. fast proliferation, do not necessarily lead to large cell clusters. In the case of U-87 MG cells, we obtained rapid cell proliferation on all materials, while only the formation of small cell agglomerations in comparison to their neuronal counterparts was seen. Judging from the corresponding radially averaged autocorrelation functions and fluorescent images, the glial cells form small cell agglomerations of different sizes rather than large clusters after 3 days of culture time. However, SH-SY5Y cells form large clusters on TiN and nanocolumnar TiN substrates after 3 days of growth, and we saw the highest neuronal cell numbers on these materials. Surprisingly, the SH-SY5Y cell numbers remained constant on ITO and even shrank on gold substrates for longer growth times, while the cellular organization changed, and agglomerations of different sizes became visible as similarly observed for U-87 MG cells. Nevertheless, glial cells proliferated much faster under the same conditions on these materials. Even though gold and ITO are considered non-toxic as mentioned before, the reduced proliferation rate of SH-SY5Y cells points toward altered physiology and metabolism, which should be addressed in future studies.

For a more detailed analysis of neuronal cluster formation, we employed K-means cluster analysis of the SH-SY5Y cell experiments. Here, the cell density inside clusters mirrored the cell proliferation behavior of the neuronal cells on planar TiN and TiN nanocolumnar substrates. Thus, higher overall cell numbers resulted in denser cell clusters for these materials. On the other hand—although not statistically significant—the cell density in clusters grown on gold and ITO increased with growth time, while the overall cell number on these substrates decreased in the case of gold (statistically significant) and stayed constant on ITO.

SH-SY5Y cells on gold and ITO formed several small agglomerations of different sizes, which are scattered homogeneously over the substrate. On first sight, the K-means algorithm contrarily sorts these agglomerations in no more than four clusters. Nevertheless, the cluster algorithm results are consistent with the outcome of the autocorrelation curve as well as our visual inspections of the fluorescent images. Here, the cell patterns hardly changed after additional culture time, and the cells still grew homogeneously distributed but arranged in small agglomerations of different sizes. These small clusters grew over time, which is also represented by the shifted radially averaged correlation length; however, the entire cell patterns did not change fundamentally, i.e., no large and dense clusters were formed. Such behavior is indeed reflected by the K-means algorithm, which did not give any statistically significant change in cell density in clusters for the gold and ITO materials for neuronal cells with longer culture times. Thus, we conclude that the K-means clustering algorithm works well for detecting large, dense cell clusters (on TiN and nanocolumnar TiN in our case) but fails to identify smaller cell agglomerations and, instead, pools them into bigger but therefore less dense clusters. For small agglomerations, the radially averaged autocorrelation function can reliably quantify such cellular arrangements and also predicts large cell clusters. Similar observations were reported by Baker et al. by applying the radially averaged autocorrelation method to analyze natural quartz crystal patterns [46]. Very long correlation lengths of several hundred micrometers always occurred for our experiments where we saw especially large cell clusters. We cannot read the actual size of the largest object directly from the autocorrelation graphs, due to the blurring effect of the radial averaging (here, the K-means algorithm is the analysis of choice); however, the curve gives an average size of the objects on the respective substrates.

While the proliferation data clearly show that the TiN and nanocolumnar TiN substrates support cell division best, the radial autocorrelation function in combination with cluster analysis alone cannot indicate if a surface exhibits optimal conditions for the in vitro cell culture. As shown by Chan-Ling et al., as well as Ogata et al., a physiological pattern for astrocytes is a homogeneously

distributed cell layer where only the most peripheral cell processes are in contact with neighboring cells [49,50]. Cells are shaped more like polyhedrons instead of stars [50]. The star-like shape stems from the distribution of fluorescently labeled glial fibrillary acidic protein (GFAP) in cells [51]. An in-depth review of the role of astrocytes in the function and architecture of the brain is available from Nedergaard et al. [52]. In our study, we can see from the associated fluorescent images of U-87 MG cells that the cells look indeed more like polyhedrons than stars. Moreover, our cells show a homogeneous distribution for short and longer culture times but develop small cell agglomerations. In this context, glial cells form physiological patterns on all investigated material types in our experiments in vitro. Thus, comparison of fluorescent images with cluster analysis is a valuable tool for improved quantification of biocompatible surfaces.

Considering the effect of surface topography, Vallejo-Giraldo et al. investigated SH-SY5Y cells grown on ITO substrates with varying surface roughness [47]. They reported that the semi-rough substrates (R_a = 19 nm) performed best in terms of cell growth, while neuronal cells do not attach well on very smooth (R_a = 1 nm) or especially rough surfaces (R_a = 81 nm) [47]. Thus, poor proliferation of SH-SY5Y cells on ITO in comparison to the TiN substrates might be attributed to the surface structure, which hinders cell adhesion. Khan et al. came to similar conclusions while investigating the adhesion of neuronal cells (rat cortical neurons) on silicon wafers [53]. According to their study, neuron adherence increases with substrate surface roughness until a certain limit is reached. Interestingly, Fan et al. found analogous results for neuronal cells cultured on SiO_2 layers and, moreover, reported that the cells migrated to areas of optimal roughness on patterned surfaces [54]. Recently published work from Yoon et al. showed the superiority of nanostructured surfaces (carbon nanotubes) in comparison to smoother graphene substrates and polystyrene films in terms of neuronal marker expression and neural activity in multielectrode arrays, recording experiments for differentiated SH-SY5Y cells [55]. A lower differentiation-induced apoptotic rate and a higher cell proliferation rate are reported for the nanostructured materials, in comparison to the smoother surfaces. Researchers here concluded that the overall improved performance of the neuronal cells on carbon nanotube surfaces does not originate from the choice of the material (carbon), but rather from the nanoscale topography of these substrates. This article included bright-field images, which show the formation of more and larger cell agglomerations on the nanostructured material in comparison to the graphene and polystyrene films. Thus, we expect that the formation of cell clusters might be beneficial for the performance of neuronal cells—in agreement with Shipley et al., who reported that SH-SY5Y tend to grow in clusters under physiologic conditions [56]. In line with Yoon et al., we saw an improvement in cell proliferation and the formation of especially large clusters of our SH-SY5Y cells on the nanostructured TiN material in comparison to the widely used gold and ITO materials. In contrast to Yoon et al., we expect that the chemical composition of the surface strongly influences cell behavior, and it is not only the topography that determines proliferation and cell adhesion. Even though our Au and TiN substrates exhibited a very similar RMS roughness ((2.95 ± 1.63) vs. (2.98 ± 1.24) nm, respectively) and similar grain sizes ((82 ± 10) vs. (90 ± 11) nm, respectively), neurons proliferated and organized very differently on the surfaces. Thus, it is not only the structure but also the surface chemistry that determines cell behavior.

In a study conducted by Piret et al. with neuronal cells cultured on gallium phosphide materials, a cluster formation of cells was found for both flat and nanostructured (nanowire) surfaces [57]. However, for neurons cultured on flat and nanostructured silicon substrates [58], the cells formed clusters only on the flat surfaces, whereas a homogeneous cell distribution was found on the nanowires. The even cell pattern was apparently accompanied by the loss of functional neuronal network abilities. Thus, it can be concluded that the cluster formation of neurons reflects a favorable cell behavior in in vitro conditions in line with good proliferation, as also seen in our experiments. Here, nanocolumnar TiN offers the best culture conditions for SH-SY5Y cells compared to ITO and gold surfaces, and TiN with larger grain sizes. To this end, our study presents a quantitative tool to assess the neural cell organization on various surfaces in vitro by employing radial autocorrelation functions in combination with cluster analysis. Studies of cell organization can show to what extent the biomaterial supports physiologic growth conditions for specific cell types. The study of biocompatibility and bioactivity of

materials in vitro can be complemented by the investigation of characteristics, such as cell morphology, cell–cell interactions, and physiological and differentiation status.

4. Materials and Methods

4.1. Electrode Materials Preparation

Cover glasses with a diameter of 13 mm and a thickness of 0.13–0.16 mm (VWR GmbH, Darmstadt, Germany) with four different coatings were employed to deposit thin films of indium tin oxide (ITO), gold (Au), and titanium nitride (TiN) in two different surface topographies.

Before film deposition, all coverslips were cleaned in a standard procedure with acetone and isopropanol in an ultrasonic bath and subsequently in 3% hydrofluoric acid for 2 min, and then rinsed with ultra-pure water. The metallic coatings were applied by using the sputter process (CREAMET 500, Creavac GmbH, Dresden, Germany). For the ITO plating, a 4" indium tin oxide target (90:20 wt.%, EVOCHEM GmbH, Offenbach am Main, Germany) was used at a working pressure of 4.5×10^{-3} mbar with an argon (Ar) flow rate of 18 sccm, a combined power of 250 W (DC) and 85 W (RF), and a working distance of 150 mm for 20 min. A heat treatment at 400 °C was performed for 10 min to increase the transparency of the layers. For the gold plating, it was necessary to apply an adhesion promoter layer before, which was realized by the deposition of a 50 nm layer of indium tin oxide. The subsequently applied gold layer was produced at 4.5×10^{-3} mbar, 350 W (DC), a working distance of 150 mm, and an argon flow rate of 18 sccm with a 4" gold target (99.99%, Heimerle&Meule GmbH, Pforzheim, Germany) for 3 min. The same ITO target and sputtering parameters in terms of working distance, working pressure, and argon flow rate were also employed to gain the ITO surfaces for later cell experiments. Here, the sputtering time was 3 min at 350 W (DC).

In order to produce two different titanium nitride (TiN) layers with different topographies, first, titanium (Ti) was used as an adhesion promoter with a 4" titanium target (99.99%, Kurt J. Lesker Company, Jefferson Hills, PA, USA) at 4.5×10^{-3} mbar with an Ar flow rate of 18 sccm, power of 500 W (DC), working distance of 150 mm, and a sputtering time of 5 min. Afterward, a gold layer was coated on top, as described above. Subsequently, the titanium nitride layer was produced by sputter deposition with the same titanium target used before at the same pressure and working distance. In addition to the process, nitrogen with a purity of 99.95% was added at a flow rate of 6 sccm, whereby the Ar flow rate was reduced to 11 sccm. The sputtering power during the process was 600 W (DC). For the thin TiN layers, a coating time of 2.5 min was chosen, and 40 min for the thick layers. The thick layer is defined as TiN nano or nanocolumnar TiN in the Results section.

4.2. Atomic Force Microscopic Analysis

Surface morphologies of the electrode materials were imaged using a JPK NanoWizard 3 atomic force microscope (Bruker Nano GmbH, Berlin, Germany). Data acquisition was performed in direct drive AC mode with a TESPAHAR cantilever (fnom = 320 kHz, dnom = 42 N/m, Bruker). The height (measured) channel was used for image analysis in Gwyddion 2.55. Image analysis included leveling data by mean plane subtraction and, subsequently, a row alignment using the program in-built median of differences method. The root-mean-square roughness and surface areas of the samples were calculated by the statistical quantities tool. For determination of grain sizes, diameters of defined grains were manually measured using the point-to-point distance tool, measuring at least 30 grains/image.

Statistical analyses were performed using GraphPad Prism 5.02. Multiple group comparisons were performed by 1D ANOVA with Tukey's post-hoc test. Differences between two means with $p < 0.05$ were considered significant (*), $p < 0.01$ very significant (**), and $p < 0.001$ extremely significant (***).

4.3. Cell Lines and Cell Culture

We chose two human brain cell lines for our studies: The human neuroblastoma cell line SH-SY5Y (Cat.No. CRL-2266, ATCC LGC Standards GmbH, Wesel, Germany) and the human primary glioblastoma cell line U-87 MG (Cat.No. 300367, CLS Cell Lines Service GmbH, Eppelheim, Germany).

U-87 MG and SH-SY5Y cells were cultured in 1:1 MEM Eagle/Ham's F12 medium containing Earle's salts, L-glutamine, and sodium bicarbonate (Cat.No. M4655 and N6658, Sigma-Aldrich Chemie GmbH, Munich, Germany) supplemented with 10% fetal bovine serum (Cat.No. S0615, Biochrom GmbH, Berlin, Germany) and 1% penicillin/streptomycin (Cat.No. P0781, Sigma-Aldrich Chemie GmbH, Munich, Germany). Both cell lines were incubated in separate culture flasks at 37 °C in a 95% air and 5% CO_2 atmosphere. Cell culture medium was changed every 2–3 days. A mixture of phosphate-buffered saline (PBS, Cat.No. 18912014, Gibco Thermo Fisher Scientific, Waltham, MA, United States), 0.025% (*w/v*) trypsin, and 0.011% (*w/v*) ethylenediaminetetraacetic acid (EDTA, Cat.No. L2143, Biochrom GmbH, Berlin, Germany) was applied for 3–4 min to detach the cells prior to cell counting and seeding.

4.4. Cell Staining and Imaging

Cells were counted in an automatic optical cell counter prior to cell seeding onto the substrate materials (EVETM, NanoEntek Inc., Seoul, Korea). Subsequently, cells were seeded onto different substrate materials (Au, ITO, TiN, nanocolumnar TiN) at a density of 130 cells/mm² in cell culture medium. U-87 MG cells were fixed 24 or 72 h after seeding, respectively. We did not employ longer culture times, to avoid the formation of very dense cell layers for which a cluster analysis would not be possible. Cells were fixed with paraformaldehyde (Cat.No. HT5011, Sigma-Aldrich Chemie GmbH, Munich, Germany) for 15 min. In order to fluorescently label actin fibers and cell nuclei, cells were washed with PBS and cell membranes were permeabilized with a PBS solution containing 1% (*w/v*) Triton X-100 (Cat.No. 9002-93-1, Sigma-Aldrich Chemie GmbH, Munich, Germany) and 0.5% (*w/v*) bovine serum albumin (Cat.No. A2153, Sigma-Aldrich Chemie GmbH, Munich, Germany) for 10 min at room temperature. Afterward, cells were incubated with a PBS solution supplemented with 1 μg/mL Hoechst 34580 (Cat.No. H21486, Molecular Probes, Eugene, OR, USA) and 0.44 μM Alexa Fluor 532 Phalloidin (Cat.No. A-22282, Molecular Probes) at room temperature for 15 min. Subsequently, substrates with fixed cells were washed again with PBS and placed upside down into clean Petri dishes (Cat.No. 80136, ibidi GmbH, Gräfeling, Germany) with mounting medium (Cat.No. 50001, ibidi GmbH, Gräfeling, Germany) to prepare the samples for imaging in an inverse confocal laser scanning microscope. Samples were stored at 4 °C until imaging.

For the SH-SY5Y cells, 24 h after seeding onto the different substrate materials, cells were supplemented with 25 nM staurosporine (Cat.No. S5921, Sigma-Aldrich Chemie GmbH, Munich, Germany) to initiate the cell differentiation process, which takes 72 h to complete [59]. The first samples of SH-SY5Y cells for each substrate type were fixed directly upon removing the culture medium containing the staurosporine, while the second samples were cultured for another 72 h in growth medium and fixed afterward as described above. After fixations, actin fibers and cell nuclei were fluorescently labeled according to the U-87 MG cells.

Cell network morphology was investigated using confocal laser scanning microscopy. Images were acquired with an inverted Zeiss Axio Observer.Z1 microscope equipped with a spinning disk unit (Yokogawa CSU-X1A 5000, Tokyo, Japan) and a 25 × glycerin immersion objective. The complete cell network for each substrate material was imaged as an array of individual dual-channel fluorescence images. Each image encompassed a substrate area of 0.22 cm². Thus, up to 54 images were required to image the entire substrate area.

4.5. Image Analysis and Autocorrelation of Cell Positions

Images of neuronal cell networks were processed using Fiji distribution [60] (Windows 10, 64-bit version) based on ImageJ software [61]. The position of the cells was identified by the location of

fluorescently labeled cell nuclei using the particle tracker tool on previously thresholded and binarized images. Thus, for all images, we extracted the following parameters for each cell type and substrate: Number of cells, growth area, and mean cell density.

In order to analyze the cellular network organization in terms of the nearest neighbors of each cell, the macro "Radially Averaged Autocorrelation" combined with the "Radial Profile" plugin was employed to evaluate a radially averaged two-point autocorrelation function S2 for all images. Such analysis allows measurement of the average size of objects (patches of cell clusters) in conjunction with the distance between these objects as similarly shown by Baker et al. [46] and described in detail by Berryman et al. [62]. Briefly, the ImageJ plugin computes the probability of finding a black pixel in increasing radial distance to an initially chosen black pixel. This process is repeated multiple times with different initial pixels. The results are radially averaged in a second step. The chosen plugin utilizes a fast Fourier transform (FFT) to reduce computation time, while simultaneously correcting for the periodicity of the FFT and finite image size, so the results do not suffer from artifacts. The results are normalized such that the value of the radially averaged autocorrelation function will always be 1 (perfect correlation) at a distance r = 0. It directly follows that an output value of 0 demonstrates the case of no correlation.

4.6. Cluster Analysis of Cellular Network Organization

Additionally, we employed self-written cluster analysis tools programmed in R for further investigation of the spatial distribution of cells on the substrates, including network patterns such as cluster formation. The goal of these cluster analysis methods is to minimize the within-cluster variation. In other words, the clusters are supposed to be dense but located far apart. The within-cluster variation W is defined as the sum of squared distances between cells and their corresponding centroid (i.e., cluster center):

$$W(C_k) = \sum_{x_i \in C_k} \| x_i - \mu_k \|^2 \tag{1}$$

where x_i refers to a cell position in the corresponding cluster C_k with μ_k being the mean value of all data points assigned to this cluster. The total within-cluster variation for any given data set (cell image) is then defined as:

$$totalwithin = totW(k) = \sum_{k=1}^{K} W(C_k) \tag{2}$$

This function needs to be minimized in order to make the clusters as compact as possible.

Our analysis is based on a K-means clustering algorithm [63]. It groups the positions of cell nuclei iteratively from a previously set number of clusters K. Initially, the positions of the cluster centers are chosen randomly. The distance of each cell to its nearest cluster center is calculated using the Euclidean norm. The algorithm then calculates iteratively new positions of cluster centers to optimize the distances of all cells to their assigned cluster centers, while the number of clusters K is kept constant. Thus, the position of the cluster centers changes in every iteration of the algorithm. The sorting of cells into clusters is finished once the cluster center positions stabilize. The outcome of the K-means algorithm and the quality of the results depend highly on the initial choice of the number of clusters K. Therefore, we performed gap statistics and used the elbow method to verify the credibility of our choice of K.

Determination of the number of cell clusters (1): The optimal number of clusters for each specimen is obtained by employing the elbow method [64]. The K-means algorithm is run for several different numbers of clusters, i.e., values of k. The total within-cluster sum of squares $totW(k)$ is calculated as indicated in the equations above from the sum of squared distances of data points in the cluster and its centroid for all k values. We then find the appropriate k value, i.e., the optimal number of clusters, by plotting $totW(k)$ as a function of k (see Supplementary Materials, Figure S1). This curve starts to flatten at some point and forms an "elbow," which is regarded as an indicator of

the optimal number of clusters. To avoid possible deviations by the correct choice of K from the resulting curves, we compared our results to gap statistics to check our choice of K.

Determination of the number of cell clusters (2): To confirm our results drawn from the elbow method, we additionally used a gap statistic tool in our analysis code. The gap statistic is based on the comparison of within-class variation of real data and what we would expect from a hypothetical uniform data set [65]. To this end, we compared the total within-cluster variation $totW(k)$ of our cell network data with a model of uniformly distributed data points. The Gap for k clusters is calculated as follows:

$$Gap(k) = logtotW_{uni}(k) - logtotW(k) \tag{3}$$

The total within-cluster variation $totW_{uni}(k)$ of the uniform data set is found by a computer simulation of 50 uniformly distributed data sets. The code also measures the standard error $s(k)$ associated with the simulated data sets, and gives the optimal number of clusters K based on this equation:

$$K = min\{k \in \{1, \dots, k_{max}\}: Gap(k) \geq Gap(k+1) - s(k+1)\} \tag{4}$$

We follow the suggestion of Tibshirani et al. [65] and set $s(k) = \sqrt{1 + \frac{1}{50}} sd(k)$ where sd(k) denotes the standard deviation of the 50 Monte-Carlo-simulated data sets.

A graphical illustration of the value $Gap(k)$ as a function of different k values is shown in Figure S2, Supplementary Materials. The optimal number of clusters is represented by the smallest value of k, where the above-mentioned inequality is fulfilled. That means we maximize the Gap value such that $Gap(k)$ is within one standard deviation of the Gap at k + 1.

Cellular grouping within clusters: In addition to these two techniques, we used the silhouette method to check and verify the quality of the grouping of cells into certain clusters [66]. It delivers one of three outcomes of the silhouette coefficient $SilCoef$ for each cell: –1, 0, or + 1. The value 0 means the cell is positioned at the edge of the cluster, –1 corresponds to the cell being assigned to the wrong cluster, and + 1 means we sorted the cell into the correct cluster. The silhouette coefficient is calculated for every cell i as follows:

$$SilCoef(i) = \frac{x(i) - y(i)}{max\{x(i), y(i)\}} \tag{5}$$

where $x(i)$ depicts the smallest mean distance to cells in any other cluster, and $y(i)$ is the mean intracluster distance. A high average silhouette width indicates a good clustering result. Thus, the silhouette method can also be used to check the chosen optimal number of clusters in our experiments. We plotted the mean silhouette width as a function of various values of clusters k. The location of the maximum of that curve is considered to be the optimal number of clusters for the experiment.

From the cluster analysis, the following parameters were extracted for both cell types and all employed substrate materials: The number of cells in each cluster, cluster area, and spatial cell density within clusters.

4.7. Statistical Analysis of Cell Analysis

For both cell types, three specimens per substrate were made for all combinations of the four substrate materials and both cell growth times. In total, we analyzed around 160,000 cells for our investigations.

Averages of data within individual samples or independent experiments were expressed as the arithmetic mean ± standard error of the mean. Statistical significance between data sets was evaluated using the two-sample t-test tool in OriginLab software (OriginPro 2017G, OriginLab Corporation). Values differing by $p \leq 0.05$ were significant, and values differing by $p \leq 0.01$ were considered as highly significant.

5. Conclusions

The importance of in vitro neuron and glial cell experiments as preliminary tests for not only in vivo applications such as neuroelectrodes [67–69] but also as stand-alone research, e.g., to investigate neural activity and neurodegenerative diseases on lab-on-a-chip devices such as multielectrode arrays (MEA), has become apparent lately [70]. This technique has been continuously improved over the past decade [38] and offers great potential to shift expensive and ethically questionable in vivo animal experiments to cost-efficient and easy-to-use high-throughput in vitro assays.

In our study, we showed that fluorescent imaging, to identify the size and position distribution of cell agglomerations in combination with a proliferation assay, is a quantitative tool to measure the biocompatibility of novel biomaterials. In fact, the combination of the K-means clustering algorithm and calculation of the radially averaged autocorrelation function is able to identify the whole range of cell patterns from large dense clusters down to individual and homogeneously distributed cells, giving an individual fingerprint for different cell types. Here, we found nanocolumnar TiN surfaces to perform best in terms of cell division and the network formation characteristic for SH-SY5Y cells. Future studies will focus on the question of how cellular organization on nanocolumnar TiN surfaces correlates with the physiological status of neurons and glial cells. As thin films of nanocolumnar TiN exhibit excellent bioactive properties in combination with optical transparency and low electric resistance, the application of this material in multielectrode arrays will be tested soon.

Supplementary Materials: Figure S1: Result of the application of the elbow method to the data shown in Figures 5 and 6 (SH-SY5Y cells grown on TiN nanocolumnar substrates after 3 days). Figure S2: Result of gap statistics method applied to the data set shown in Figures 5 and 6 (SH-SY5Y cells grown on TiN nanocolumnar substrates after 3 days). Figure S3: Average silhouette width associated with the example from Figures 5 and 6 (SH-SY5Y cells grown on TiN nanocolumnar substrates after 3 days). Supplementary materials can be found at www.mdpi.com/xxx/s1.

Author Contributions: Conceptualization, M.Z.; methodology, A.A., C.S., R.F. and H.-G.J.; software, C.S.; validation, A.A., C.S., H.-G.J. and M.Z.; formal analysis, A.A., C.S. and R.F.; resources, S.S., H.-G.J. and M.Z.; data curation, A.A., C.S., H.-G.J. and M.Z.; writing—original draft preparation, A.A., H.-G.-J. and M.Z.; writing—review and editing, A.A., C.S., H.-G.J. and M.Z.; visualization, A.A.; supervision, H.-G.J. and M.Z.; project administration, M.Z. and H.-G.J.; funding acquisition, M.Z. and H.-G.J. All authors have read and agreed to the published version of the manuscript.

Conflicts of Interest: The authors declare no conflict of interest. The funders had no role in the design of the study; in the collection, analyses, or interpretation of data; in the writing of the manuscript, or in the decision to publish the results.

Abbreviations

Au	Gold
ITO	Indium tin oxide
TiN	Titanium nitride
TiN nano	Titanium nitride nanocolumnar
MEA	Multielectrode array
RMS	Root mean square

References

1. von Bartheld, C.S.; Bahney, J.; Herculano-Houzel, S. The search for true numbers of neurons and glial cells in the human brain: A review of 150 years of cell counting. *J. Comp. Neurol.* **2016**, *524*, 3865–3895, doi:10.1002/cne.24040.

2.   Azevedo, F.A.C.; Carvalho, L.R.B.; Grinberg, L.T.; Farfel, J.M.; Ferretti, R.E.L.; Leite, R.E.P.; Filho, W.J.; Lent, R.; Herculano-Houzel, S. Equal Numbers of Neuronal and Nonneuronal Cells Make the Human Brain an Isometrically Scaled-Up Primate Brain. *J. Comp. Neurol.* **2009**, *513*, 532–541, doi:10.1002/cne.21974.

3.   Adolphs, R. The unsolved problems of neuroscience. *Trends. Cogn. Sci.* **2015**, *19*, 173–175, doi:10.1016/j.tics.2015.01.007.

4.   Calabrese, V.P.; Dorsey, E.R.; Constantinescu, R.; Thompson, J.. P.; Biglan, K.. M.; Holloway, R.. G.; Kieburtz, K.; Marshall, F.. J.; Ravina, B.. M.; Schifitto, G.; et al. Projected number of people with Parkinson disease in the most populous nations, 2005 through 2030. *Neurology* **2007**, *69*, 223–224, doi:10.1212/01.wnl.0000271777.50910.73.

5.   Konnova, E.A.; Swanberg, M. Animal Models of Parkinson's Disease. In *Parkinson's Disease: Pathogenesis and Clinical Aspects*; Stoker, T., Greenland, J., Eds.; Codon Publications: Brisbane, Australia, 2018; pp. 83–106 ISBN 978-0-9944381-6-4.

6.   Humpel, C. Organotypic brain slice cultures: A review. *Neuroscience* **2015**, *305*, 86–98, doi:10.1016/j.neuroscience.2015.07.086.

7.   Kallendrusch, S.; Merz, F.; Bechmann, I.; Mayr, S.G.; Zink, M. Long-Term Tissue Culture of Adult Brain and Spleen Slices on Nanostructured Scaffolds. *Adv. Healthc. Mater.* **2017**, *6*, 2192–2640, doi:10.1002/adhm.201601336.

8.   Slanzi, A.; Iannoto, G.; Rossi, B.; Zenaro, E.; Constantin, G. In vitro Models of Neurodegenerative Diseases. *Front. Cell Dev. Biol.* **2020**, *8*, 328, doi:10.3389/fcell.2020.00328.

9.   Schlachetzki, J.C.M.; Saliba, S.W.; de Oliveira, A.C.P. Studying neurodegenerative diseases in culture models. *Rev. Bras. Psiquiatr.* **2013**, *35*, S92–S100, doi:10.1590/1516-4446-2013-1159.

10. Perlmutter, J.S.; Mink, J.W. Deep Brain Stimulation. *Annu. Rev. Neurosci.* **2006**, *29*, 229–257, doi:10.1146/annurev.neuro.29.051605.112824.

11. Marin, C. Biocompatibility of intracortical microelectrodes: Current status and future prospects. *Front. Neuroeng.* **2010**, *3*, 1–6, doi:10.3389/fneng.2010.00008.

12. Zhang, A.; Lieber, C.M. Nano-Bioelectronics. *Chem. Rev.* **2016**, *116*, 215–257, doi:10.1021/acs.chemrev.5b00608.

13. Torimitsu, K.; Kawana, A. Selective growth of sensory nerve fibers on metal oxide pattern in culture. *Dev. Brain Res.* **1990**, *51*, 128–131, doi:10.1016/0165-3806(90)90265-Z.

14. Fischer, R.A.; Zhang, Y.; Risner, M.L.; Li, D.; Xu, Y.; Sappington, R.M. Impact of Graphene on the Efficacy of Neuron Culture Substrates. *Adv. Healthc. Mater.* **2018**, *7*, 2192–2640, doi:10.1002/adhm.201701290.

15. Ojovan, S.M.; McDonald, M.; Rabieh, N.; Shmuel, N.; Erez, H.; Nesladek, M.; Spira, M.E. Nanocrystalline diamond surfaces for adhesion and growth of primary neurons, conflicting results and rational explanation. *Front. Neuroeng.* **2014**, *7*, 1–9, doi:10.3389/fneng.2014.00017.

16. Turner, S. Cell attachment on silicon nanostructures. *J. Vac. Sci. Technol. B.* **1997**, *15*, 2848–2854, doi:10.1116/1.589742.

17. Jahnke, H.-G.; Schmidt, S.; Frank, R.; Weigel, W.; Prönnecke, C.; Robitzki, A.A. FEM-based design of optical transparent indium tin oxide multielectrode arrays for multiparametric, high sensitive cell based assays. *Biosens. Bioelectron.* **2019**, *129*, 208–215, doi:10.1016/j.bios.2018.09.095.

18. Ni, M.; Tong, W.H.; Choudhury, D.; Rahim, N.A.A.; Iliescu, C.; Yu, H. Cell Culture on MEMS Platforms: A Review. *Int. J. Mol. Sci.* **2009**, *10*, 5411–5441, doi:10.3390/ijms10125411.

19. Selvakumaran, J.; Hughes, M.P.; Keddie, J.L.; Ewins, D.J. Assessing biocompatibility of materials for implantable microelectrodes using cytotoxicity and protein adsorption studies. In Proceedings of the 2nd Annual International IEEE-EMBS Special Topic Conference on Microtechnologies in Medicine and Biology (Cat. No.02EX578), IEEE, Madison, WI, USA, 2–4 May 2002, pp. 261–264.

20. Geninatti, T.; Bruno, G.; Barile, B.; Hood, R.L.; Farina, M.; Schmulen, J.; Canavese, G.; Grattoni, A. Impedance characterization, degradation, and in vitro biocompatibility for platinum electrodes on BioMEMS. *Biomed. Microdevices* **2015**, *17*, 24, doi:10.1007/s10544-014-9909-6.

21. Carnicer-Lombarte, A.; Lancashire, H.T.; Vanhoestenberghe, A. In vitro biocompatibility and electrical stability of thick-film platinum/gold alloy electrodes printed on alumina. *J. Neural Eng.* **2017**, *14*, 036012, doi:10.1088/1741-2552/aa6557.

22. Kim, M.-H.; Park, M.; Kang, K.; Choi, I.S. Neurons on nanometric topographies: Insights into neuronal behaviors in vitro. *Biomater. Sci.* **2014**, *2*, 148–155, doi:10.1039/C3BM60255A.

23. Craighead, H.G.; James, C.D.; Turner, A.M.P. Chemical and topographical patterning for directed cell attachment. *Curr. Opin. Solid State Mater. Sci.* **2001**, *5*, 177–184, doi:10.1016/S1359-0286(01)00005-5.

24. Goldner, J.S.; Bruder, J.M.; Li, G.; Gazzola, D.; Hoffman-Kim, D. Neurite bridging across micropatterned grooves. *Biomaterials* **2006**, *27*, 460–472, doi:10.1016/j.biomaterials.2005.06.035.

25. Dowell-Mesfin, N.M.; Abdul-Karim, M.-A.; Turner, A.M.P.; Schanz, S.; Craighead, H.G.; Roysam, B.; Turner, J.N.; Shain, W. Topographically modified surfaces affect orientation and growth of hippocampal neurons. *J. Neural Eng.* **2004**, *1*, 78–90, doi:10.1088/1741-2560/1/2/003.

26. Hanson, J.N.; Motala, M.J.; Heien, M.L.; Gillette, M.; Sweedler, J.; Nuzzo, R.G. Textural guidance cues for controlling process outgrowth of mammalian neurons. *Lab. Chip* **2009**, *9*, 122–131, doi:10.1039/B803595D.

27. Brunetti, V.; Maiorano, G.; Rizzello, L.; Sorce, B.; Sabella, S.; Cingolani, R.; Pompa, P.P. Neurons sense nanoscale roughness with nanometer sensitivity. *Proc. Natl. Acad. Sci. USA.* **2010**, *107*, 6264–6269, doi:10.1073/pnas.0914456107.

28. Li, Z.; Persson, H.; Adolfsson, K.; Oredsson, S.; Prinz, C.N. Morphology of living cells cultured on nanowire arrays with varying nanowire densities and diameters. *Sci. China Life Sci.* **2018**, *61*, 427–435, doi:10.1007/s11427-017-9264-2.

29. Hällström, W.; Mårtensson, T.; Prinz, C.; Gustavsson, P.; Montelius, L.; Samuelson, L.; Kanje, M. Gallium Phosphide Nanowires as a Substrate for Cultured Neurons. *Nano Lett.* **2007**, *7*, 2960–2965, doi:10.1021/nl070728e.

30. Moyen, E.; Hama, A.; Ismailova, E.; Assaud, L.; Malliaras, G.; Hanbücken, M.; Owens, R.M. Nanostructured conducting polymers for stiffness controlled cell adhesion. *Nanotechnology* **2016**, *27*, 074001, doi:10.1088/0957-4484/27/7/074001.

31. Keefer, E.W.; Botterman, B.R.; Romero, M.I.; Rossi, A.F.; Gross, G.W. Carbon nanotube coating improves neuronal recordings. *Nat. Nanotechnol.* **2008**, *3*, 434–439, doi:10.1038/nnano.2008.174.

32. Chen, N.; Luo, B.; Patil, A.C.; Wang, J.; Gammad, G.G.L.; Yi, Z.; Liu, X.; Yen, S.; Ramakrishna, S.; Thakor, N. V Nanotunnels within Poly(3,4-ethylenedioxythiophene)-Carbon Nanotube Composite for Highly Sensitive Neural Interfacing. *ACS Nano* **2020**, doi:10.1021/acsnano.0c00672.

33. Ji, Y.-R.; Homaeigohar, S.; Wang, Y.; Lin, C.; Su, T.-Y.; Cheng, C.-C.; Yang, S.-H.; Young, T.-H. Selective Regulation of Neurons, Glial Cells, and Neural Stem/Precursor Cells by Poly(allylguanidine)-Coated Surfaces. *ACS Appl. Mater. Interfaces* **2019**, *11*, 48381–48392, doi:10.1021/acsami.9b17143.

34. Sánchez, G.; Dalchiele, E.; Bologna Alles, A. Electrical characterization of titanium nitride surfaces for pacing electrodes. *J. Mater. Sci.* **2006**, *41*, 3241–3247, doi:10.1007/s10853-005-5477-8.

35. Krinke, D.; Jahnke, H.-G.; Pänke, O.; Robitzki, A.A. A microelectrode-based sensor for label-free in vitro detection of ischemic effects on cardiomyocytes. *Biosens. Bioelectron.* **2009**, *24*, 2798–2803, doi:10.1016/j.bios.2009.02.006.

36. Suni, I.I. Impedance methods for electrochemical sensors using nanomaterials. *TrAC Trends Anal. Chem.* **2008**, *27*, 604–611, doi:10.1016/j.trac.2008.03.012.

37. Cui, X.; Martin, D.C. Fuzzy gold electrodes for lowering impedance and improving adhesion with electrodeposited conducting polymer films. *Sensors Actuators A Phys.* **2003**, *103*, 384–394, doi:10.1016/S0924-4247(02)00427-2.

38. Jahnke, H.-G.; Krinke, D.; Seidel, D.; Lilienthal, K.; Schmidt, S.; Azendorf, R.; Fischer, M.; Mack, T.; Striggow, F.; Althaus, H.; et al. A novel 384-multiwell microelectrode array for the impedimetric monitoring of Tau protein induced neurodegenerative processes. *Biosens. Bioelectron.* **2017**, *88*, 78–84, doi:10.1016/j.bios.2016.07.074.

39. Seymour, J.P.; Wu, F.; Wise, K.D.; Yoon, E. State-of-the-art MEMS and microsystem tools for brain research. *Microsystems Nanoeng.* **2017**, *3*, 16066, doi:10.1038/micronano.2016.66.

40. Hasan, M.; Berdichevsky, Y. Neural Circuits on a Chip. *Micromachines* **2016**, *7*, 157, doi:10.3390/mi7090157.

41. Craighead, H. Future lab-on-a-chip technologies for interrogating individual molecules. *Nature* **2006**, *442*, 387–393, doi:10.1038/nature05061.

42. Xicoy, H.; Wieringa, B.; Martens, G.J.M. The SH-SY5Y cell line in Parkinson's disease research: A systematic review. *Mol. Neurodegener.* **2017**, *12*, 10, doi:10.1186/s13024-017-0149-0.

43. Zink, M.; Samwer, K.; Johnson, W.L.; Mayr, S.G. Plastic deformation of metallic glasses: Size of shear transformation zones from molecular dynamics simulations. *Phys. Rev. B. Condens. Matter Mater. Phys.* **2006**, *73*, 2–4, doi:10.1103/PhysRevB.73.172203.

44. Pan, Y. Le; Berg, M.J.; Zhang, S.S.M.; Noh, H.; Cao, H.; Chang, R.K.; Videen, G. Measurement and autocorrelation analysis of two-dimensional light-scattering patterns from living cells for label-free classification. *Cytom. Part. A* **2011**, *79*, 284–292, doi:10.1002/cyto.a.21036.

45. Kim, G.; Kim, K.; Lee, E.; An, T.; Choi, W.; Lim, G.; Shin, J. Recent Progress on Microelectrodes in Neural Interfaces. *Materials (Basel).* **2018**, *11*, 1995, doi:10.3390/ma11101995.

46. Baker, D.R.; Sirbescu, M.-L.; Maneta, V.; Webber, K.L.; Simmons, W.B. Quantitative Analysis of Natural and Experimental Graphic Textures. *Can. Mineral.* **2018**, *56*, 625–643, doi:10.3749/canmin.1700084.

47. Vallejo-Giraldo, C.; Pampaloni, N.P.; Pallipurath, A.R.; Mokarian-Tabari, P.; O'Connell, J.; Holmes, J.D.; Trotier, A.; Krukiewicz, K.; Orpella-Aceret, G.; Pugliese, E.; et al. Preparation of Cytocompatible ITO Neuroelectrodes with Enhanced Electrochemical Characteristics Using a Facile Anodic Oxidation Process. *Adv. Funct. Mater.* **2018**, *28*, 1605035, doi:10.1002/adfm.201605035.

48. Schouenborg, J.; Garwicz, M.; Danielsen, N. *Brain Machine Interfaces: Implications for Science, Clinical Practice and Society*; Schouenborg, J., Garwicz, M., Danielsen, N., Eds.; Elsevier Science : Amsterdam, Netherlands, 2011; Vol. 194, pp. 2–282. ISBN 9780444538161.

49. Chan-Ling, T.; Stone, J. Factors determining the morphology and distribution of astrocytes in the cat retina: A "contact-spacing" model of astrocyte interaction. *J. Comp. Neurol.* **1991**, *303*, 387–399, doi:10.1002/cne.903030305.

50. Ogata, K.; Kosaka, T. Structural and quantitative analysis of astrocytes in the mouse hippocampus. *Neuroscience* **2002**, *113*, 221–233, doi:10.1016/S0306-4522(02)00041-6.

51. Bushong, E.A.; Martone, M.E.; Jones, Y.Z.; Ellisman, M.H. Protoplasmic Astrocytes in CA1 Stratum Radiatum Occupy Separate Anatomical Domains. *J. Neurosci.* **2002**, *22*, 183–192, doi:10.1523/JNEUROSCI.22-01-00183.2002.

52. Nedergaard, M.; Ransom, B.; Goldman, S.A. New roles for astrocytes: Redefining the functional architecture of the brain. *Trends Neurosci.* **2003**, *26*, 523–530, doi:10.1016/j.tins.2003.08.008.

53. Khan, S.P.; Auner, G.G.; Newaz, G.M. Influence of nanoscale surface roughness on neural cell attachment on silicon. *Nanomed. Nanotechnol. Biol. Med.* **2005**, *1*, 125–129, doi:10.1016/j.nano.2005.03.007.

54. Fan, Y.W.; Cui, F.Z.; Chen, L.N.; Zhai, Y.; Xu, Q.Y.; Lee, I.S. Adhesion of neural cells on silicon wafer with nano-topographic surface. *Appl. Surf. Sci.* **2002**, *187*, 313–318, doi:10.1016/S0169-4332(01)01046-7.

55. Yoon, S.-B.; Lee, G.; Park, S.B.; Cho, H.; Lee, J.-O.; Koh, B. Properties of differentiated SH-SY5Y grown on carbon-based materials. *RSC Adv.* **2020**, *10*, 19382–19389, doi:10.1039/D0RA03383A.

56. Shipley, M.M.; Mangold, C.A.; Szpara, M.L. Differentiation of the SH-SY5Y Human Neuroblastoma Cell Line. *J. Vis. Exp.* **2016**, 1–12, doi:10.3791/53193.

57. Piret, G.; Perez, M.-T.; Prinz, C.N. Neurite outgrowth and synaptophysin expression of postnatal CNS neurons on GaP nanowire arrays in long-term retinal cell culture. *Biomaterials* **2013**, *34*, 875–887, doi:10.1016/j.biomaterials.2012.10.042.

58. Piret, G.; Perez, M.-T.; Prinz, C.N. Substrate porosity induces phenotypic alterations in retinal cells cultured on silicon nanowires. *RSC Adv.* **2014**, *4*, 27888–27897, doi:10.1039/C4RA04121F.

59. Jalava, A.; Åkerman, K.; Heikkilä, J. Protein kinase inhibitor, staurosporine, induces a mature neuronal phenotype in SH-SY5Y human neuroblastoma cells through an α-, β-, and ζ-protein kinase C-independent pathway. *J. Cell. Physiol.* **1993**, *155*, 301–312, doi:10.1002/jcp.1041550211.

60. Schindelin, J.; Arganda-Carreras, I.; Frise, E.; Kaynig, V.; Longair, M.; Pietzsch, T.; Preibisch, S.; Rueden, C.; Saalfeld, S.; Schmid, B.; et al. Fiji: An open-source platform for biological-image analysis. *Nat. Methods* **2012**, *9*, 676–682, doi:10.1038/nmeth.2019.

61. Schindelin, J.; Rueden, C.T.; Hiner, M.C.; Eliceiri, K.W. The ImageJ ecosystem: An open platform for biomedical image analysis. *Mol. Reprod. Dev.* **2015**, *82*, 518–529, doi:10.1002/mrd.22489.

62. Berryman, J.G. Measurement of spatial correlation functions using image processing techniques. *J. Appl. Phys.* **1985**, *57*, 2374–2384, doi:10.1063/1.334346.

63. MacQueen, J. Some methods for classification and analysis of multivariate observations. In *Proceedings of the fifth Berkeley symposium on mathematical statistics and probability*; Lecam, L., Neyman, J., Eds.; University of California Press: Oakland, CA, USA, 1967; pp. 281--297.

64. Thorndike, R.L. Who belongs in the family? *Psychometrika* **1953**, *18*, 267–276, doi:10.1007/BF02289263.

65. Tibshirani, R.; Walther, G.; Hastie, T. Estimating the number of clusters in a data set via the gap statistic. *J. R. Stat. Soc.* **2001**, *63*, 411–423, doi:10.1111/1467-9868.00293.

66. Rousseeuw, P.J. Silhouettes: A graphical aid to the interpretation and validation of cluster analysis. *J. Comput. Appl. Math.* **1987**, *20*, 53–65, doi:10.1016/0377-0427(87)90125-7.

67. Aparicio-Blanco, J.; Martín-Sabroso, C.; Torres-Suárez, A.-I. In vitro screening of nanomedicines through the blood brain barrier: A critical review. *Biomaterials* **2016**, *103*, 229–255, doi:10.1016/j.biomaterials.2016.06.051.

68. Gilmour, A.D.; Woolley, A.J.; Poole-Warren, L.A.; Thomson, C.E.; Green, R.A. A critical review of cell culture strategies for modelling intracortical brain implant material reactions. *Biomaterials* **2016**, *91*, 23–43, doi:10.1016/j.biomaterials.2016.03.011.

69. Brown, J.; Quadrato, G.; Arlotta, P. Studying the Brain in a Dish: 3D Cell Culture Models of Human Brain Development and Disease. In *Current Topics in Developmental Biology*; Brivanlou, A.H., Eds.; Elsevier Inc: Amsterdam, Netherlands 2018; Vol. 129, pp. 99–122. ISBN 9780128042519.

70. Spira, M.E.; Hai, A. Multi-electrode array technologies for neuroscience and cardiology. *Nat. Nanotechnol.* **2013**, *8*, 83–94, doi:10.1038/nnano.2012.265.

Supplementary Materials

Proliferation and Cluster Analysis of Neurons and Glial Cell Organization on Nanocolumnar TiN Substrates

Alice Abend [1], Chelsie Steele [1], Sabine Schmidt [2], Ronny Frank [2], Heinz-Georg Jahnke [2,*] and Mareike Zink [1,*]

[1] Soft Matter Physics Division and Biotechnology & Biomedical Group, Peter-Debye-Institute for Soft Matter, Physics, Leipzig University, Linnéstr. 5, 04103 Leipzig, Germany; alice.abend@uni-leipzig.de (AA); cs73gygu@studserv.uni-leipzig.de (CS); zink@physik.uni-leipzig.de (MZ)

[2] Centre for Biotechnology and Biomedicine, Molecular Biological-biochemical Processing Technology, Leipzig University, Deutscher Platz 5, 04103 Leipzig, Germany; sabine.schmidt@bbz.uni-leipzig.de (SS); ronny.frank@bbz.uni-leipzig.de (RF); heinz-georg.jahnke@bbz.uni-leipzig.de (HGJ)

* Correspondence: zink@physik.uni-leipzig.de (MZ), heinz-georg.jahnke@bbz.uni-leipzig.de (HGJ); Tel.: +49 (341) 9732573, +49 (341) 9731246 (HGJ) (MZ); Fax: +49 (341) 9732479 (MZ), +49 (341) 9731249 (HGJ)
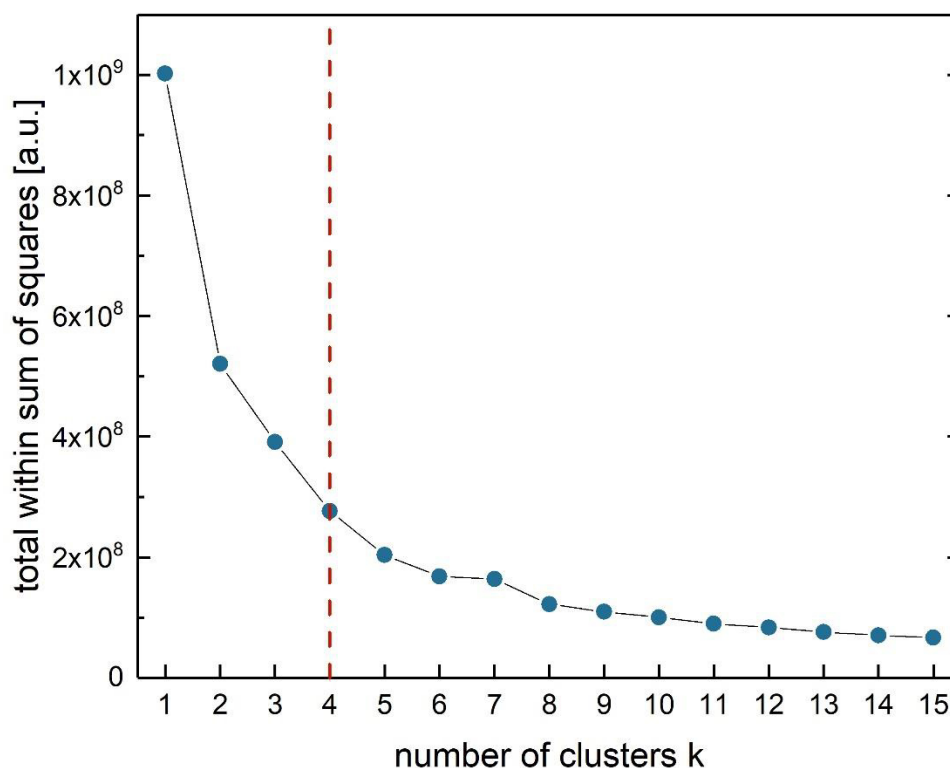
Figure S1: Result of the application of the elbow method to the data shown in Figures 5 and 6 (SH-SY5Y cells grown on TiN nanocolumnar substrates after 3 days). The red dashed line marks the optimal number of clusters k=4 for this example.
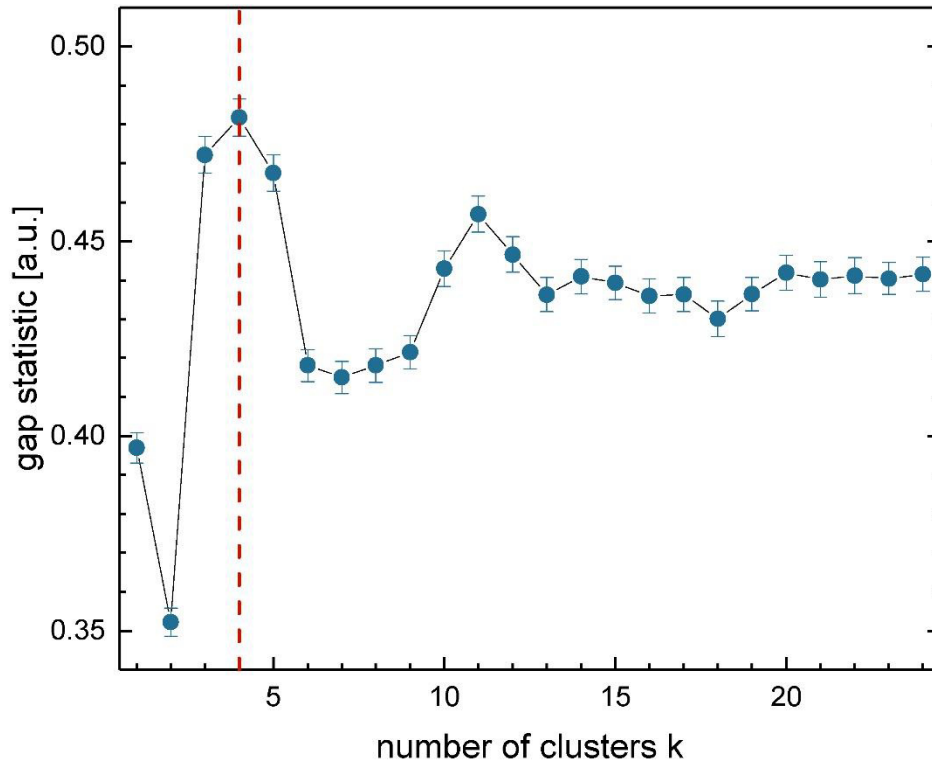
Figure S2: Result of gap statistics method applied to the data set shown in Figures 5 and 6 (SH-SY5Y cells grown on TiN nanocolumnar substrates after 3 days). The value $Gap(k)$ was calculated according to Equation 3. The optimal number of clusters (red dashed line) is found to be k=4 in this case indicated by the peak of the graph. Most of our gap statistics graphs show this distinct maximum and thus reveal a reliable result for the optimal number of clusters. The gap statistics curve could theoretically also exhibit a slowly ascending and then flattening form so that the condition $Gap(k) \geq Gap(k + 1)$ is never fulfilled. Therefore, this condition is extended by the standard deviation term in Equation 4. The condition $Gap(k) \geq Gap(k + 1) - s(k + 1)$ can usually be fulfilled somewhere in the graph.
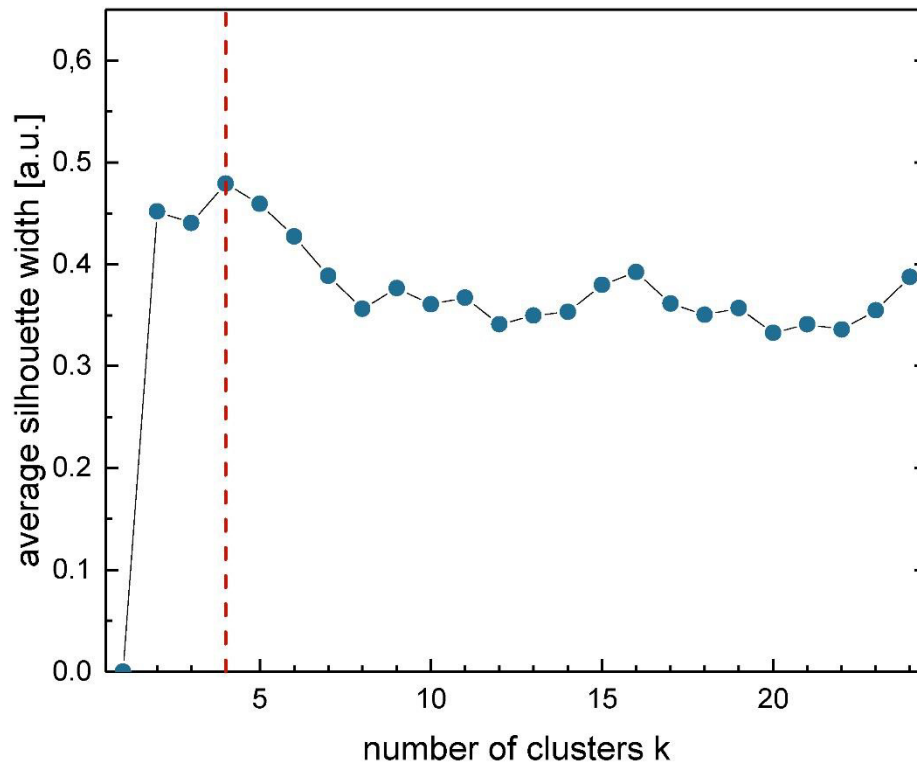
Figure S3: Average silhouette width associated with the example from Figures 5 and 6 (SH-SY5Y cells grown on TiN nanocolumnar substrates after 3 days). The maximum of the curve represents the optimal number of clusters for this experiment (red dashed line). We therewith verify our results drawn from the elbow method and gap statistics (see Figures S1 and S2).

3.2. Adhesion of Neurons and Glial Cells with Nanocolumnar TiN Films for Brain-Machine Interfaces

The content of this chapter has been published in the manuscript "Adhesion of Neurons and Glial Cells with Nanocolumnar TiN Films for Brain-Machine Interfaces" [148].

Article

Adhesion of Neurons and Glial Cells with Nanocolumnar TiN Films for Brain-Machine Interfaces

Alice Abend [1,*], Chelsie Steele [1], Heinz-Georg Jahnke [2] and Mareike Zink [1,*]

[1] Research Group Biotechnology and Biomedicine, Faculty of Physics and Earth Sciences, Peter Debye Institute for Soft Matter Physics, Leipzig University, Linnéstraße 5, 04103 Leipzig, Germany; cs73gygu@studserv.uni-leipzig.de

[2] Centre for Biotechnology and Biomedicine, Molecular Biological-Biochemical Processing Technology, Leipzig University, Deutscher Platz 5, 04103 Leipzig, Germany; heinz-georg.jahnke@bbz.uni-leipzig.de

[*] Correspondence: alice.abend@uni-leipzig.de (A.A.); zink@physik.uni-leipzig.de (M.Z.); Tel.: +49-(341)-973-2561 (A.A.); Tel.: +49-(341)-973-2573 (M.Z.)

Abstract: Coupling of cells to biomaterials is a prerequisite for most biomedical applications; e.g., neuroelectrodes can only stimulate brain tissue in vivo if the electric signal is transferred to neurons attached to the electrodes' surface. Besides, cell survival in vitro also depends on the interaction of cells with the underlying substrate materials; in vitro assays such as multielectrode arrays determine cellular behavior by electrical coupling to the adherent cells. In our study, we investigated the interaction of neurons and glial cells with different electrode materials such as TiN and nanocolumnar TiN surfaces in contrast to gold and ITO substrates. Employing single-cell force spectroscopy, we quantified short-term interaction forces between neuron-like cells (SH-SY5Y cells) and glial cells (U-87 MG cells) for the different materials and contact times. Additionally, results were compared to the spreading dynamics of cells for different culture times as a function of the underlying substrate. The adhesion behavior of glial cells was almost independent of the biomaterial and the maximum growth areas were already seen after one day; however, adhesion dynamics of neurons relied on culture material and time. Neurons spread much better on TiN and nanocolumnar TiN and also formed more neurites after three days in culture. Our designed nanocolumnar TiN offers the possibility for building miniaturized microelectrode arrays for impedance spectroscopy without losing detection sensitivity due to a lowered self-impedance of the electrode. Hence, our results show that this biomaterial promotes adhesion and spreading of neurons and glial cells, which are important for many biomedical applications in vitro and in vivo.

Keywords: neurons; glial cells; electrode materials; cell adhesion; cell spreading; TiN; nanostructured surfaces; cell-surface interaction; neuroelectrode

1. Introduction

Many cellular processes such as proliferation and migration rely on the ability of cells to adhere to a surrounding medium such as the extracellular matrix (ECM) or a biomaterial [1]. In vivo cells mainly connect to the ECM, which constitutes different proteins with specific binding sites for cellular adhesion. In contact with a biomaterial composed of metals or ceramics, these proteins are missing. However, cells express specific proteins, such as fibronectin or laminin, which can then be deposited onto the biomaterial. This enables the cells to form specific adhesion points via surface receptors connecting to the previously deposited proteins. First adhesion sites for cells in contact with biomaterials can occur within seconds when early focal complexes form [2]. Subsequently, maturation of this soft binding step to focal adhesion results in specific adhesion sites in which cellular adhesion receptors interact with ECM molecules and form mature adhesion complexes [2,3].

Within the last decade, a large variety of biomaterials have been developed, ranging from diagnostic tools [4] to dental [5] and orthopedic implants [6], organ replacement [7],

and tissue engineering [8] to vascular grafts [9] and pharmaceutical applications [10]. Nevertheless, the functioning of medical devices and implants relies on good integration and cellular adhesion in vivo. In terms of neuroelectrodes used for deep brain stimulation to treat diseases such as Parkinson's disease [11] or treatment-resistant depression [12], the coupling of neurons to the electrode is crucial for electric signal transfer. However, a mechanical mismatch of the stiff electrode which exhibits Young's moduli in the range of GPa and the soft brain tissue often generates inflammatory responses and the formation of scar tissue around the electrode, causing degradation of recording and implant failure [13,14]. Additionally, glial scarring hinders regeneration of neurons after local injury, which inevitably has to be accepted after implantation of the electrode [15]. Alternatively, soft [16,17] and bioinspired electrodes [18,19] can overcome this drawback, while implantation strategies are still a matter of debate [20]. Nevertheless, electronic features such as low impedance, and a suitable signal-to-noise ratio have to be ensured. Other strategies employ nanotechnology to reduce scar formation by optimization of neural electrode-tissue interfaces, including carbon nanotube fiber-based surfaces [21] and nano-coatings [21,22].

Brain-machine interfaces such as lab-on-a-chip devices and multielectrode arrays (MEA) also offer great potential for in vitro and in vivo application to study neuronal circuit-connectivity, physiology, and pathology [23]. As recently shown by Vafaiee et al., carbon nanotube modified microelectrode arrays show improved electric properties important for neural interfaces [24]. Currently, 384-multiwell microelectrode arrays are used for the impedimetric monitoring of Tau protein-induced neurodegenerative processes [25]. To further miniaturize future brain-machine interfaces, electric materials with a lowered self-impedance of the electrode are required. A possible candidate is titanium nitride (TiN), which exhibits an increased surface area and allows the shrinking of microelectrode size without losing detection sensitivity [26–29]. By further increasing the surface area of TiN with a nanocolumnar pattern, we have previously shown that neurons and glial cells cultured on these surfaces exhibit a much better proliferation behavior, in contrast to conventional electrode materials such as gold and indium-tin-oxide (ITO) [30]. In addition to research on multielectrode arrays, the functional properties of primary cortical neurons and neuron-like cells have also been studied on promising organic [31–34], as well as inorganic [35], memristive brain-machine interfaces.

The formation of glial scars is not present during in vitro application in MEA devices when investigating neurons in a cell culture system. However, adequate coupling of neurons to the underlying MEA is still a major prerequisite in order for neural recording to become possible. Additionally, in terms of neuron-surface interaction, understanding cell adhesion in terms of response and control of cellular interaction with their environment is an important feature during repair mechanisms and possible medical treatment related to diseases of the central and peripheral nervous systems [36]. Thus, promoting neuron adhesion and growth on a biomaterial is an ongoing task.

In our study, we investigated the short-term adhesion behavior of human neuron-like SH-SY5Y and glial-like U-87 MG cells on several electrode materials (TiN, nanocolumnar TiN, ITO, and gold) using atomic force microscopy-based single-cell force spectroscopy. To this end, we analyzed the maximum adhesion force of single cells and measured the total work required to completely detach the cell from the substrate to quantify the bioactivity of the different surfaces. Adhesion on longer time scales goes in line with maturation of specific cell-surface binding sites, e.g., via integrin receptors [37] which correlates with cell spreading and the formation of neurites. Therefore, we further studied the dynamics of spreading and changes in cell growth areas over several days of cultured SH-SY5Y and U-87 MG cells. While the adhesion and spreading behavior of the glial cells was almost independent of the investigated electrode materials, the neurons showed an enhanced cell spreading on TiN and nanocolumnar TiN in contrast to ITO and gold. Additionally, glial cells already developed their maximum growth areas after one day in culture: neurons needed more time to spread, and the final growth areas were observed after 3 days. Together with the observation that the neurons proliferated much better

on TiN and nanocolumnar TiN, as well as formed clusters and agglomerations on these surfaces (a hint for improved physiologic behavior as shown before), our study reveals that nanocolumnar TiN exhibits suitable bioactive properties together with enhanced electric features important for brain-machine interfaces.

2. Results

We investigated the short-term adhesion behavior of U-87 MG and SH-SY5Y cells on several electrode materials (see Figure S1 for information on surface topography, Supplementary Material) using single-cell force spectroscopy for both 5 s and 30 s cell contact times on TiN and nanocolumnar TiN, as well as Au and ITO substrates as control. Representative examples of the resulting force-distance curves are shown in Figure 1. We noticed that characteristic plateau-shaped retract curves mainly occurred for U-87 MG cells (see Figure 1a). The tearing off process while pulling the cell upwards away from the surface happened for the SH-SY5Y cells, usually at much smaller distances from the substrate than for U-87 MG cells. For these cells, we usually observed a single rupture event instead of multiple plateaus as shown in Figure 1b.
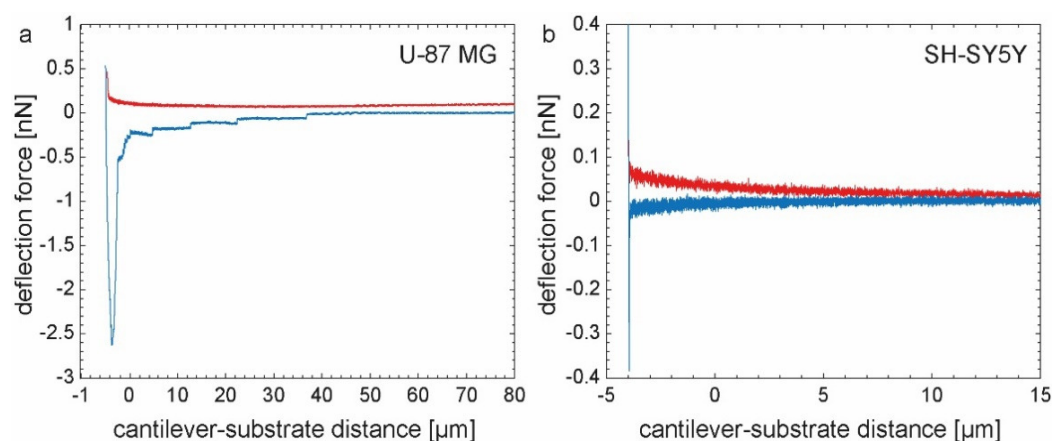

Figure 1. (**a**) Representative example of a force-distance curve of a U-87 MG cell in contact with a TiN substrate. The approach segment is shown in red and the blue graph indicates the retraction of the cell from the sample. The minimum of the retract segment corresponds to the maximum adhesion force; (**b**) Same experiment as in (**a**) but measured with a SH-SY5Y cell.

We analyzed the maximum adhesion forces exerted by the cells while being detached from the substrate. The mean values for each cell normalized by the average contact area are shown in Figure 2a,b. We observed that the maximum adhesion values are generally higher for longer contact times for both cell types and all materials. Gold showed the lowest adhesion forces for both neuronal and glial cells with 3.8 pN and 5.4 pN for 5 s contact time, respectively, as well as 7.1 pN and 6.5 pN for 30 s contact time, respectively. The largest adhesion force was found for glial cells on ITO after 30 s with a value of 20.4 pN compared to 8.6 pN for 5 s, while for the neuronal cell type the adhesion force increased from 8.3 pN after 5 s to 12.5 pN after 30 s contact time. TiN and nanocolumnar TiN both delivered a comparable ratio of adhesion forces for U-87 MG and SH-SH5Y cells for different contact times. However, neurons generally comprised comparatively higher adhesion forces on the nanocolumnar TiN surface (12.1 pN for 30 s) with very similar forces as found for the glial cells (12.9 pN for 30 s).
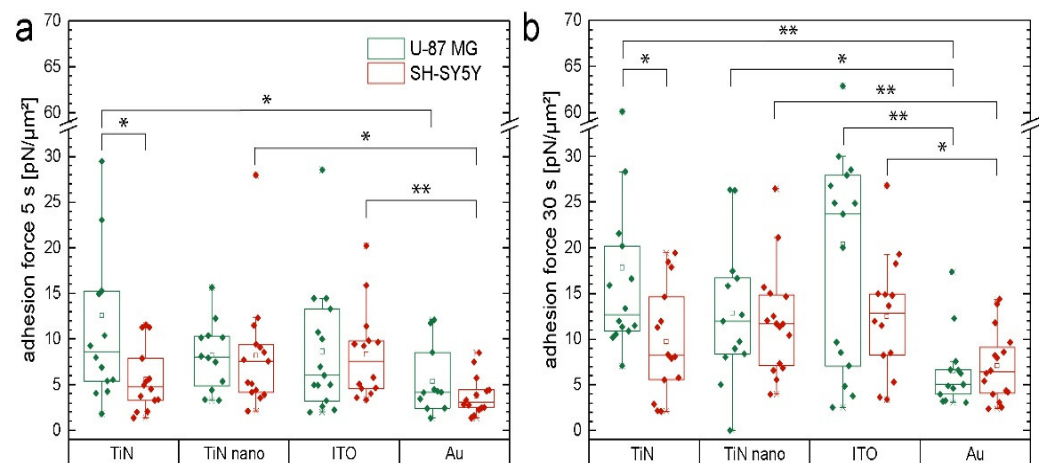
Figure 2. (**a**) Maximal adhesion force of single U-87 MG (green) and SH-SY5Y (red) cells measured with a contact time of 5 s on different electrode materials (TiN, nanocolumnar TiN, ITO, Au); (**b**) Same as in (**a**) but with a contact time of 30 s. We marked data values as significant (*) for $p \leq 0.05$ and highly significant (**) for $p \leq 0.01$.

In addition to the maximal adhesion forces, we also studied the total work required to completely detach a single cell from the electrode substrate, i.e., the area between the retract part of the force-distance curve and the baseline. The mean values for each cell are presented in Figure 3a,b with a logarithmic scale. This detachment work represents the overall cell adhesion because it includes every single separation event while pulling the cell upwards away from the electrode substrate. Interestingly, glial cells generally exhibited a broader distribution of data points with more outliers in comparison to their neuronal counterparts. The electrode material gold shows the lowest median values for SH-SY5Y cells for both adhesion times (with 1.5×10^{-4} fJ/μm^2 for 5 s and 4.7×10^{-4} fJ/μm^2 for 30 s contact time), whereas the U-87 MG cells seemed to adhere much stronger to this substrate type with 1.9×10^{-3} fJ/μm^2 for 30 s and 1.4×10^{-2} fJ/μm^2 for 5 s adhesion time. Comparing the two TiN materials, neurons adhered weaker regarding the detachment work on TiN than nanocolumnar TiN. We see the highest median value of the detachment work on nanocolumnar TiN for SH-SY5Y for 5 s contact time with 1.1×10^{-3} fJ/μm^2. On the other hand, U-87 MG cells exhibited their second-poorest adhesion behavior with a median detachment work of 1.1×10^{-3} fJ/μm^2 on nanocolumnar TiN, right behind ITO with a value of 1.7×10^{-3} fJ/μm^2 for 30 s contact time.
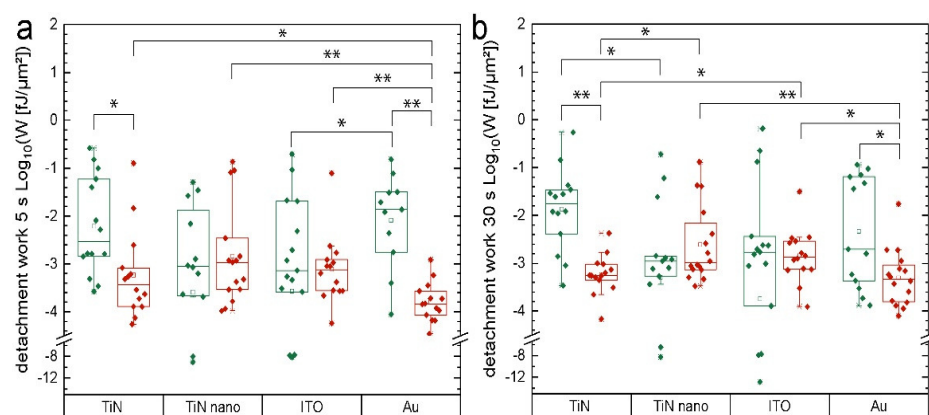

Figure 3. (**a**) Total work required to completely detach a single cell from the electrode substrate with a contact time of 5 s. Results of U-87 MG cells are shown in green and SH-SY5Y cells in red; (**b**) Same as in (**a**) but with a contact time of 30 s. We marked data values as significant (*) for $p \leq 0.05$ and highly significant (**) for $p \leq 0.01$.

Additionally, with regards to the analysis of the single-cell short-term adhesion behavior, we also investigated the spreading of cells in networks over longer time scales of several days cultured on the electrode materials. Cell spreading, and thereby increase of cell size, is usually coupled to an increased number of adhesion points, which in turn leads to enhanced cell adhesion and improved bioactivity of the underlying substrate material [38,39]. Here, we measured the size of actin phalloidin labeled U-87 MG and SH-SY5Y cells, viz. the projected cell areas grown on TiN, TiN nano, ITO, and gold electrode substrates for one day and three days, respectively. Examples of the fluorescent images of actin fibers of SH-SY5Y and U-87 MG cells grown on ITO and TiN nano that were used for these experiments are shown in Figure 4 and Figure S2, Supplementary Materials. Results of the projected cell area analysis are presented in Figure 5.
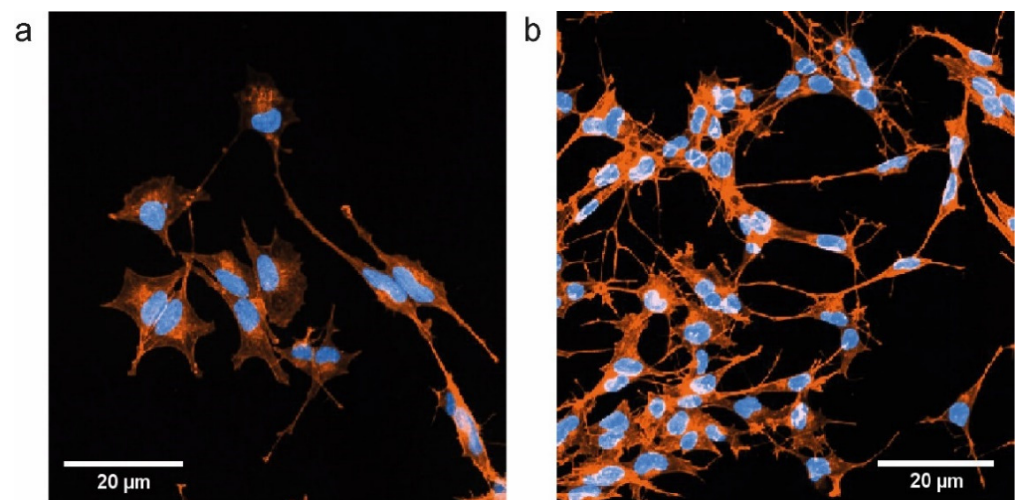

Figure 4. (**a**) Fluorescence image of SH-SY5Y cells grown on ITO substrate for 3 days. Actin fibers are shown in orange and cell nuclei in blue; (**b**) Same as in (**a**) for cells cultured on nanocolumnar TiN.
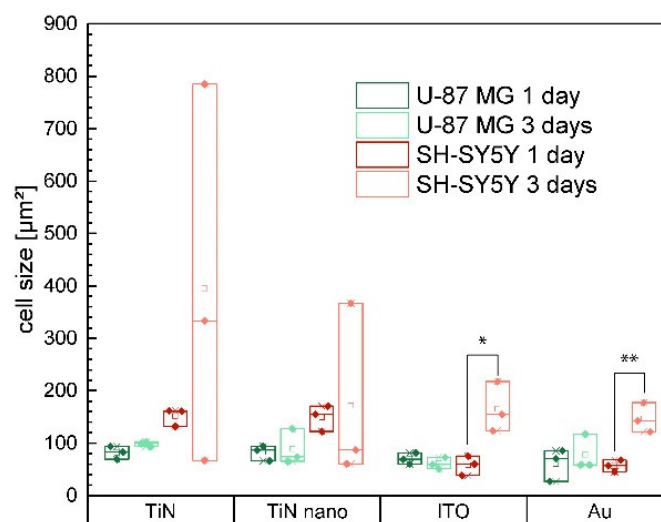

Figure 5. Cell size (viz. projected cell areas) on different substrate materials extracted from fluorescent images of actin phalloidin labeled glial U-87 MG (green) and neuronal SH-SY5Y (red) cells for different growth times. We marked data values as significant (*) for $p \leq 0.05$ and highly significant (**) for $p \leq 0.01$.

The size of U-87 MG cells after 1 day of culture was almost identical for all substrate materials with values around 90 μm^2. After 3 days, cell areas hardly increased due to spreading and only small differences became visible. In fact, on ITO, the cell area mean value decreased by around 13% after 3 days compared to 1 day, while on TiN an increase of around 20% was observed.

In contrast, the growth areas of neurons increased strongly from day 1 to day 3 on ITO and Au. We also observed much larger cells on TiN and TiN nano, while on both materials there was great variation of cell sizes after 3 days. Thus, on both materials, cells were found much smaller than seen after 1 day, as well as cell sizes up to 5 times larger. On TiN, the mean value doubled from day 1 to day 3, while on TiN nano, the mean value decreased. Even though very large cells were seen on TiN nano, the number of very small cells was highest. Since the SH-SY5Y cells organized in clusters on the TiN and TiN nano surface in contrast to ITO and Au [30], cells in the center of the clusters could not be included in our evaluation because of the high density, which resulted in optical separation of adjacent cells becoming impossible. Thus, our evaluation only included cells in less dense areas, viz. in the vicinity of cluster centers.

3. Discussion

In our study, we investigated the adhesion behavior of both human neuron-like SH-SY5Y and glial-like U-87 MG cells on short time scales of seconds. To this end, single-cell force spectroscopy with cell-material adhesion times of 5 s and 30 s was used to obtain data on the cells' maximum adhesion force, as well as the work required to completely detach a single cell from the electrode substrate. In our experiments, we do not take wetting behavior effects into account (viz. spreading of cells in contact with a surface due to surface tension effects when cells are considered liquid-like [40]) since the force spectroscopy microscope actively pushes the cell onto the electrode substrate with a constant setpoint of 500 pN, and then sustains the reached z-position for the adhesion time of either 5 s or 30 s, respectively. The results were normalized to the cell-material contact area (see Materials and Methods) to exclude the influence of sheer cell size, which likely correlates with the number of formed adhesion points and therewith adhesion force itself [41]. As expected [42], we found higher values of the cell-substrate adhesion force for both cell lines on all materials for the longer contact time. Our results show the lowest adhesion forces on gold substrates for both neuronal and glial cells. Since bad cell adhesion can also reduce proliferation, our results go in line with our previous findings that neurons and glial cells show a reduced proliferation rate on gold compared to ITO, TiN, and nanocolumnar TiN [30]. However, reduced proliferation rates could also be partly attributed to the influence of differentiative processes on the neuron-like SH-SY5Y cells caused by the surface nanotopography of the substrate material as shown recently [43–45]. Optically judging from Figure 4, we did indeed notice differences in the differentiation state of SH-SY5Y cells on particular electrode materials.

Additionally, we noticed an overall broader distribution of adhesion force and detachment work values for U-87 MG cells than SH-SY5Y cells. As previously shown by Dao et al. for CHO cells [46], cell adhesion variability stems from cell to cell variation within populations and does not depend on changes of adhesion behavior of single cells after repetitive measurements and is also likely not due to different cell cycle phases. In contrast, Panagiotakopoulou et al. [47] reported periodic variations of cancer cell traction forces on substrates connected to proliferative cycle phases. Moreover, Lock et al. [48] even identified a specific form of adhesion complex which is assembled during the mitotic phase of cells. The dependency of our cell adhesion force results on cell cycle phase is challenging to analyze because it is difficult to determine the phase of cells which are attached to the AFM cantilever for measurements.

We want to mention that our single-cell force spectroscopy study is subject to similar technical limitations as reported by other research groups, see e.g., Helenius et al. [42]. Specifically, in our case, the adhesion forces exerted by the cells for contact times of more than 30 s were too high to be reliably and reproducibly measurable in our atomic force microscopy setup. Here, adhesion forces originating from contact times above 30 s usually exceeded the measurable range and the cell could not be completely detached from the substrate, which leads to our decision to limit the single-cell force spectroscopy measurements to contact time values up to 30 s. We attribute the increase in binding

strength to the beginning of specific binding site formations. Dot-like nascent adhesions and focal complexes form on time scales of tens of seconds before maturation into focal adhesions occurs, matching the time scales employed in our single-cell force spectroscopy measurements [2,49–53].

As recently shown by Chighizola et al. for SCFS measurements of PC12 cells, adhesion forces of these cells in contact with nanostructured colloidal ZrO_2 probes revealed a reduced number of adhesion sites after 60 s contact time [54]. This drop is considered to be caused by mechanotransductive interactions at the cellular level which result in excessive force loading in single adhesion sites. This process was not observed on the respective time scales when flat ZrO_2 probes were employed. In our experimentally accessible time scales, such force drop as a possible early marker of integrin adhesion complex maturation was not visible. However, since the size of focal adhesions depends on their maturation stage [55,56], we expect that for differently structured nanosurfaces with various length scales, time scales on which the observed actomyosin-generated forces occur might vary as well.

Due to the short time scale of our experiments, it is challenging to conclude which type of substrate material supports maturation of focal contact adhesions best, which is important for long-term cell behavior. In fact, interaction of cells and substrate materials can have a great variety of short-term, as well as long-term, consequences on cell behavior and functions, such as adhesion complex formation, spreading, proliferation, differentiation, gene expression, and mechanotransduction. Unraveling the connections between these diverse interactions remains challenging and even the definition of "good adhesion" can vary greatly for different cell types. In case of neurons, delicate cellular adhesion is not automatically a disadvantage [57,58]. Thus, in order to better understand adhesion of neurons and glial cells on the different electrode materials, we compared the single-cell force-spectroscopy data with long-term adhesion studies in order to investigate possible correlations between short-term adhesion and the spreading area of cells as an indicator of strong cell-surface interaction. To this end, we calculated the growth areas of cultured cells after one and three days on the four different materials. However, it is important to note that cellular organization and proliferation can strongly influence spreading: fast proliferation and the formation of cell clusters lead to a reduction of substrate space available for spreading.

As we have shown previously, U-87 MG cells showed the poorest cell proliferation on gold substrates (the cell number increased on gold by a factor of 1.6 and nearly tripled on ITO, TiN, and nanocolumnar TiN with additional growth time) [30]. Thus, the available space for spreading was largest on gold. However, the size of their cell bodies did not increase significantly. Hence, the adhesion behavior of glial cells hardly evolves on gold substrates over time. In contrast, U-87 MG cells proliferated much better on ITO, TiN, and nanocolumnar TiN substrates but still lacked a significant increase in cell size. The cells tended to form evenly distributed cell patterns instead of agglomerations and clusters on these materials [30] which would allow spreading in the empty intercellular spaces. However, we saw no significant changes in cell area, and thereby, cell adhesion for the glial cells. Overall, U-87 MG tended to behave the same on all utilized materials: cells arranged themselves in homogenous agglomeration-free patterns and hesitated to change their size independent of their proliferation behavior.

In contrast, neuronal SH-SY5Y cells exhibited a completely different response in contact with the electrode materials. We noticed an increase in cell size on gold and ITO, but the number of cells was halved on gold and stagnated on ITO after three days of growth time in comparison to the one-day experiment. The cells were distributed homogeneously and had enough space to spread (for an example of cell distribution on a surface see Figure S3, Supplementary Material). Additionally, optical inspection of cells revealed that cell networks lacked alterations: there were no new neurite formations, which in turn lead to only slight changes of the overall cell size since the central cell body hardly changed in size. We noticed only small variances of the cell size data of neuronal cells on TiN and TiN nano after one day. The cells had not yet formed clusters on the substrates and all cells had more or less the same amount of space available to them for spreading. The

situation changed after additional growth time when the number of SH-SY5Y cells had more than doubled, and the variance of cell sizes increased significantly. There were now giant and tiny cells that were only half as big as the mean cell size after one day. The cells started to agglomerate in clusters, whereas the cluster density was larger on TiN nano than TiN (for an example of cluster formation see Figure S4, Supplementary Material). This could very well give answers to the question of why there were overall fewer giant cells visible. Even if areas of very high densities are excluded from the results due to technical properties of the analysis algorithm which only allowed us to quantify cells we could fully see and distinguish from their immediate neighbors, the SH-SY5Y cells still grew densely and appeared therefore on average smaller than on TiN. There were areas in the vicinity of cell clusters and in the inter-cluster space of the samples where cells grew very large. This means that the cells produced long neurites and formed networks in the less-occupied substrate areas to connect with the cells in clusters. In summary, SH-SY5Y cells tended to spread more on TiN and nanocolumnar TiN in areas where there was enough empty space available in comparison to the ITO and gold materials. This suggests an increased adhesion of neuronal cells on TiN and TiN nano. Moreover, the cells formed more and longer neurites on these materials to build a network with cells in high-density areas in clusters (see Figure 4 and Supplementary Material). This behavior mirrors physiological conditions much better than a homogeneous cell distribution and weaker network formation of SH-SY5Y cells on ITO and gold.

We have to emphasize that during short-term adhesion, as present during single-cell force spectroscopy, unspecific bonds formed during cell-surface contact, while for longer culture times specific bonds, e.g., via integrin binding motifs, occurred [59]. Formation of such specific ligand-receptor pairs is also the origin of the observed neurite formation [60] mainly seen on TiN and TiN nano. Since TiN and TiN nano promote cell spreading to a much larger extent compared to gold and ITO (in fact the size of the cell body remained almost constant and it was the formation of new neurites which contributed to the growth area increase), we conclude that the maturation of specific bonds is directly correlated with cell size during long-term adhesion and a measure for the surfaces' bioactivity.

The effect of nanostructured surfaces on adhesion and proliferation of SH-SY5Y was recently reported by Boehler et al. [61]. They showed that nanostructured platinum coatings of neuroelectrodes, as well as unstructured surfaces, do not exhibit cytotoxic effects on the SH-SY5Y cells. Dominguez-Bajo et al. [62] grew neuronal cells derived from rats on both flat and nanostructured nickel and gold electrodes. Increased neural cell survival, improved neuronal differentiation, and fewer glial cells were measurable on nanostructured nickel in comparison to its flat counterpart. The surface topography of the gold samples seemed to have only little effect on cell proliferation and differentiation, while the nanostructure still reduced the number of glial cells in culture. Thus, apparently, the electrode material's surface chemistry, as well as topography, seems to play a major role in finding biocompatible candidates. In our experiments, we do not attribute differences in cell adhesion on Au and TiN substrates to surface roughness differences, since both materials exhibited a very similar RMS roughness and similar grain sizes [30]. Nevertheless, adhesion and spreading of neurons were different on these materials, most likely due to chemical influences.

In terms of tissue adhesion in contrast to single-cell adhesion, we want to point out that our previous study with neuronal tissues such as adult retinae and adult brain slices in contact with TiO_2 nanotube scaffolds clearly showed that the size of the nanotubes, viz. the length scale of the surface nanostructure, strongly influences tissue adhesion and cell viability [63,64]. From this study, we expect that the nanostructure of an electrode material might promote adhesion of neurons and even reduce the risk of glial scar formation and encapsulation, an important feature for the application of a neuroelectrode in vivo. Thus, even though the mechanical mismatch between brain tissue and electrode material cannot be avoided, the nanotopography of the electrode's surface might be a valuable tool to improve the connection between neurons and electrode. To this end, future studies should

address the interaction of neuronal tissue explants with nanocolumnar TiN to determine tissue adhesion ex vivo, while in vivo investigation of the material can give rise to the question if a nanostructure can reduce glial scarring.

Finally, we want to mention that the bioactivity of a material is often connected to the ability of protein adsorption, which in turn is important for cell adhesion. As we have shown previously, surface topography can change the adsorption behavior, and surfaces that promote fibronectin adsorption exhibit an enhanced ability for improved cell adhesion and spreading [39,65]. To investigate possible differences in protein adsorption behavior, we soaked our Au, ITO, TiN, and TiN nano materials in purified water including fluorescently labeled laminin, an extracellular matrix protein, which is widely expressed in the central nervous system and important for specific binding of the ECM to neurons (see Figure S5, Supplementary Material). In fact, we observed only very small differences in laminin adsorption. Thus, we conclude that the observed cell behavior in terms of short-term adhesion and spreading after 1 to 3 days is hardly influenced by possible protein adsorption, but determined by other material properties such as chemical cues.

4. Materials and Methods

4.1. Electrode Materials Preparation

The following substrates were used for our experiments: indium tin oxide (ITO), gold (Au), as well as titanium nitride in two different surface topographies (TiN and TiN nano). All materials were produced by thin film deposition on glass cover slits and characterized in terms of surface topography by electron microscopy and atomic force microscopy as described previously in Abend et al. [30]. Briefly, the different films exhibit the following features: the gold substrates showed the lowest root-mean-square (RMS) roughness and even transitions between the individual grains. In contrast, ITO exhibited the highest RMS roughness of all four materials and a crystalline surface structure. TiN samples were produced with two different sputter times which lead to a film thickness of 150–200 nm for TiN and 500–550 nm for TiN nano and widely different surface morphologies. TiN showed a cauliflower-like formation with several grain sizes, whereas TiN nano exhibited a nanocolumnar structure with single-type grains. This resulted in a surface area increase of (1.27 ± 0.08) nm for TiN nano. All of the other materials scored below 1.1 with (1.02 ± 0.01) nm for Au, (1.10 ± 0.02) nm for ITO, and (1.07 ± 0.01) nm for TiN (for more details see Abend et al. [30]).

4.2. Cell Lines and Cell Culture for Single-Cell Force Spectroscopy

We used the glioblastoma cell line U-87 MG (Cat.No. 300367, CLS Cell Lines Service GmbH, Eppelheim, Germany) and the neuroblastoma cell line SH-SY5Y (Cat.No. CRL-2266, ATCC LGC Standards GmbH, Wesel, Germany) for our studies. Both cell lines were grown in culture flasks in a 1:1 mixture of MEM Eagle/Ham's F12 medium with Earle's salts, L-glutamine, and sodium bicarbonate (Cat.No. M4655 and N6658, Sigma-Aldrich Chemie GmbH, Munich, Germany) and kept at 37 °C in a 95% air and 5% CO_2 atmosphere. Medium change was performed every 2–3 days. We supplemented the cell culture medium with 10% fetal bovine serum (Cat.No. S0615, Biochrom GmbH, Berlin, Germany) and 1% penicillin/streptomycin (Cat.No. P0781, Sigma-Aldrich Chemie GmbH, Munich, Germany). Cells were passaged using phosphate-buffered saline (PBS, Cat.No. 18912014, Gibco, Thermo Fisher Scientific, Waltham, MA, USA) with 0.025% (*w/v*) trypsin and 0.011% (*w/v*) ethylenediaminetetraacetic acid (EDTA, Cat.No. L2143, Biochrom GmbH, Berlin, Germany). Trypsinization took 3–4 min for each culture flask.

For normal cell passages, regular serum-containing cell culture medium was added to the detached cells to inactivate the trypsin, and cells were seeded in fresh complete medium afterward. To perform single-cell force spectroscopy experiments with the detached cells, serum-free medium consisting of a 1:1 mixture of MEM Eagle/Ham's F12 medium containing Earle's salts, L-glutamine, and sodium bicarbonate (Cat.No. M4655 and N6658, Sigma-Aldrich Chemie GmbH, Munich, Germany) supplemented with 1%

penicillin/streptomycin (Cat.No. P0781, Sigma-Aldrich Chemie GmbH, Munich, Germany) was added to the detached cells. Cells were then centrifuged for 1 min at 800 rounds/min. The resulting supernatant liquid was aspirated and the cell pellet was resuspended in fresh serum-free cell culture medium.

4.3. Single-Cell Force Spectroscopy

We quantified adhesion of glial cells (U-87 MG) and undifferentiated neuron-like cells (SH-SY5Y) on electrode materials (Au, ITO, TiN, and TiN nano) by single-cell force spectroscopy. Prior to measurement, we attached a single cell to a tipless arrow-shaped cantilever (Arrow™ TL1, NanoWorld AG, Neuchâtel, Switzerland) utilizing a Poly-D-Lysine coating (PDL, Cat.No. A-003-M, Sigma-Aldrich Chemie GmbH, Munich, Germany). PDL was diluted with sterile PBS to a concentration of 20 µg/mL and each cantilever was coated with 50 µL of that solution in a petri dish overnight at 4 °C. Each cantilever was used once and cleaned after a measurement with one cell using piranha etch solution consisting of 70% sulfuric acid (Cat.No. 84727, Sigma-Aldrich Chemie GmbH, Munich, Germany) and 30% hydrogen peroxide (Cat.No. H1009, Sigma-Aldrich Chemie GmbH, Munich, Germany).

For single-cell force spectroscopy, the CellHesion atomic force microscope (CellHesion 200, JPK BioAFM–Bruker Nano GmbH, Berlin, Germany) equipped with the JPK Instruments SPM and DP software Version 6.1.146 was used for the cell adhesion experiments. A CCD camera (FireWire CCD Color Camera DFK 41AF02, The Imaging Source Europe GmbH, Bremen, Germany) was mounted onto the CellHesion system to visualize cell capture and adhesion to the cantilever. For our experiments, we used standard 4 cm petri dishes (TPP Techno Plastic Products AG, Trasadingen, Switzerland) coated with a solution of 1% bovine serum albumin (BSA, Cat.No. A2153, Sigma-Aldrich Chemie GmbH, Munich, Germany) diluted in PBS. The dishes were stored at 4 °C overnight, shortly rinsed with Millipore water, and dried with nitrogen the next day. An electrode substrate was glued to the petri dish bottom using nail polish to avoid slippage. Once the polish had dried completely, 2 mL serum-free cell culture medium was added and the dish heating system was set to 37 °C. Additionally, an atmosphere consisting of 95% air and 5% CO_2 was created. A PDL-coated cantilever was then mounted on the glass block of the CellHesion-AFM. After reaching thermal equilibrium in the 37 °C warm serum-free culture medium, the cantilever was then calibrated with the built-in contact-based calibration tool of the JPK software, which is based on the spring constant calibration method proposed by Hutter and Bechhoefer [66]. Cells were passaged as described in the section above. The scanning head of the CellHesion-AFM was briefly removed to flush 10 µL of the cell solution into the petri dish. One cell of average size and smooth spherical form was chosen for the measurement. It was captured by positioning the tip of the cantilever over the cell and running a single scan repetition in the constant force mode with a 500 pN setpoint, 5 µm/s constant speed, 5 s contact time and 100 µm pulling length. Once the cell was successfully captured, we waited 30 min before starting the measurements to ensure that the cell firmly adhered to the cantilever. The cantilever was then positioned over the electrode substrate in the petri dish and the cell adhesion behavior on the material was probed by acquiring force-distance curves with 500 pN setpoint and 100 µm pulling length. The extend speed was set to 2 µm/s and retract speed was chosen as 1 µm/s for each scan repetition. Contact time was set to either 5 s or 30 s. The cell was probed 5 times with an adhesion time of 5 s with 120 s recovery breaks in between repetitions. After a 5 min rest time, the cell was probed again 5 times with a contact time of 30 s and 120 s recovery breaks in between, respectively. The position of the cell on the electrode substrate was changed after every run. Having finished the measurements with one cell, the cell culture medium in the petri dish was replaced with fresh serum-free medium. The cantilever was replaced by a new one with a different cell attached to repeat the entire experimental procedure.

4.4. Growth Area of Cells

The growth area of both U-87 MG and differentiated SH-SY5Y cells on electrode materials (Au, ITO, TiN, and TiN nano) was determined using fluorescence microscopy. We employed the following protocol as previously described [30]. Briefly, for this experiment, we seeded the cells at a density of 130 cells/mm^2 onto electrode substrate materials (Au, ITO, TiN, TiN nano). Accurate cell numbers were obtained using an automatic optical cell counter (EVETM, NanoEntek Inc., Seoul, Korea). The U-87 MG cells were fixed with paraformaldehyde (Cat.No. HT5011, Sigma-Aldrich Chemie GmbH, Munich, Germany) for 15 min. at time points of 24 h or 72 h after seeding. We did not utilize longer culture times because usually cells then start to grow into dense layers which hinders the cell area analysis. After fixation, cells were washed with PBS and treated with 1% (*w/v*) Triton X-100 (Cat.No. 9002-93-1, Sigma-Aldrich Chemie GmbH, Munich, Germany) and 0.5% (*w/v*) bovine serum albumin (Cat.No. A2153, Sigma-Aldrich Chemie GmbH, Munich, Germany) for 10 min at room temperature as preparation for fluorescent labeling of actin fibers and cell nuclei. To this end, 1 µg/mL Hoechst 34580 (Cat.No. H21486, Molecular Probes, Eugene, OR, USA) and 0.44 µM Alexa Fluor 532 Phalloidin (Cat.No. A-22282, Molecular Probes, Eugene, OR, USA) diluted in PBS was added to the cells at room temperature for 15 min. Cells were washed again with PBS and placed upside down in petri dishes (Cat.No. 80136, ibidi GmbH, Gräfeling, Germany). We applied mounting medium (Cat.No. 50001, ibidi GmbH, Gräfeling, Germany) between the sample and the petri dish. Specimens were stored at 4 °C before imaging.

Treatment of samples with SH-SY5Y instead of U-87 MG cells was slightly different: we added 25 nM staurosporine (STS, Cat.No. S5921, Sigma-Aldrich Chemie GmbH, Munich, Germany) to the SH-SY5Y samples 24 h after seeding to initiate the cell differentiation process, which takes 72 h to complete [59]. Half of the SH-SY5Y specimens were fixed directly upon removing the STS. For the remaining samples, we replaced the STS containing medium with regular growth medium and let the cells grow for another 72 h before fixation. Subsequently, cells were fluorescently labeled as reported before. The cell network morphology was imaged using confocal laser scanning microscopy. We employed an inverted Zeiss Axio Observer.Z1 microscope equipped with a spinning disk unit (Yokogawa CSU-X1A 5000, Tokyo, Japan) for image acquisition. An array of dual-channel images of whole cell networks was taken with a 25 × glycerin immersion objective for each sample. Each file enclosed a substrate area of 0.22 cm^2. Up to 54 individual images were required to cover the complete sample area.

The images of actin fibers were used to determine the cell growth area. We processed them with a Fiji distribution [67] (Windows 10, 64-bit version) based on ImageJ software [39,68]. Images were thresholded, binarized, and subsequently analyzed with the edge detection of the particle tracker tool to detect cell shapes and determine the size of the cells. The images of cell nuclei were processed similarly and used for cell counting. Results of the cell proliferation analysis can be found in our previous publication [30].

4.5. Statistical Analysis

We employed CellHesion single-cell force spectroscopy measurements to determine the adhesion force of 15 cells for each of the 4 substrate types and 2 adhesion times (5 s and 30 s). For each cell, 10 force-distance curves were acquired, i.e., 5 recordings for each of the adhesion times. Overall, 120 cells were used for the single-cell spectroscopy experiments which resulted in the acquisition of 1200 force-distance curves. The JPK Data Processing software (JPK Data Processing Version 6.1.169, JPK BioAFM–Bruker Nano GmbH, Berlin, Germany) was used to extract the maximum adhesion force and the work required to completely detach a single cell from the electrode substrate of each force-distance curve.

We repeated the cell area measurements three times for each cell type and material combination. In total, we analyzed 160,000 cells.

Two-sample *t*-test in OriginLab software (OriginPro 2017G, OriginLab Corporation, Northampton, MA, USA) for unequal sample sizes was employed to analyze statistical

significance of data sets. We marked data values as significant (*) for $p \leq 0.05$ and highly significant (**) for $p \leq 0.01$.

5. Conclusions

Many biomedical applications such as neuroelectrodes, for example, rely on fine-tuned coupling of cells and tissue to the electrode's surface. Thus, cell survival, proliferation, and biochemical function all depend on the electrode materials' surface chemistry and topography. We investigated the short-term adhesion dynamics and long-term evolution of cell spreading and neurite formation with culture time of human neuron-like SH-SY5Y and glial-like U-87 MG cells on four different electrode materials (TiN, TiN nano, ITO, and gold). We found the adhesion behavior of U-87 MG cells to be mostly independent of the substrate material and we found cells stopped spreading after one day of culture time. In contrast, neuronal cells spread much better on TiN and nanocolumnar TiN in comparison with ITO and gold. Here, spreading was mainly determined by the formation of long and numerous neurites for longer culture times. The lowered self-impedance of nanocolumnar TiN combined with our findings of the cells' adhesion and spreading makes the material a promising candidate for building miniaturized microelectrodes. Even though our material might induce the formation of glial scars due to the mechanical mismatch of the material and the brain tissue, novel treatments are under consideration to restore local neuron density and improve the long-term recording stability as recently shown by Zhang et al. [69]. Moreover, Shur et al. recently demonstrated that soft printable coatings improve the mechanical properties on the electrode surface towards more physiologic conditions important to reduce the formation of scar tissue [70]. Thus, surface structures that promote coupling to neurons, as seen in our study, offer great perspectives for brain-machine interfaces, ranging from MEA to deep brain stimulation. Future studies should address the interplay of neurons and glial cells on nanocolumnar TiN, e.g., in a co-culture system of primary cells or even in an in vivo system to further develop our nanostructured TiN towards possible biomedical applications. Here coatings with suitable electric properties might be a valuable option to enhance neuron adhesion important for long-term recording in vivo.

References

1. Khalili, A.; Ahmad, M. A Review of Cell Adhesion Studies for Biomedical and Biological Applications. *Int. J. Mol. Sci.* **2015**, *16*, 18149–18184. [CrossRef]
2. Zaidel-Bar, R.; Cohen, M.; Addadi, L.; Geiger, B. Hierarchical assembly of cell–matrix adhesion complexes. *Biochem. Soc. Trans.* **2004**, *32*, 416–420. [CrossRef] [PubMed]
3. Hynes, R.O. Integrins: Versatility, modulation, and signaling in cell adhesion. *Cell* **1992**, *69*, 11–25. [CrossRef]
4. Qi, C.; Lin, J.; Fu, L.-H.; Huang, P. Calcium-based biomaterials for diagnosis, treatment, and theranostics. *Chem. Soc. Rev.* **2018**, *47*, 357–403. [CrossRef]
5. Pérez-González, F.; Sánchez-Labrador, L.; Molinero-Mourelle, P.; Sáez-Alcaide, L.M.; Cortés-Bretón-Brinkmann, J.; García-Denche, J.T.; López-Quiles, J.; Martinez-González, J.M. Dental implant placement through impacted teeth or residual roots as an alternative to invasive extraction surgeries: A systematic literature review. *Br. J. Oral Maxillofac. Surg.* **2021**. [CrossRef]
6. Grzeskowiak, R.M.; Schumacher, J.; Dhar, M.S.; Harper, D.P.; Mulon, P.-Y.; Anderson, D.E. Bone and Cartilage Interfaces With Orthopedic Implants: A Literature Review. *Front. Surg.* **2020**, *7*, 1–15. [CrossRef]
7. Malchesky, P.S. Artificial Organs 2019: A year in review. *Artif. Organs* **2020**, *44*, 314–338. [CrossRef]
8. Ramos, T.; Moroni, L. Tissue Engineering and Regenerative Medicine 2019: The Role of Biofabrication—A Year in Review. *Tissue Eng. Part C Methods* **2020**, *26*, 91–106. [CrossRef] [PubMed]
9. Lam, M.T.; Wu, J.C. Biomaterial applications in cardiovascular tissue repair and regeneration. *Expert Rev. Cardiovasc. Ther.* **2012**, *10*, 1039–1049. [CrossRef]
10. Mehta, P.; Haj-Ahmad, R.; Rasekh, M.; Arshad, M.S.; Smith, A.; van der Merwe, S.M.; Li, X.; Chang, M.-W.; Ahmad, Z. Pharmaceutical and biomaterial engineering via electrohydrodynamic atomization technologies. *Drug Discov. Today* **2017**, *22*, 157–165. [CrossRef]
11. Fang, J.Y.; Tolleson, C. The role of deep brain stimulation in Parkinson's disease: An overview and update on new developments. *Neuropsychiatr. Dis. Treat.* **2017**, *13*, 723–732. [CrossRef]
12. Mayberg, H.S.; Lozano, A.M.; Voon, V.; McNeely, H.E.; Seminowicz, D.; Hamani, C.; Schwalb, J.M.; Kennedy, S.H. Deep Brain Stimulation for Treatment-Resistant Depression. *Neuron* **2005**, *45*, 651–660. [CrossRef] [PubMed]
13. Guido, K.; Clavijo, A.; Zhu, K.; Ding, X.; Ma, K. Strategies to Improve Neural Electrode Performance. In *Neural Interface Engineering*; Springer International Publishing: Cham, Switzerland, 2020; pp. 173–199.
14. Renz, A.F.; Reichmuth, A.M.; Stauffer, F.; Thompson-Steckel, G.; Vörös, J. A guide towards long-term functional electrodes interfacing neuronal tissue. *J. Neural Eng.* **2018**, *15*, 061001. [CrossRef] [PubMed]
15. Moeendarbary, E.; Weber, I.P.; Sheridan, G.K.; Koser, D.E.; Soleman, S.; Haenzi, B.; Bradbury, E.J.; Fawcett, J.; Franze, K. The soft mechanical signature of glial scars in the central nervous system. *Nat. Commun.* **2017**, *8*, 14787. [CrossRef] [PubMed]
16. Song, E.; Li, J.; Won, S.M.; Bai, W.; Rogers, J.A. Materials for flexible bioelectronic systems as chronic neural interfaces. *Nat. Mater.* **2020**, *19*, 590–603. [CrossRef] [PubMed]
17. Shi, Y.; Liu, R.; He, L.; Feng, H.; Li, Y.; Li, Z. Recent development of implantable and flexible nerve electrodes. *Smart Mater. Med.* **2020**, *1*, 131–147. [CrossRef]
18. Woods, G.A.; Rommelfanger, N.J.; Hong, G. Bioinspired Materials for In Vivo Bioelectronic Neural Interfaces. *Matter* **2020**, *3*, 1087–1113. [CrossRef]
19. Li, H.; Wang, J.; Fang, Y. Bioinspired flexible electronics for seamless neural interfacing and chronic recording. *Nanoscale Adv.* **2020**, *2*, 3095–3102. [CrossRef]
20. Zhang, S.; Wang, C.; Linghu, C.; Wang, S.; Song, J. Mechanics Strategies for Implantation of Flexible Neural Probes. *J. Appl. Mech.* **2021**, *88*, 010801. [CrossRef]
21. Bareket-Keren, L.; Hanein, Y. Carbon nanotube-based multi electrode arrays for neuronal interfacing: Progress and prospects. *Front. Neural Circuits* **2013**, *6*, 1–16. [CrossRef] [PubMed]
22. Liu, S.; Zhao, Y.; Hao, W.; Zhang, X.-D.; Ming, D. Micro- and nanotechnology for neural electrode-tissue interfaces. *Biosens. Bioelectron.* **2020**, *170*, 112645. [CrossRef]
23. Spira, M.E.; Hai, A. Multi-electrode array technologies for neuroscience and cardiology. *Nat. Nanotechnol.* **2013**, *8*, 83–94. [CrossRef]
24. Vafaiee, M.; Mohammadpour, R.; Vossoughi, M.; Asadian, E.; Janahmadi, M.; Sasanpour, P. Carbon Nanotube Modified Microelectrode Array for Neural Interface. *Front. Bioeng. Biotechnol.* **2021**, *8*, 1–12. [CrossRef]
25. Jahnke, H.-G.; Krinke, D.; Seidel, D.; Lilienthal, K.; Schmidt, S.; Azendorf, R.; Fischer, M.; Mack, T.; Striggow, F.; Althaus, H.; et al. A novel 384-multiwell microelectrode array for the impedimetric monitoring of Tau protein induced neurodegenerative processes. *Biosens. Bioelectron.* **2017**, *88*, 78–84. [CrossRef] [PubMed]
26. Sánchez, G.; Dalchiele, E.; Bologna Alles, A. Electrical characterization of titanium nitride surfaces for pacing electrodes. *J. Mater. Sci.* **2006**, *41*, 3241–3247. [CrossRef]
27. Krinke, D.; Jahnke, H.-G.; Pänke, O.; Robitzki, A.A. A microelectrode-based sensor for label-free in vitro detection of ischemic effects on cardiomyocytes. *Biosens. Bioelectron.* **2009**, *24*, 2798–2803. [CrossRef]
28. Suni, I.I. Impedance methods for electrochemical sensors using nanomaterials. *TrAC Trends Anal. Chem.* **2008**, *27*, 604–611. [CrossRef]

29. Cui, X.; Martin, D.C. Fuzzy gold electrodes for lowering impedance and improving adhesion with electrodeposited conducting polymer films. *Sens. Actuators A Phys.* **2003**, *103*, 384–394. [CrossRef]

30. Abend, A.; Steele, C.; Schmidt, S.; Frank, R.; Jahnke, H.; Zink, M. Proliferation and Cluster Analysis of Neurons and Glial Cell Organization on Nanocolumnar TiN Substrates. *Int. J. Mol. Sci.* **2020**, *21*, 6249. [CrossRef]

31. Caponi, S.; Mattana, S.; Ricci, M.; Sagini, K.; Juarez-Hernandez, L.J.; Jimenez-Garduño, A.M.; Cornella, N.; Pasquardini, L.; Urbanelli, L.; Sassi, P.; et al. A multidisciplinary approach to study the functional properties of neuron-like cell models constituting a living bio-hybrid system: SH-SY5Y cells adhering to PANI substrate. *AIP Adv.* **2016**, *6*, 111303. [CrossRef]

32. Cellot, G.; Lagonegro, P.; Tarabella, G.; Scaini, D.; Fabbri, F.; Iannotta, S.; Prato, M.; Salviati, G.; Ballerini, L. PEDOT:PSS Interfaces Support the Development of Neuronal Synaptic Networks with Reduced Neuroglia Response In vitro. *Front. Neurosci.* **2016**, *9*, 1–11. [CrossRef] [PubMed]

33. Juarez-Hernandez, L.J.; Cornella, N.; Pasquardini, L.; Battistoni, S.; Vidalino, L.; Vanzetti, L.; Caponi, S.; Serra, M.D.; Iannotta, S.; Pederzolli, C.; et al. Bio-hybrid interfaces to study neuromorphic functionalities: New multidisciplinary evidences of cell viability on poly(anyline) (PANI), a semiconductor polymer with memristive properties. *Biophys. Chem.* **2016**, *208*, 40–47. [CrossRef]

34. Juzekaeva, E.; Nasretdinov, A.; Battistoni, S.; Berzina, T.; Iannotta, S.; Khazipov, R.; Erokhin, V.; Mukhtarov, M. Coupling Cortical Neurons through Electronic Memristive Synapse. *Adv. Mater. Technol.* **2019**, *4*, 1800350. [CrossRef]

35. Roncador, A.; Jimenez-Garduño, A.M.; Pasquardini, L.; Giusti, G.; Cornella, N.; Lunelli, L.; Potrich, C.; Bartali, R.; Aversa, L.; Verucchi, R.; et al. Primary cortical neurons on PMCS TiO2 films towards bio-hybrid memristive device: A morpho-functional study. *Biophys. Chem.* **2017**, *229*, 115–122. [CrossRef] [PubMed]

36. Roach, P.; Parker, T.; Gadegaard, N.; Alexander, M.R. Surface strategies for control of neuronal cell adhesion: A review. *Surf. Sci. Rep.* **2010**, *65*, 145–173. [CrossRef]

37. Harjumäki, R.; Zhang, X.; Nugroho, R.W.N.; Farooq, M.; Lou, Y.-R.; Yliperttula, M.; Valle-Delgado, J.J.; Österberg, M. AFM Force Spectroscopy Reveals the Role of Integrins and Their Activation in Cell–Biomaterial Interactions. *ACS Appl. Bio Mater.* **2020**, *3*, 1406–1417. [CrossRef]

38. Zink, M.; Szillat, F.; Allenstein, U.; Mayr, S.G. Interaction of Ferromagnetic Shape Memory Alloys and RGD Peptides for Mechanical Coupling to Cells: From Ab Initio Calculations to Cell Studies. *Adv. Funct. Mater.* **2013**, *23*, 1383–1391. [CrossRef]

39. Weidt, A.; Mayr, S.G.; Zink, M. Influence of Topological Cues on Fibronectin Adsorption and Contact Guidance of Fibroblasts on Microgrooved Titanium. *ACS Appl. Bio Mater.* **2019**, *2*, 1066–1077. [CrossRef]

40. Frisch, T.; Thoumine, O. Predicting the kinetics of cell spreading. *J. Biomech.* **2002**, *35*, 1137–1141. [CrossRef]

41. Shinde, A.; Illath, K.; Gupta, P.; Shinde, P.; Lim, K.-T.; Nagai, M.; Santra, T.S. A Review of Single-Cell Adhesion Force Kinetics and Applications. *Cells* **2021**, *10*, 577. [CrossRef]

42. Helenius, J.; Heisenberg, C.-P.; Gaub, H.E.; Muller, D.J. Single-cell force spectroscopy. *J. Cell Sci.* **2008**, *121*, 1785–1791. [CrossRef] [PubMed]

43. Baek, J.; Cho, S.-Y.; Kang, H.; Ahn, H.; Jung, W.-B.; Cho, Y.; Lee, E.; Cho, S.-W.; Jung, H.-T.; Im, S.G. Distinct Mechanosensing of Human Neural Stem Cells on Extremely Limited Anisotropic Cellular Contact. *ACS Appl. Mater. Interfaces* **2018**, *10*, 33891–33900. [CrossRef]

44. Chen, W.; Han, S.; Qian, W.; Weng, S.; Yang, H.; Sun, Y.; Villa-Diaz, L.G.; Krebsbach, P.H.; Fu, J. Nanotopography regulates motor neuron differentiation of human pluripotent stem cells. *Nanoscale* **2018**, *10*, 3556–3565. [CrossRef]

45. Schulte, C.; Rodighiero, S.; Cappelluti, M.A.; Puricelli, L.; Maffioli, E.; Borghi, F.; Negri, A.; Sogne, E.; Galluzzi, M.; Piazzoni, C.; et al. Conversion of nanoscale topographical information of cluster-assembled zirconia surfaces into mechanotransductive events promotes neuronal differentiation. *J. Nanobiotechnol.* **2016**, *14*, 18. [CrossRef]

46. Dao, L.; Weiland, U.; Hauser, M.; Nazarenko, I.; Kalt, H.; Bastmeyer, M.; Franz, C.M. Revealing non-genetic adhesive variations in clonal populations by comparative single-cell force spectroscopy. *Exp. Cell Res.* **2012**, *318*, 2155–2167. [CrossRef]

47. Panagiotakopoulou, M.; Lendenmann, T.; Pramotton, F.M.; Giampietro, C.; Stefopoulos, G.; Poulikakos, D.; Ferrari, A. Cell cycle–dependent force transmission in cancer cells. *Mol. Biol. Cell* **2018**, *29*, 2528–2539. [CrossRef] [PubMed]

48. Lock, J.G.; Jones, M.C.; Askari, J.A.; Gong, X.; Oddone, A.; Olofsson, H.; Göransson, S.; Lakadamyali, M.; Humphries, M.J.; Strömblad, S. Reticular adhesions are a distinct class of cell-matrix adhesions that mediate attachment during mitosis. *Nat. Cell Biol.* **2018**, *20*, 1290–1302. [CrossRef]

49. Zimmerman, E.; Geiger, B.; Addadi, L. Initial Stages of Cell-Matrix Adhesion Can Be Mediated and Modulated by Cell-Surface Hyaluronan. *Biophys. J.* **2002**, *82*, 1848–1857. [CrossRef]

50. Geiger, B.; Yamada, K.M. Molecular Architecture and Function of Matrix Adhesions. *Cold Spring Harb. Perspect. Biol.* **2011**, *3*, a005033. [CrossRef]

51. Geiger, B.; Spatz, J.P.; Bershadsky, A.D. Environmental sensing through focal adhesions. *Nat. Rev. Mol. Cell Biol.* **2009**, *10*, 21–33. [CrossRef]

52. Parsons, J.T.; Horwitz, A.R.; Schwartz, M.A. Cell adhesion: Integrating cytoskeletal dynamics and cellular tension. *Nat. Rev. Mol. Cell Biol.* **2010**, *11*, 633–643. [CrossRef]

53. Cakir, M.V.; Allenstein, U.; Zink, M.; Mayr, S.G. Early adhesion of cells to ferromagnetic shape memory alloys functionalized with plasma assembled biomolecules—A single cell force spectroscopy study. *Mater. Des.* **2018**, *158*, 19–27. [CrossRef]

54. Chighizola, M.; Previdi, A.; Dini, T.; Piazzoni, C.; Lenardi, C.; Milani, P.; Schulte, C.; Podestà, A. Adhesion force spectroscopy with nanostructured colloidal probes reveals nanotopography-dependent early mechanotransductive interactions at the cell membrane level. *Nanoscale* **2020**, *12*, 14708–14723. [CrossRef] [PubMed]

55. Lamers, E.; van Horssen, R.; Riet, J.; van Delft, F.; Luttge, R.; Walboomers, X.; Jansen, J. The influence of nanoscale topographical cues on initial osteoblast morphology and migration. *Eur. Cells Mater.* **2010**, *20*, 329–343. [CrossRef] [PubMed]

56. Owen, G.R.; Meredith, D.O.; Ap Gwynn, I.; Richards, R. Focal adhesion quantification—A new assay of material biocompatibility?: Review. *Eur. Cells Mater.* **2005**, *9*, 85–96. [CrossRef] [PubMed]

57. Betz, T.; Koch, D.; Lu, Y.-B.; Franze, K.; Kas, J.A. Growth cones as soft and weak force generators. *Proc. Natl. Acad. Sci. USA* **2011**, *108*, 13420–13425. [CrossRef]

58. Kerstein, P.C.; Nichol, R.H., IV; Gomez, T.M. Mechanochemical regulation of growth cone motility. *Front. Cell. Neurosci.* **2015**, *9*, 1–16. [CrossRef]

59. Powell, S.K.; Kleinman, H.K. Neuronal laminins and their cellular receptors. *Int. J. Biochem. Cell Biol.* **1997**, *29*, 401–414. [CrossRef]

60. Kleinman, H.K.; Ogle, R.C.; Cannon, F.B.; Little, C.D.; Sweeney, T.M.; Luckenbill-Edds, L. Laminin receptors for neurite formation. *Proc. Natl. Acad. Sci. USA* **1988**, *85*, 1282–1286. [CrossRef]

61. Boehler, C.; Vieira, D.M.; Egert, U.; Asplund, M. NanoPt—A Nanostructured Electrode Coating for Neural Recording and Microstimulation. *ACS Appl. Mater. Interfaces* **2020**, *12*, 14855–14865. [CrossRef]

62. Domínguez-Bajo, A.; Rodilla, B.L.; Calaresu, I.; Arché-Núñez, A.; González-Mayorga, A.; Scaini, D.; Pérez, L.; Camarero, J.; Miranda, R.; López-Dolado, E.; et al. Interfacing Neurons with Nanostructured Electrodes Modulates Synaptic Circuit Features. *Adv. Biosyst.* **2020**, *4*, 2000117. [CrossRef]

63. Dallacasagrande, V.; Zink, M.; Huth, S.; Jakob, A.; Müller, M.; Reichenbach, A.; Käs, J.A.; Mayr, S.G. Tailoring Substrates for Long-Term Organotypic Culture of Adult Neuronal Tissue. *Adv. Mater.* **2012**, *24*, 2399–2403. [CrossRef] [PubMed]

64. Kallendrusch, S.; Merz, F.; Bechmann, I.; Mayr, S.G.; Zink, M. Long-Term Tissue Culture of Adult Brain and Spleen Slices on Nanostructured Scaffolds. *Adv. Healthc. Mater.* **2017**, *6*, 2192–2640. [CrossRef]

65. De Luca, A.C.; Zink, M.; Weidt, A.; Mayr, S.G.; Markaki, A.E. Effect of microgrooved surface topography on osteoblast maturation and protein adsorption. *J. Biomed. Mater. Res. Part A* **2015**, *103*, 2689–2700. [CrossRef] [PubMed]

66. Hutter, J.L.; Bechhoefer, J. Calibration of atomic-force microscope tips. *Rev. Sci. Instrum.* **1993**, *64*, 1868–1873. [CrossRef]

67. Schindelin, J.; Arganda-Carreras, I.; Frise, E.; Kaynig, V.; Longair, M.; Pietzsch, T.; Preibisch, S.; Rueden, C.; Saalfeld, S.; Schmid, B.; et al. Fiji: An open-source platform for biological-image analysis. *Nat. Methods* **2012**, *9*, 676–682. [CrossRef]

68. Schindelin, J.; Rueden, C.T.; Hiner, M.C.; Eliceiri, K.W. The ImageJ ecosystem: An open platform for biomedical image analysis. *Mol. Reprod. Dev.* **2015**, *82*, 518–529. [CrossRef]

69. Zhang, Z.; Li, Q.; Han, L.; Zhong, Y. Layer-by-layer films assembled from natural polymers for sustained release of neurotrophin. *Biomed. Mater.* **2015**, *10*, 055006. [CrossRef]

70. Shur, M.; Fallegger, F.; Pirondini, E.; Roux, A.; Bichat, A.; Barraud, Q.; Courtine, G.; Lacour, S.P. Soft Printable Electrode Coating for Neural Interfaces. *ACS Appl. Bio Mater.* **2020**, *3*, 4388–4397. [CrossRef]

Adhesion of neurons and glial cells with nanocolumnar TiN films for brain-machine interfaces
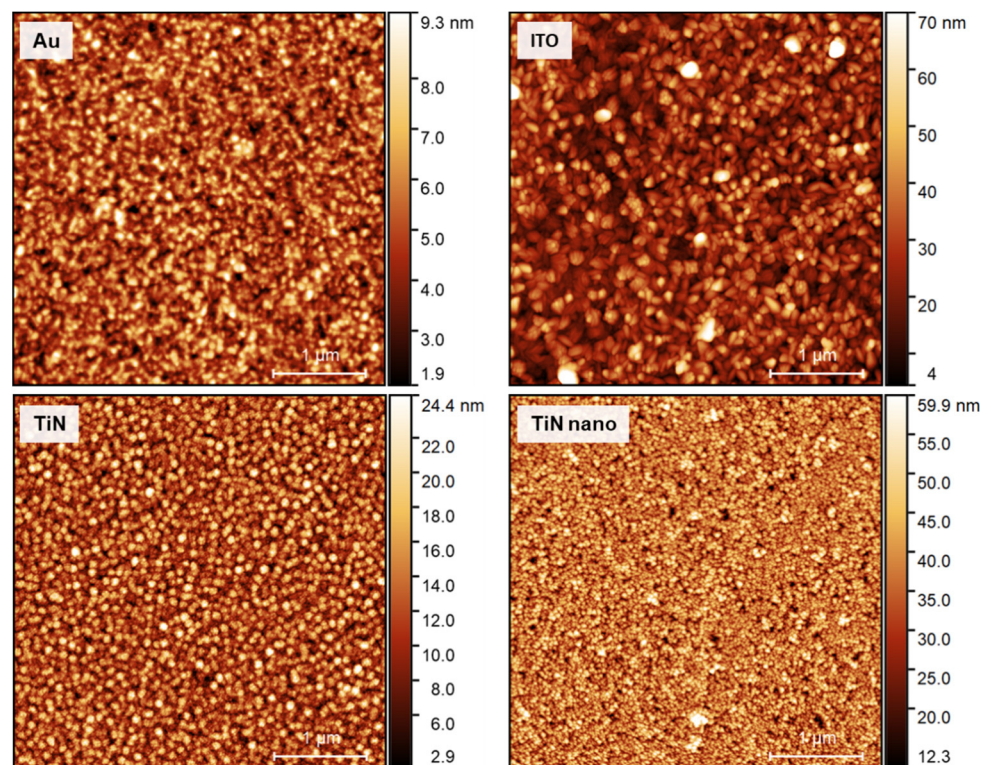
Figure S1. Atomic force microscopy-based topology characterization. The electrode materials of gold (Au), indium tin oxide (ITO), titanium nitride (TiN), and titanium nitride with nanocolumnar structure (TiN nano) were imaged with a JPK NanoWizard 3 atomic force microscope in direct drive AC mode with a TESPAHAR cantilever (Bruker).
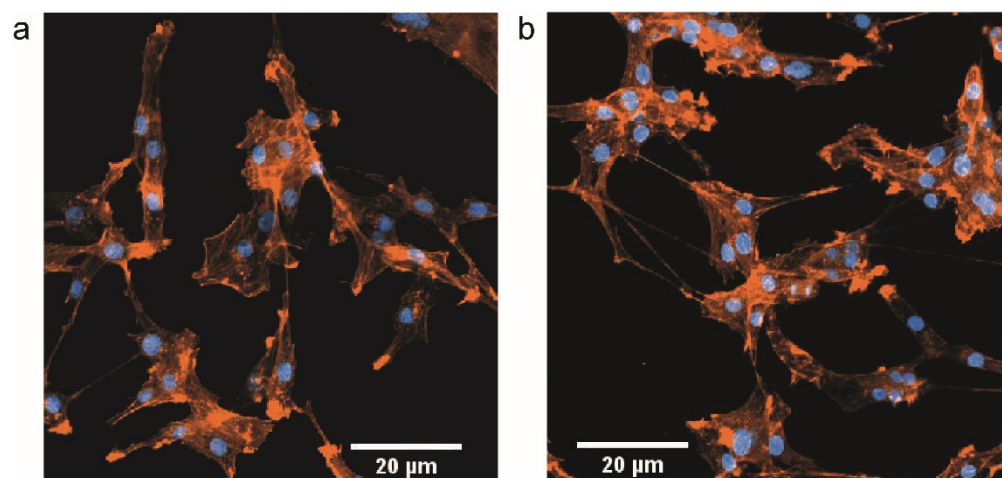
Figure S2. (a) Fluorescence image of U-87 MG cells grown on ITO substrate for 3 days. Actin fibers are shown in orange and cell nuclei in blue; **(b)** Same as in **(a)** for cells cultured on nanocolumnar TiN.

Figure S3. Fluorescent image of SH-SY5Y cells grown on ITO substrate for 3 days after differentiation. Actin fibers are shown in orange and cell nuclei in blue.

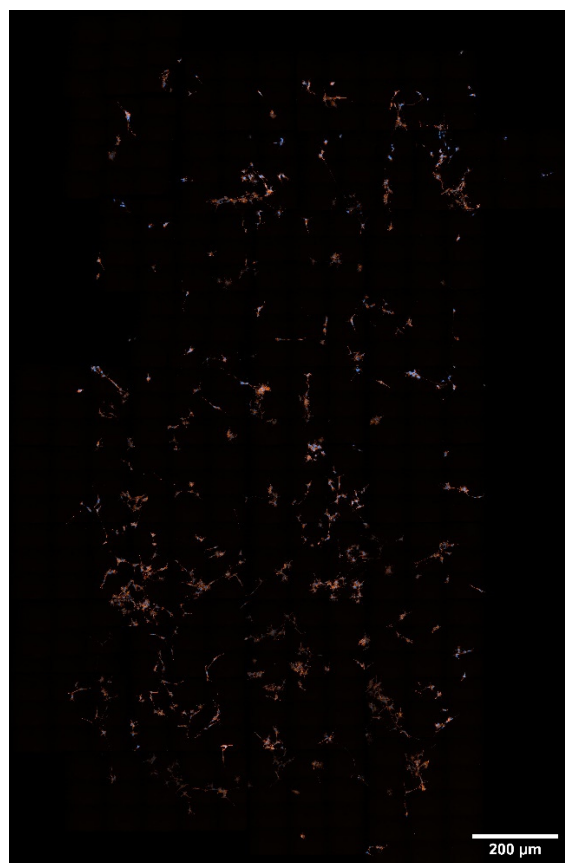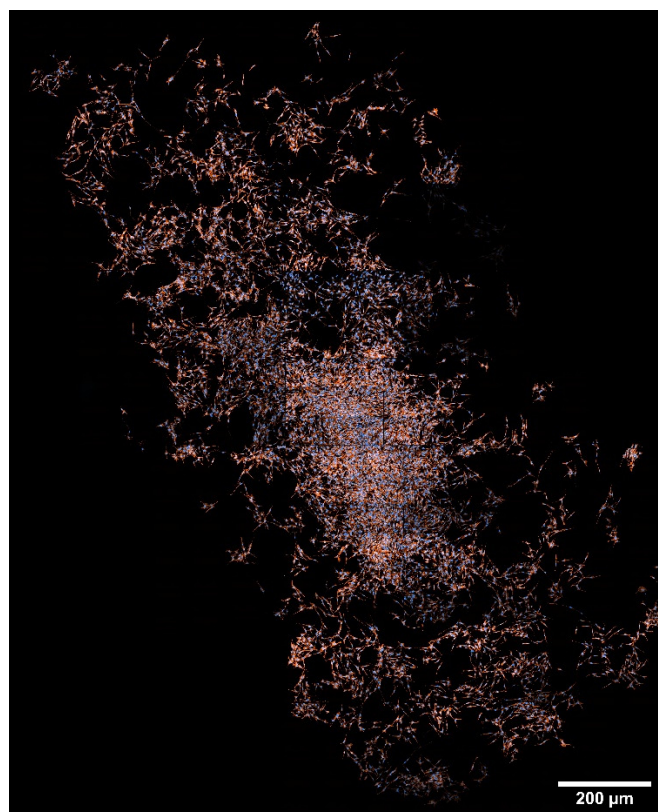**Figure S4.** Fluorescent image of SH-SY5Y cells grown on nanocolumnar TiN substrate for 3 days after differentiation. Actin fibers are shown in orange and cell nuclei in blue.

Laminin adsorption

We quantified the adsorption of the cell matrix glycoprotein laminin on electrode materials (Au, ITO, TiN, and TiN nano) using microplate reader measurements. To this end, we applied rhodamine-labeled laminin (Cat.No. LMN01, Cytoskeleton Inc., Denver, Colorado, USA) with a concentration of 10 µg/ml diluted in Millipore water to an area of 0.22 cm² resulting in a final concentration of 1.5 µg/cm² to the electrode substrates – a coating concentration often used for cell culture, see e.g. Pixley et al. [1] – and incubated the samples for 30 min at room temperature protected from light. Afterwards, non-adsorbed liquid was pipetted into a 96-well plate (Cat.No. 655086, Greiner Bio-One GmbH, Frickenhausen, Germany) and the fluorescence signal was analyzed with a microplate reader (Synergy H1 microplate reader, BioTek Instruments GmbH, Bad Friedrichshall, Germany). The light units were converted into protein mass using a calibration curve ranging from 0 µg to 1.5 µg rhodamin laminin diluted in Millipore water. We repeated this experiment three times for each electrode material type. The results of the analysis are shown in Figure S3. The relative adsorption is the difference between the initially applied and the non-adsorbed protein mass divided by the initial protein mass.
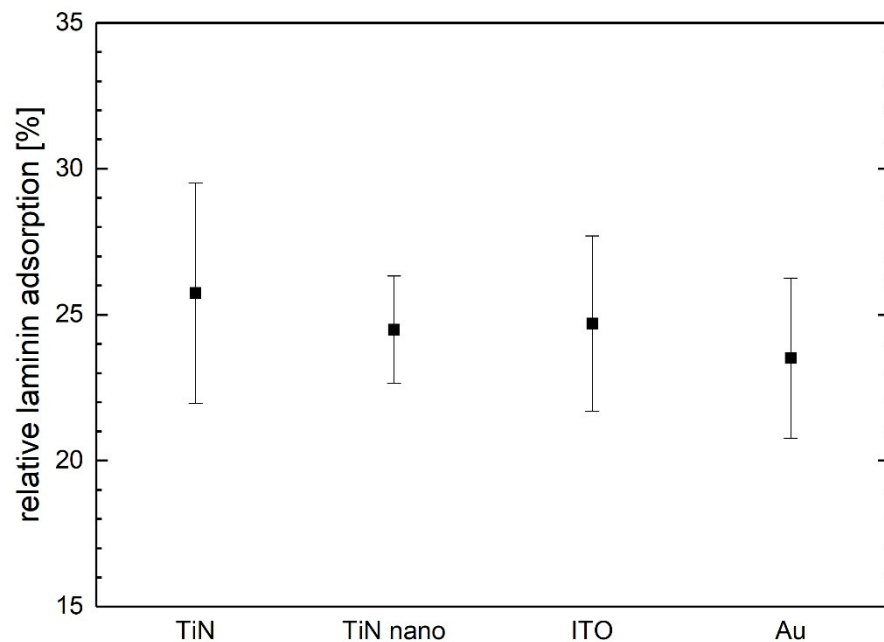
Figure S5. Relative laminin adsorption on different electrode material substrates.

References

1. Pixley, S.K.R.; Nieto-Sampedro, M.; Cotman, C.W. Preferential adhesion of brain astrocytes to laminin and central neurites to astrocytes. *J. Neurosci. Res.* **1987**, *18*, 402–406, doi:10.1002/jnr.490180304.

3.3. Neuronal and glial cell co-culture organization and impedance spectroscopy on nanocolumnar TiN films for lab-on-a-chip devices

The content of this chapter has been published in the manuscript "Neuronal and glial cell co-culture organization and impedance spectroscopy on nanocolumnar TiN films for lab-on-a-chip devices" [149].

Check for updates

Neuronal and glial cell co-culture organization and impedance spectroscopy on nanocolumnar TiN films for lab-on-a-chip devices†

Alice Abend,[a] Chelsie Steele,[a] Sabine Schmidt,[b] Ronny Frank,[b] Heinz-Georg Jahnke [ID]‡[b] and Mareike Zink [ID]*‡[a]

Lab-on-a-chip devices, such as multielectrode arrays (MEAs), offer great advantages to study function and behavior of biological cells, such as neurons, outside the complex tissue structure. Nevertheless, *in vitro* systems can only succeed if they represent realistic conditions such as cell organization as similarly found in tissues. In our study, we employ a co-culture system of neuron-like (SH-SY5Y) and glial-like (U-87 MG) cells with various neuron-glial ratios to model different brain regions with different cellular compositions *in vitro*. We find that cell behavior in terms of cellular organization, as well as proliferation, depends on neuron-glial cell ratio, as well as the underlying substrate material. In fact, nanocolumnar titanium nitride (TiN nano), which exhibits improved electric properties for neural recording on MEA, shows improved biocompatible features compared to indium tin oxide (ITO). Moreover, electrochemical impedance spectroscopy experiments allow us to monitor cellular processes label-free in real-time over several days with multielectrode arrays. Additionally, electrochemical impedance experiments reveal superiority of TiN with nanocolumnar surface modification in comparison with ITO. TiN nano exhibits enhanced relative cell signals and improved signal-to-noise ratio, especially for smaller electrode sizes, which makes nanocolumnar TiN a promising candidate for research on neural recording and stimulation.

Introduction

Neurodegenerative diseases such as epilepsy, Alzheimer's disease, and Parkinson's disease are on the rise. In fact, neurological disorders are the leading cause of disability, and the second leading cause of death worldwide.[1] The number of disability-adjusted life years has increased by 15%, and the absolute number of deaths by 39% during the last 30 years.[1] Aging was identified as the primary risk factor for neurodegenerative diseases[2] and rising patient numbers are no surprise in the light of increasing life expectancy.[3,4] Understanding the mechanisms underlying brain aging and the formation of neurodegeneration is still a work in progress.[5] The number of patients 50 years and older diagnosed with Parkinson's disease is expected to double in the world's most populated countries between 2005 and 2030 up to 9.3 million.[6] Additionally, the number of people affected by Alzheimer's disease is assumed to double every 20 years up to about 80 million cases by 2040 globally resulting in a single new patient every 7 seconds.[7] It is therefore imperative to study brain cell function to understand underlying biomechanical and biochemical mechanisms to encourage therapy development.

Major efforts have been made in both *in vivo* and *in vitro* research to study function and dysplasia of the brain, but many underlying biomedical processes are still not completely understood.[8] *In vivo* approaches based on animal models usually cannot account for the complexity of a human brain and lack some important human characteristics, in addition to the raised ethical concern of animal experiments, optical non-transparency, low throughput, and high cost.[9] In contrast, *in vitro* techniques usually do not account adequately for cell–matrix interactions and reciprocal action of different cell types and therefore fall short of mimicking *in vivo* tissue environments.[10] By comparing the response of cortical neurons of rats

[a]*Research Group Biotechnology and Biomedicine, Peter Debye Institute for Soft Matter Physics, Leipzig University, 04103 Leipzig, Germany.*
E-mail: zink@physik.uni-leipzig.de
[b]*Centre for Biotechnology and Biomedicine, Molecular Biological-Biochemical Processing Technology, Leipzig University, 04103 Leipzig, Germany*

in vivo and dissociated neurons *in vitro* exposed to drugs, Belle *et al.* proved that *in vitro* cultures may be appropriate for some, but not all, pharmacological studies.[11]

Great efforts have been made in recent years to bridge the gap between *in vivo* animal experiments and *in vitro* cell cultures, resulting in promising advances in biomimetic neural micro-environments, which mimic neural networks or structures found in the brain.[12,13] Such systems can offer great potential to study neural function, leading to the widespread field of brain-on-a-chip devices as, *e.g.*, illustrated by Brofiga *et al.*,[14] Maoz,[15] and Bang *et al.*[16] However, the idea to recreate organs on chips does not end with brains, but rather extends to other organs such as lung,[17] liver,[18] kidney,[19] heart,[20] bone,[21] skin,[22] and many more. Thus, such organ-on-a-chip devices recapitulate the key features of the physiology of human organs.[23]

The goal of brain-on-a-chip technologies is to mimic physiologic neuronal and glial cell interactions. This allows brain function replication and structural aspects on artificial platforms. Improvements in engineering and science have allowed for these types of lab-on-a-chip devices to be nicknamed 'mini-brain' models.[24] Some relevant examples range from microfluidic chambers, for mimicking the blood–brain barrier,[25] to 3D brain organoids derived from stem cells, to explore diseases in the human brain,[26] to organotypic brain slice cultures for glioblastoma cancer research.[27] However, there are still some limitations to these systems, such as, the number of functional interacting neuronal populations from different brain regions is still limited (for example amygdala, prefrontal cortex, and hippocampus cells as described by Dauth *et al.*[28]). Unfortunately, the devices lack the ability to simultaneously monitor relevant data on metabolic consumption and neurotransmitter concentration while performing measurements on electrophysiological activity of cells.[14]

Multielectrode arrays (MEAs) have become a popular tool to measure neuronal cell activity, due to their ability to record and stimulate cells at multiple sites simultaneously.[29] These devices can be used to study circuit connectivity, physiology, and pathology[30] long-term *in vitro* and *in vivo*. They provide the ability to examine cell health and function non-invasively.[31,32] Manufacturing processes of these promising lab-on-a-chip devices have already come a long way. Currently, 384-multiwell MEAs are used for impedance measurements of tau protein-induced neurodegenerative processes.[33] Even 3D MEAs have been developed to study function in three-dimensional neuronal cultures.[34] In fact, recently published work shows that long-term recordings of up to 79 days are possible in 3D neural cell cultures as a brain-on-a-chip with multielectrode arrays.[35]

Further improvement of the multielectrode array lab-on-a-chip devices and miniaturization of the electrodes give rise to new requirements for biomaterials. A lowered self-impedance of the electrodes is a prerequisite for even denser electrode arrays. Titanium nitride (TiN) is a promising candidate for such material, as it allows a reduction of electrode size without loss of sensitivity due to its increased surface area.[36–38] In our

previous work, we could already show an advantage of TiN with a further increased surface area due to a nanocolumnar surface patterning in terms of cell proliferation of neurons and glial cells in contrast to typical electrode materials such as gold and indium tin oxide (ITO).[39]

In our study, we show that a co-culture system of human neuron-like cells (SH-SY5Y) and glial-like cells (U-87 MG) co-cultured on titanium nitride (TiN) and nanocolumnar TiN (TiN nano) electrode biomaterials in comparison to indium tin oxide (ITO) substrates can be employed to investigate cell distribution and pattern formation *in vitro*. We study the interplay of both cell types while seeding neurons and glial cells in various ratios (80 : 20, 50 : 50, 20 : 80) onto the substrates and monitor growth patterns *via* confocal fluorescence microscopy. Analysis of cell organization is performed using radial autocorrelation functions and next neighbor analysis. Since various ratios of neurons and glial cells are present in different structures of the human brain,[40] our co-culture study is an *in vitro* model system for cellular organization employed on a lab-on-a-chip device. In order to demonstrate the advantage of TiN in contrast to ITO as electrode material, additional electrochemical impedance spectroscopy measurements allow us to monitor cellular processes label-free in real-time over several days. Our impedance spectroscopy experiments show technical superiority of nanocolumnar TiN over ITO in terms of enhanced relative impedance and reduced signal-to-noise ratios of the electrodes while co-culture tests hint at improved cell culture conditions of TiN nano. As we have shown before, TiN and TiN nano exhibit improved biocompatibility features compared to ITO and gold.[39,41] Thus, nanocolumnar TiN offers great potential for the fabrication of miniaturized MEAs.

Results

In our study, we investigate cell proliferation and pattern formation behavior of human neuronal cells SH-SY5Y (neuronal-like) and U-87 MG (glial cell-like) co-cultured on electrode biomaterials titanium nitride (TiN) and TiN with nanocolumnar surface patterning (TiN nano) in comparison with indium tin oxide (ITO). Information on surface topography of the materials is shown in Fig. S1, ESI.† The three materials display the following surface features: ITO shows a crystalline topography with the highest RMS roughness, followed by TiN nano and TiN, as verified by atomic force microscopy measurements. We see a cauliflower-like surface structure on TiN with several different grain sizes. However, TiN nano exhibits single-type grains with a nanocolumnar topography which leads to a surface area increase of (1.27 ± 0.08) nm for this material, while we measure only (1.10 ± 0.02) nm for ITO and even less (1.07 ± 0.01) nm for TiN. Please also refer to previous studies by Abend *et al.* for detailed material characterization.[39,41]

In order to study possible influences of SH-SY5Y to U-87 MG cell ratios on cell behavior, cells were seeded as a co-culture with different ratios of 80 : 20, 20 : 80, and 50 : 50 on

Biomaterials Science

the electrode materials, and cultured for either one or three days. Subsequently, samples were fixed and imaged. Having labeled the cell nuclei of SH-SY5Y and U-87 MG cells (for details of cell nucleus stain see methods section) before starting the co-culturing process, we are able to distinguish both cell types in the fluorescence images. An example of such images is shown in Fig. 1.

As a first step in assessing the cell proliferation, we counted cell nuclei of both neurons and glial cells on all 54 samples (3 seeding ratios × 2 culture times × 3 materials × 3 samples each = 54 samples overall). The results are shown in Fig. 2. Overall, we notice an impact of different cell seeding ratios on the cell proliferation of SH-SY5Y and U-87 MG cells on all tested materials. Generally, seeding of more SH-SY5Y cells than U-87 MG cells (80 : 20) leads to poor proliferation of both cell types, whereas starting with a superior number of U-87 MG cells (20 : 80) leads to an overgrowth of glial cells, and an initial ratio of 50 : 50 results in a proportional growth of neurons and glial cells. In case of 80 : 20 seeding, starting with a four times larger number of SH-SY5Y *versus* U-87 MG cells does not translate to enhanced growth of neuronal cells. Instead, on the contrary, both cell types grow in roughly equal numbers on all materials, but ITO provides the worst proliferation conditions here. After one day of culture with a ratio of 80 : 20, the number of neurons was about twice as high on TiN nano compared to ITO. Even though cell number of neurons was identical for TiN and TiN nano, the cell number halved on TiN. In contrast, when a cell ratio of 50 : 50 was employed, neurons proliferated and doubled on TiN nano, as well as ITO, while on TiN the cell number quintupled exceeding the glial cell
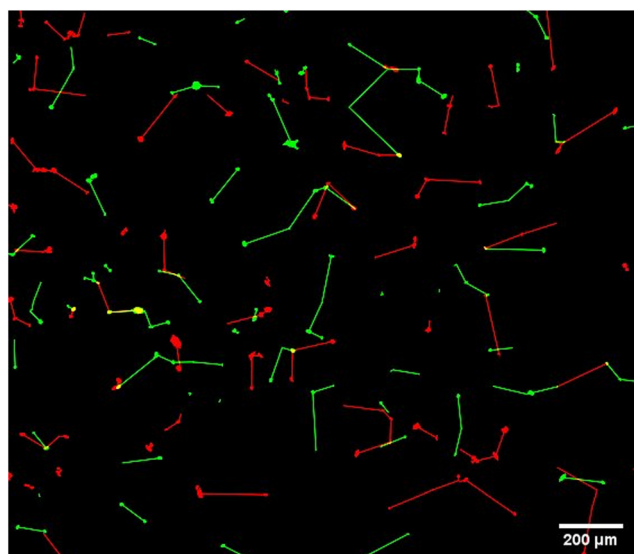

Fig. 2 Average number of cells grown on electrode materials (TiN nano, TiN, and ITO) for 1 or 3 days with different initial ratios of SH-SY5Y and U-87 MG cells. The bottom row in the diagram description shows the initial cell seeding ratio of SH-SY5Y to U-87 MG cells. We computed statistical significances within the seeding ratio groups and for the same culture times of either 1 day or 3 days. Error bars represent the SEM of three samples.

count for three days of culture. Taken together, for a ratio of 80 : 20 (neurons to glial cell ratio), best cell growth was seen on TiN nano, which was also the case for a ratio of 50 : 50. Culturing 20% SH-SY5Y and 80% U-87 MG cells together leads to an overgrowth of glial cells and neuronal cells are not able to catch up after three days of culture. This is most noticeable for ITO samples as we count simultaneously the highest number of glial cells and lowest number of neuronal cells for this substrate type for a 20 : 80 seeding ratio. The number of glial cells was almost twice as high after one day on TiN nano compared to ITO. However, after 3 days, most glial cells were detected on ITO, where the cell number doubled, as similarly occurring on unstructured TiN. TiN nano seems to provide improved culture conditions since we find the highest number of SH-SY5Y cells on this material after three days of culture and U-87 MG cells only proliferate moderately and do not overgrow the neuronal cells.

For the glial cells, we also observed good proliferation and cell growth on all three materials for a co-culture ratio of 50 : 50, where cell numbers more than doubled during culture time. Doubling of glial cell number was also present on TiN nano for a ratio of 80% neurons and 20% glial cells, while on TiN and ITO the cell number remained almost constant. In summary, U-87 MG glial cells grew well on all employed electrode materials except for a seeding ratio of 80 : 20 with only 20% glial cells. Here, best cell proliferation was seen on TiN nano.

Additionally, we further investigated cell distribution on electrode materials, taking the neuronal to glial cell ratio into account. To this end, we computed the nearest neighbor distance amongst SH-SY5Y cells and between U-87 MG cells. The

Fig. 1 Representative example of co-cultured SH-SY5Y cells (red) and U-87 MG cells (green) grown on electrode material (here: TiN with an initial seeding ratio of 50 : 50) for one day culture time. Only the cell nuclei were fluorescently labeled. Straight lines indicate nearest neighbor cells of the same type. The image shows only a small section of the complete cell network.
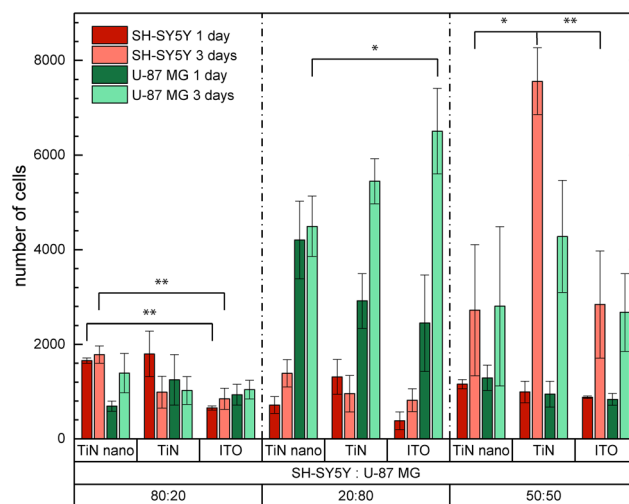
straight lines connecting cell nuclei in Fig. 1 illustrate the nearest neighbors of neuronal cells (red) and glial cells (green). We also measured the nearest neighbor distance between neuronal and glial cells, *i.e.* distance from one SH-SY5Y cell to the nearest neighboring U-87 MG cell. Results of the nearest neighbor analysis are shown in Fig. 3. Generally, we observe pairs of neuronal and glial cells to sit closer together on all materials for longer culture times indicated by the black and gray columns in the graph. This also becomes apparent from the histograms of nearest neighbor center-to-center distance of neuronal cells to the closest glial cell displayed in Fig. S2, ESI.† Conversely, for pairs of SH-SY5Y cells (Fig. 3 red) and pairs of U-87 MG cells (Fig. 3 green), this is not always the case. While we see significant proliferation of U-87 MG cells for the 20 : 80 cell seeding ratio (see Fig. 2), the glial cells do not seem to cluster together, but rather organize in the vicinity of neuronal cells. The distance between pairs of neuronal and glial cells is smaller than the distance amongst SH-SY5Y cells and between U-87 MG cells. A similar situation of rapid cell proliferation leading to close organization of neuronal and glial cells is observed for the 50 : 50 cell seeding ratio, albeit not as prominent. However, in case of the 80 : 20 cell seeding ratio, both SH-SY5Y and U-87 MG cells are lacking speedy cell proliferation (see Fig. 2) and organize so that pairs of cells of the same type sit closer together than cells of different types after three days of culture time.

We tested the statistical significance of the neuronal-glial co-localization to validate the results above. Measured data were compared to randomly generated data sets of the same size. For more details on the procedure see Gilles *et al.*[42] and Fig. S3, ESI.† We found our experimentally determined center-to-center distances of SH-SY5Y and U-87 MG cell pairs to be significantly different from randomized data.
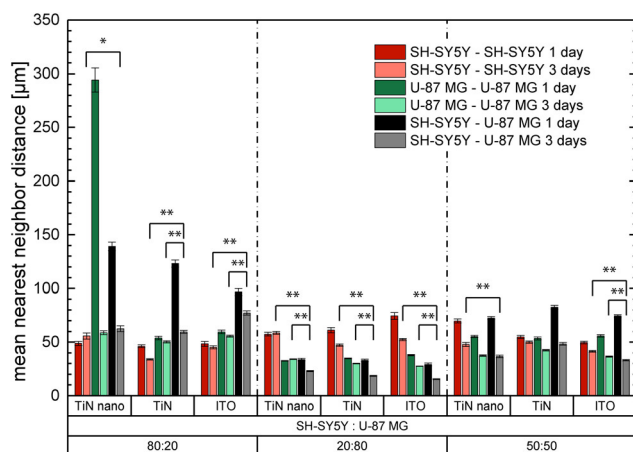
We further study cellular distributions on the three electrode materials as a function of co-culture ratios using a radially averaged autocorrelation analysis for both neuronal and glial cell nuclei separately for all 54 samples (3 seeding ratios × 2 culture times × 3 materials × 3 samples each = 54 samples overall). This function provides the average size of objects in an image (cell nuclei here) in conjunction with information about the typical distance between objects. Representative results of autocorrelation curves are shown in Fig. 4, *viz.* one example for each combination of material type, culture time, and cell seeding ratio. The other curves completing the data set of 54 samples can be found in Fig. S4, ESI.†

Generally, we see smooth and rapidly decreasing autocorrelation functions for our experiments. Similar to the findings on cell proliferation, we notice a pattern in the experimental results in the sense that cell behavior looks similar for samples with the same cell seeding ratio. Absolute values vary for different electrode materials, but the general appearance of data stays rather constant for equal seeding ratios. In case of the 80 : 20 seeding ratio of neuronal to glial cells, autocorrelation curves of neuronal cell data drop to zero with a cutoff at about 50 μm for TiN nano and ITO and 60 μm for TiN. Functions of U-87 MG cells also approach zero, but at a larger distance of 80 μm. The inverse seeding ratio of 20 : 80 exhibits a similar pattern concerning the SH-SY5Y cells but differs for the glial cells. The green U-87 MG functions generally have an offset in vertical direction and lie above their corresponding red curve for all samples. This behavior is consistent with changing culture times. In contrast, radially averaged autocorrelation curves of neuronal and glial cells almost always overlap for the 50 : 50 cell seeding ratio regardless of material type and culture time. We find the transition into the linear regime for neuronal cells at 50 μm for one day of culture and about 70 μm for three days. The transition for U-87 MG cells is shifted to slightly larger distances.

To validate nanocolumnar TiN in comparison to ITO as potential MEA material, we conducted electrochemical impedance spectroscopy measurements of co-cultured neurons and glial cells on microelectrode arrays made of TiN nano and ITO over several days. We investigated the influence of electrode materials as well as electrode size (diameter) on measured cell signal of SH-SY5Y cells, U-87 MG cells, and both cell types at a ratio of 50 : 50. In theory, smaller electrodes provide higher spatial resolution of cells cultured on them down to single-cell level, and even more importantly, higher cell signals can be achieved. However, in practice, this is offset by the increasing intrinsic impedance with decreasing electrode size. Thus, the detectable cell signal decreases below a certain electrode size.

We aim to improve this limitation by employing TiN with a nanocolumnar surface topography to lower the self-impedance of electrodes. Whether the cell signal in microelectrode arrays can be improved that way, and if so, in which frequency range is shown in Fig. 5 and 6. An example of a multielectrode array with circular electrodes of 10–200 μm diameter, which was used for the experiments, is displayed in Fig. 5a. Initial characterization without cells, but with cell culture medium, revealed

Fig. 3 Average nearest neighbor center-to-center distance of SH-SY5Y (red), U-87 MG cells (green), and pairs of neuronal and glial cells (black) grown on TiN nano, TiN, and ITO for 1 or 3 days. Bottom row of diagram description shows initial cell seeding ratio. We computed statistical significances within the seeding ratio groups and for the same culture times of either 1 day or 3 days. Error bars represent the SEM of three samples.

Fig. 4 Radially averaged autocorrelation analysis for cell nuclei positions obtained from 18 samples with different seeding ratios of U-87 MG cells (green) and SH-SY5Y cells (red) cultured on TiN nano, TiN, and ITO.

impedance magnitude spectra for TiN nano and ITO electrodes shown in Fig. 5b. We find typical curve shapes for electrode–electrolyte interfaces with high impedance values in the lower frequency range. This is followed by a decrease of impedance, due to the Helmholtz double layer formed at the interface (capacitive load), and a plateau mainly caused by spreading resistance (ohmic load). Spreading resistance occurs when electric current flows from the working electrode to the counter electrode and is mainly determined by the bulk resistance of the culture medium. We notice an increase of impedance in the upper kHz–MHz range only for ITO electrodes, which hints at an inductive effect. Additionally, the graph

shows a consistently lowered self-impedance for TiN nano in comparison to ITO over the whole frequency range. The smallest electrode size (10 μm) reveals the largest impedance magnitude of 7400 kΩ for ITO and 4710 kΩ for TiN nano at a frequency of 1 kHz. At 100 kHz, we measure 119 kΩ for 10 μm ITO electrodes and 86 kΩ for TiN nano.

Next, we recorded impedance spectra of TiN nano and ITO microelectrode arrays with and without cells to determine the cell signal (relative impedance). The resulting graphs are displayed in Fig. 6a. For more details on the computation of the relative impedance, please refer to the materials and methods section. We find the maximum cell signal in the range of 10
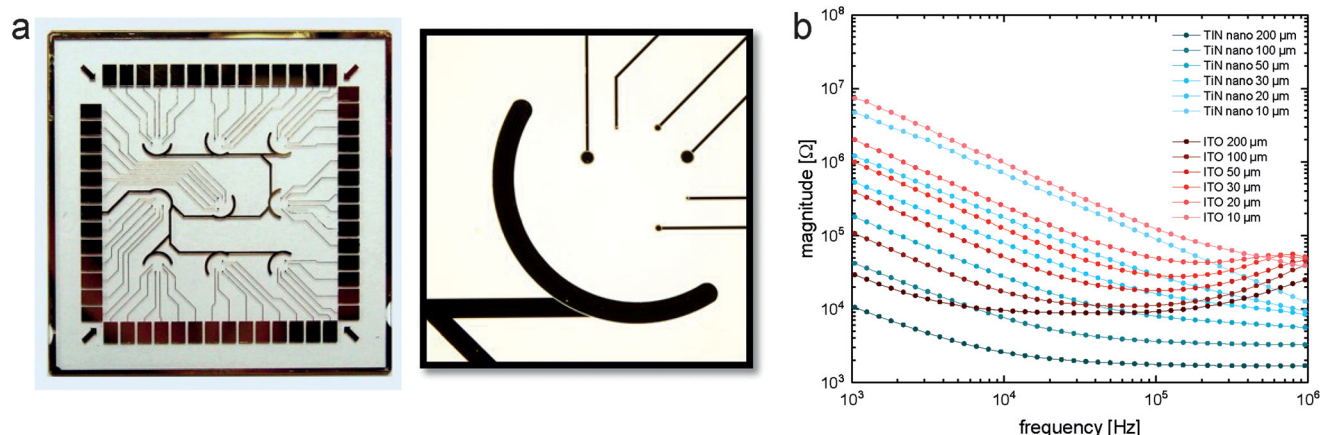
Fig. 5 (a) Microelectrode sensor chip consisting of electrodes fabricated on glass. Zoomed-in view of working electrodes of several diameters (10 μm, 20 μm, 30 μm, 50 μm, 100 μm, and 200 μm) in comparison to counter electrode. (b) Impedance magnitude as a function of frequency measured at TiN nano (blue) and ITO (red) electrodes of several diameters (mean, n = 15 electrodes).
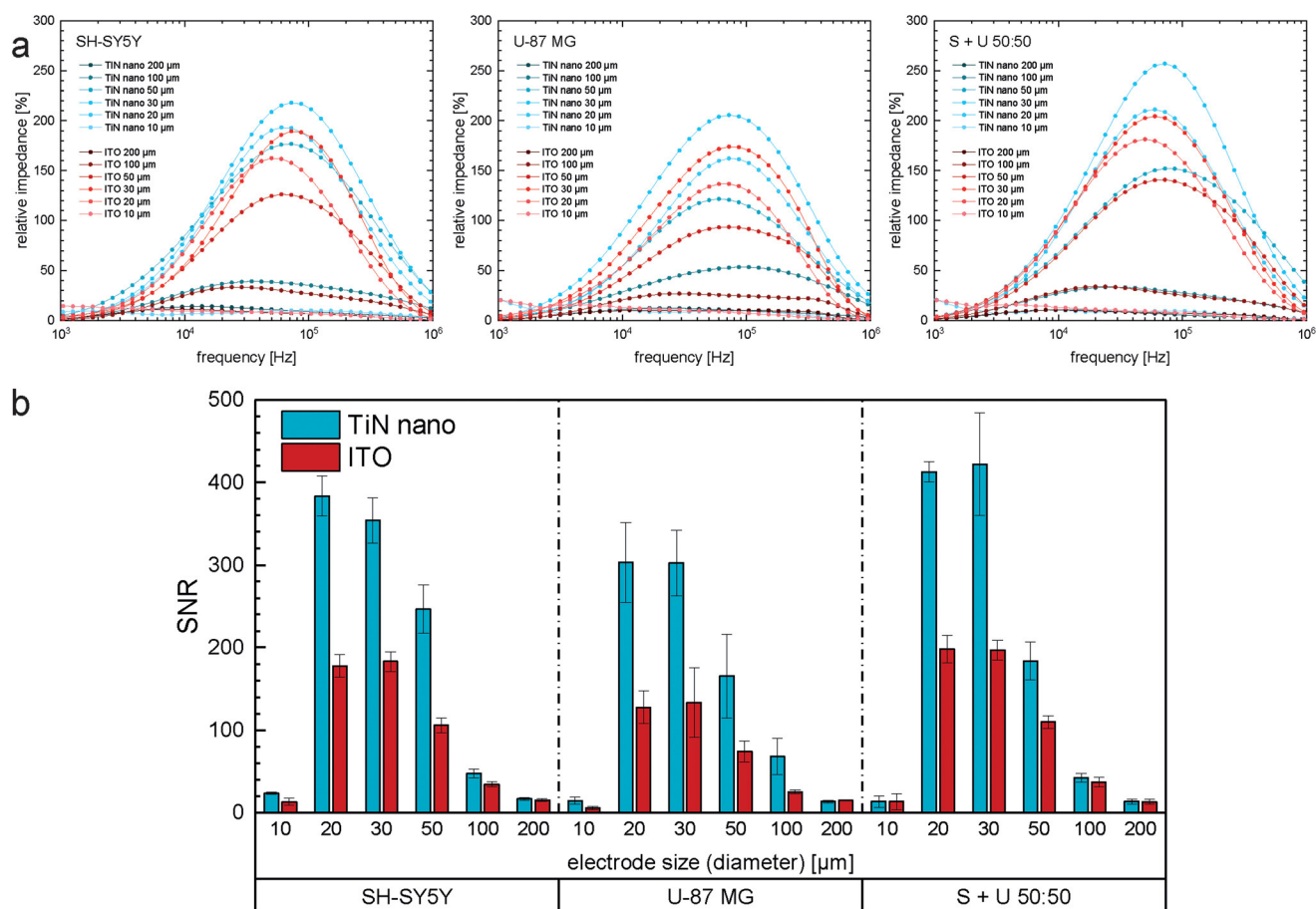
Fig. 6 (a) Relative impedance as a function of frequency measured for TiN nano (blue) and ITO (red) electrodes of several sizes with either SH-SY5Y cells or U-87 MG cells or both cell types seeded at a ratio of 50 : 50 (mean, n = 4 experiments). (b) Signal to noise ratio comparing impedance spectroscopy experiments with TiN nano (blue) and ITO (red) electrodes. Measurements were performed with SH-SY5Y cells or U-87 MG cells or both cell types at a ratio of 50 : 50 grown on sensor chips (mean ± sem, n = 4 experiments).

kHz–100 kHz for all experiments without notable differences between TiN nano and ITO electrodes. Electrodes of the sizes 50 μm, 100 μm, and 200 μm yield maximum relative impe-

dance values of only 100% and much lower. Smaller 20 μm and 30 μm electrodes deliver much larger values up to 250% for TiN nano with a 50 : 50 ratio of neuronal and glial cells and

200% for the mono-cultured cells on TiN nano. Interestingly, 10 μm electrodes yield continuously low relative impedance values comparable with the large electrodes. Directly comparing TiN nano with ITO reveals constantly higher cell signals on nanocolumnar TiN. Besides the measured cell signal, the occurring signal noise and consequently the signal-to-noise ratio (SNR) play an important role in measurements with devices with high self-impedance such as microelectrode arrays. We notice considerable differences in SNR between TiN nano and ITO for our experiments due to the lowered self-impedance of TiN nano as shown in Fig. 6b. Generally, the lowest SNR values are measured for U-87 MG cells and highest numbers are seen for a 50 : 50 ratio of neuronal and glial cells. Electrode sizes 20 μm and 30 μm yield the highest SNR resulting in the most sensitive measurements with these microelectrode arrays. Most importantly, TiN nano electrodes display a two times higher SNR for 20 μm and 30 μm size than ITO.

Discussion

In our study, we investigate neuronal (SH-SY5Y) and glial cell (U-87 MG) growth, as well as pattern formation and cell distribution on electrode materials (TiN nano, TiN, and ITO). Cells were co-cultured with three different seeding ratios of SH-SY5Y and U-87 MG cells: 50 : 50, 80 : 20, and 20 : 80. These specific ratios were chosen based on the cellular composition of human brains as described by Azevedo et al.[40] Overall, human brains consist of roughly 50% neurons and 50% non-neuronal cells, i.e. about 86 billion neurons and 84 billion non-neurons according to Azevedo. Hence, we investigate a 50 : 50 co-culture of neuronal and glial cells in our experiments. Moreover, in the gray and white matter of the cerebral cortex combined, we find about 20% neurons and 80% non-neuronal cells. The cerebral cortex accounts for more than half of the volume of the human brain and is suspected to be involved in neuronal computation necessary for perception, thought, language, and voluntary movement.[43] The composition of the cerebral cortex inspired our choice of a 20 : 80 co-culture. However, the brain region called cerebellum houses the highest number of neurons in the human brain resulting in a ratio of roughly 80% neurons and 20% non-neuronal cells,[40] which justifies our 80 : 20 co-culture ratio. The cerebellum is known for its crucial role in coordinating voluntary movement and the control of vestibular systems, but research nowadays also focuses on the cerebellum's responsibility for cognitive and emotional functions.[44]

The brain does not only have a heterogeneous architecture in terms of growth ratio of neuronal and non-neuronal cell types, but neurons and glial cells also form different cell patterns in different parts of the brain. For example, Ravi et al. show in their study about organotypic brain slices acute sections of healthy human cerebral cortex labeled for neuronal marker NeuN and astrocyte marker GFAP.[45] Both cell types are uniformly distributed and form a homogeneous cell pattern. We see this type of cell growth mostly for our samples with

seeding ratios of 20 : 80 and 50 : 50, especially for longer culture times. Cells organize so that pairs of neurons and glial cells sit closer together than cells of the same cell type. Hence, our model of the cerebral cortex (co-culture with 20% SH-SY5Y and 80% U-87 MG cells) resembles the real human cerebral cortex in terms of cellular architecture. On the other hand, neurons in the cerebellum and hippocampus for example are more tightly packed. Immunostained tissue sections of mouse brain slices have been published by Er et al. in their study about a novel fluorescent probe for live neuron labeling.[46] GFAP-positive astrocytes have a homogenous distribution which is pervaded by the NeuN-positive cell layer. Studying the samples with an 80 : 20 co-culture ratio, we notice that distances among U-87 MG cells and in between SH-SY5Y cells are shorter than distances from one U-87 MG cell to the next neighbor SH-SY5Y cell. Thus, cells of the same type sit closer together than cell pairs of different types, especially for longer culture times. Although we do not see the formation of dense layers of neurons, as they appear in brain slices in our experiments, our model system for the cerebellum (i.e. the 80 : 20 co-culture of SH-SY5Y and U-87 MG cells) resembles the architecture of the cerebellum region more than the cerebral cortex for example.

Inserting neuroelectrodes in patients' brains for therapeutic purposes is always a traumatic procedure, and leads to disruption of neuronal tissue and blood vessels which triggers a number of morphological and metabolic changes.[47] Cell patterns surrounding long-term implants are often characterized by glial scar formation. Glial scars comprise astroglial encapsulation of the implant and persistent inflammatory response at the brain-machine interface. This leads to a loss of neurons in the vicinity of the neuroelectrode.[47,48] Countermeasures include biomimetic coatings of electrodes, for example brain-derived neuronal-specific adhesion molecules, as presented by Golabchi et al.,[49] or the fabrication of neuronal probes designed to be structurally and mechanically similar to neurons as shown by Yang et al.[50] Coatings can lead to a significantly lowered microglial activation and increased neuronal density at the brain-device interface which improves effectiveness of the device.[49,51–53] Also, the biomimetic neuronal probes from Yang et al. lead to a rather uniform distribution of neuronal and glial cell types at the implant-brain interface instead of neuronal depletion and astroglial enhancement. We conclude that our results of homogenously organized SH-SY5Y and U-87 MG cells on electrode materials hint at favorable implant conditions, especially for the 20 : 80 and 50 : 50 seeding ratios. Also taking cell proliferation experiments into account, TiN nano seems to be a promising candidate for medical probes.

Comparing our fluorescence images with autocorrelation data, we notice that the offset between autocorrelation curves of SH-SY5Y and U-87 MG cells for 20 : 80 cell ratio possibly stems from the overgrowth of glial cells which is detected as a large agglomeration of glial cells in comparison to sparsely appearing neuronal cells. The overlap of autocorrelation curves for 50 : 50 cell ratio might derive from the equal growth

of both cell types and the homogeneous distribution of cells. Overall equal growth of neuronal and glial cells on 80 : 20 cell seeding ratio samples, however, results in larger distances between SH-SY5Y and U-87 MG cells than among cells of the same type. Small agglomerations of glial cells surrounding neuronal cells could possibly lead to the offset of autocorrelation functions in the x-direction.

Co-cultured SH-SY5Y and U-87 MG cells exhibit vastly different cell organization on electrode materials TiN, TiN nano, and ITO compared to mono-cultured cells. In our previous study, we noticed the formation of large cell agglomerations.[39] Such cell clusters were most prominent for SH-SY5Y cells cultured in TiN materials, whereas U-87 MG cells formed smaller agglomerations that were fairly evenly distributed on the substrates. Here in this study, co-cultured neuron-like and glial-like cells form more homogeneously distributed cell patterns where cells of different types tend to sit closer together than cells of the same type. The seeding density is low enough for all cells (glial and neuronal) to occupy space on the substrates and not on top of each other. Since all experimental parameters (except fluorescent stain) and culture conditions were equal to the former study, we conclude that the direct interaction between neuron-like and glial-like cells is essential for resulting cell growth and organization. In fact, the importance of cellular interaction in co-culture systems to mimic blood–brain barrier functions with immortalized cell lines (including SH-SY5Y) has been studied by Idris et al. with the verdict that only direct contact of cells of different types and triple co-culture systems closely mimic the in vivo blood–brain barrier conditions.[54]

Cell morphology and adhesion studies of the employed cell lines on electrode materials ITO, TiN, and TiN nano are included in our previous study.[41] We expect the cell-surface adhesion and spreading behavior to be similar.

Considering ITO and TiN nano as potential candidates for electronic brain-machine interfaces, initial characterization of microelectrode arrays without cells revealed impedance magnitude spectra for ITO which are comparable with results from a former study of ITO microelectrodes (50–200 μm) by Jahnke et al.[55] Also, the atypical increase of impedance in the upper kHz–MHz range for ITO electrodes due to the presumed inductive effect is consistent with former experiments.[55] This inductive impedance has not yet been observed for other materials such as gold[55] and neither do we see such an effect for TiN nano in our study. TiN nano shows a consistently lowered self-impedance in comparison to ITO in the lower as well as the middle frequency range. This lowered self-impedance creates favorable conditions for microelectrode arrays since usually the intrinsic impedance increases with decreasing electrode size and therefore renders cell signals undetectable below a certain (material-dependent) electrode size. In other words, materials with lowered self-impedance allow the fabrication of smaller electrodes and denser electrode arrays, which increases the spatial resolution of measurements. A lowered self-impedance of nano rough TiN in comparison with stainless steel electrodes has also been reported recently by Schmitz

et al.[56] In their experiments, the effect was observed only in the lower frequency range <1 kHz. However, in our results, we found the intrinsic impedance of TiN nano to be consistently lower than ITO for frequencies up to 100 kHz, and even 1 MHz due to the inductive effect in ITO. We speculate that the lowered self-impedance effect vanishing for frequencies over 1 kHz might be caused by the much larger electrode size (3–5 mm) in comparison to our experiments (10–200 μm). Schmitz et al. also recorded the transepithelial electrical resistance for both nano rough TiN and stainless steel electrodes in cell culture experiments finding favorable cell conditions for TiN nano electrodes over a culture time of 21 days.

Additionally, we employed ITO and TiN nano microelectrode arrays to record impedance spectra with SH-SY5Y and U-87 MG cells, as well as co-culture systems with a 50 : 50 ratio, to compute the cell signal, i.e. relative impedance. Resulting curve shapes closely resemble data published by Jahnke et al.[55] measured with ITO electrodes and HEK cells. However, their maximum measured relative impedance values are much higher for the same size of ITO electrodes in comparison to our experiments. Jahnke et al. observe a relative impedance of about 200% for 50 μm ITO electrodes with HEK cells whereas we measure only 125% for ITO electrodes with SH-SY5Y cells, 95% for U-87 MG cells, and 140% for a ratio of 50 : 50 neurons and glial cells. We speculate that this is due to the more epithelial character of the HEK cells in comparison to our neuronal cell lines since epithelial cell types tend to form denser cell layers and their cell–cell contacts differ from neuronal cells. Also, Jahnke et al. used a collagen coating for their electrode substrates to improve cell–substrate adhesion. Nevertheless, we can also reach maximum impedance values of about 200% for all cell types and seeding ratios in our experiments with a smaller electrode size (30 μm ITO and 20–30 μm TiN nano). In fact, we observe the highest cell signal of 250% for 30 μm TiN nano electrodes for the 50 : 50 co-cultured neurons and glial cells. Thus, microelectrodes composed of TiN nano exhibit improved signal-to-noise ratios compared to ITO microelectrode arrays.

Experimental

Electrode material preparation

In our study, we used the following electrode material substrates: indium tin oxide (ITO) and titanium nitride with two different surface topographies (TiN and TiN nano). Specimens were produced by thin film deposition on 13 mm glass coverslips with a thickness of 0.13–0.16 mm (VWR GmbH, Darmstadt, Germany). Before coating, coverslips were washed with acetone and isopropanol in an ultrasonic bath, treated with 3% hydrofluoric acid for 2 min, and rinsed with ultrapure water. A coating setup (CREAMET 500, Creavac GmbH, Dresden, Germany) was used to sputter metallic coatings onto the glass. ITO plating was achieved with a 4″ indium tin oxide target (90 : 10 wt%, EVOCHEM GmbH, Offenbach am Main, Germany) and a working pressure of 4.5×10^{-3} mbar. The

argon flow rate was set to 18 sccm with a working distance of 150 mm for 20 min and a combined power of 250 W (DC) and 85 W (RF). Subsequent heat treatment of the samples at 400 °C for 10 min increased the transparency of the deposited ITO material.

Titanium nitride samples were produced using a titanium layer as adhesion promoter with a 4″ titanium target (99.99%, Kurt J. Lesker Company, Jefferson Hills, PA, USA) at 4.5×10^{-3} mbar with an argon flow rate of 18 sccm for a sputtering time of 5 min. Working distance was set to 150 mm and power was 500 W (DC). As the next step, we added a gold layer on top of the titanium coating. The gold layer was produced using a 4″ gold target (99.99%, Heimerle&Meule GmbH, Pforzheim, Germany) at 4.5×10^{-3} mbar, 350 W (DC), a working distance of 150 mm, and an argon flow rate of 18 sccm for 3 min. Afterward, titanium was layered on top of the gold surface using the same titanium target, pressure, and working distance as described above. Argon flow rate was thereby reduced to 11 sccm and we added a 99.95% pure nitrogen flow at 6 sccm. Sputtering power was set to 600 W (DC). Different sputter times for TiN of 2.5 min and 40 min resulted in a film thickness of 150–200 nm for TiN and 500–550 nm for TiN nano (also termed nanocolumnar TiN), respectively.

Atomic force microscopy-based surface characterization of the electrode materials is shown in the ESI.† ITO exhibits a crystalline surface topography and showed the highest RMS roughness followed by TiN nano and TiN. The latter reveals a cauliflower-like structure with a variety of grain sizes while TiN nano has single-type grains with nanocolumnar surface topography. The nano-sized columns lead to a surface area increase (1.27 ± 0.08) nm for TiN nano. In contrast, we measured (1.10 ± 0.02) nm for ITO and even less (1.07 ± 0.01) nm for TiN.

Cell culture

We used the human neuroblastoma SH-SY5Y (Cat. No. CRL-2266, ATCC LGC Standards GmbH, Wesel, Germany) and glioblastoma U-87 MG (Cat. No. 300367, CLS Cell Lines Service GmbH, Eppelheim, Germany) cell lines for the presented study. Both cell types were cultured in a 1 : 1 mixture of MEM Eagle/Ham's F12 containing Earle's salts, L-glutamine, and sodium bicarbonate (Cat. No. M4655 and N6658, Sigma-Aldrich Chemie GmbH, Munich, Germany). Cell culture medium was supplemented with 10% fetal bovine serum (Cat. No. S0615, Biochrom GmbH, Berlin, Germany) and 1% penicillin/streptomycin (Cat. No. P0781, Sigma-Aldrich Chemie GmbH, Munich, Germany). Cells were maintained at 37 °C in culture flasks in a 95% air and 5% CO_2 atmosphere. Culture medium was changed every other day and cells were passaged once a week with a ratio of 1 : 10 in case of the U-87 MG cells and 1 : 5 for the SH-SY5Y cells. We used a blend of phosphate-buffered saline (PBS, Cat. No. 18912014, Gibco, Thermo Fisher Scientific, Waltham, MA, USA), 0.025% (w/v) trypsin, and 0.011% ethylenediaminetetraacetic acid (EDTA, Cat. No. L2143, Biochrom GmbH, Berlin, Germany) applied for 3–4 minutes before cell counting and seeding.

Co-culture cell staining and imaging

In our study, we analyzed cellular organization in terms of cell distribution and growth pattern formation of both U-87 MG and SH-SY5Y cells as a co-culture on the electrode biomaterials ITO, TiN, and nanocolumnar TiN, respectively. The nuclei of both cell types were fluorescently labeled before seeding them onto the electrode substrates in co-culture, in order to distinguish neurons and glial cells in the subsequently acquired fluorescence microscopy images. We eventually decided against antibody staining since we always observed some degree of cross staining even though the antibodies should have been specific enough according to the manufacturers. Thus, we were not able to distinguish the cell types by antibody staining and decided to use the following staining procedure:

Before fluorescent labeling, SH-SH5Y cells were supplemented with 20 nM staurosporine (Cat. No. S5921, Sigma-Aldrich Chemie GmbH, Munich, Germany) for 72 h. This initiates the differentiation process.[57] We used CellLight® reagents to label the nuclei of U-87 MG cells with RFP (Cat. No. C10603, Invitrogen by Thermo Fisher Scientific, Waltham, MA, USA) and GFP (Cat. No. C10602, Invitrogen by Thermo Fisher Scientific, Waltham, MA, USA) for the SH-SY5Y cells *via* transduction. In doing so, we are able to distinguish between both cell types in the fluorescent images of the co-culture by emission color. Concentration was chosen following the manufacturer's instructions as 30 particles per cell diluted in cell culture medium. Cells were incubated with the staining solution for 24 h at 37 °C and 5% CO_2.

Afterward, cells were passaged using trypsin/EDTA as described above and counted in an automatic optical cell counter (EVE™, NanoEntek Inc., Seoul, Korea). We seeded neurons and glial cells with ratios of 50 : 50, 80 : 20, and 20 : 80 of both cell types at an overall density of 230 cells per mm² onto electrode substrate materials ITO, TiN, and nanocolumnar TiN, respectively. Cells were cultured on the electrode substrates in complete medium as a co-culture.

In order to investigate cellular organization on the substrates 1 and 3 days after seeding half of the samples were fixed after 24 h and the other half after 72 h with paraformaldehyde (Cat. No. HT501128, Sigma-Aldrich Chemie GmbH, Munich, Germany) for 15 min and washed three times with PBS. Samples were placed upside down in Petri dishes (Cat. No. 80136, ibidi GmbH, Gräfeling, Germany) with mounting medium (Cat. No. 50001, ibidi GmbH, Gräfeling, Germany) sandwiched between sample and dish. Specimens were stored at 4 °C before imaging.

Cell distribution was imaged using confocal laser scanning microscopy. Images were taken employing an inverted Zeiss Axio Observer.Z1 microscope equipped with a spinning disk unit (Yokogawa CSU-X1A 5000, Tokyo, Japan) and a 25× glycerin immersion objective. An area of 0.22 cm² was imaged for each sample. We imaged 54 samples overall using 3 cell seeding ratios, 2 culture times, 3 electrode materials, and 3 specimens each. Up to 60 individual two-channel images were necessary to cover the cell growth area of every specimen.

Image analysis – nearest neighbor distance

We investigated cellular distribution on electrode materials by analyzing the distance to the respective nearest neighbor cell of every cell in the network. We first measured the distance of neuronal and glial cell nuclei in the fluorescence microscopy images using a Fiji distribution[58] (Windows 10, 64-bit version) based on ImageJ software.[59] Two-channel fluorescence images were split (single channel for each cell type), thresholded, binarized, and watershed. The distance between two cells was always defined by the center-to-center distance of the cell nuclei. We employed the plugin "NnD – Nearest Neighbor Distance" to measure the distance between cells of the same type, *i.e.* cells in either the glial cell channel or the neuronal cell channel of the microscopy images. Additionally, we used the "Cluster Analysis of Nuclei Tool" plugin for visualization of nearest neighbors of the same cell type. Distances of neuronal cells to the nearest neighbor glial cell were measured using the "DiAna – Distance Analysis" plugin[42] for all samples. This tool was also used to compare our measured data with randomized data sets of the same size.

Image analysis – radial autocorrelation function

We employed a radial autocorrelation analysis in order to investigate cellular distribution on the different electrode materials. A detailed description of the data processing workflow can be found in the ESI† and our previous publication.[39] Briefly, fluorescence microscopy images were processed using Fiji distribution[58] (Windows 10, 64-bit version) based on ImageJ software.[59] Cell nuclei positions were identified on binarized and thresholded images with the particle tracker tool from ImageJ. Co-cultured U-87 MG and SH-SY5Y cells were distinguished from one another by color (red and green) in the fluorescence images. We used the "Radially Averaged Autocorrelation" macro and "Radial Profile" plugin to compute the radially averaged two-point autocorrelation function for both cell types individually on all co-culture samples. The autocorrelation function provides information on the spatial distribution of objects in a given data set as well as on a distribution of the size of objects (*i.e.* cluster of cell nuclei) in the picture, as described by Baker *et al.*[60] and Berryman *et al.*[61] We normalize the results so that the value of the autocorrelation function at distance $r = 0$ will always be 1 (perfect correlation) while the value 0 denotes the case of no correlation.

Microelectrode array fabrication

Microelectrode arrays (MEAs) were fabricated in a clean room with the same material depositing steps and process parameters as described for the "electrode material preparation". For the structuring, lift-off technique was used as previously described by Jahnke *et al.*[55]

Briefly, borofloat glass substrate surfaces (49 × 49 × 1 mm, Industriearmaturen Goettgens GmbH, Würselen, Germany) were cleaned by piranha etching followed by intensive washing with ultrapure water. For structuring, substrates were spin-coated with negative resist AR-N 4340 (Allresist, Strausberg, Germany). After soft baking, chrome photomasks (Compugraphics GmbH, Jena, Germany) were used in combination with a MA6 mask aligner (350–405 nm, exposure time 8 s; Süss MicroTec, Garching, Germany) to transfer the chip layout to the substrate. After a post-exposure bake step (60 s, 95 °C) structures were developed in AR-N 300–475 (Allresist, Strausberg, Germany), rinsed, and dried. After electrode material deposition, the negative resist was removed by incubation in acetone followed by extensive washing with isopropanol and ultrapure water prior to dehydration at 200 °C for at least 30 min. For electrical insulation of conducting paths and definition of microelectrode structures, a SU-8_2 (Micro Resist Technology GmbH, Berlin, Germany) insulation layer of 2 μm thickness was added *via* spin coating, pre-bake (1 min, 65 °C) followed by soft-bake (1 min, 95 °C), 4 s UV exposure, post-exposure bake (1 min at 65 °C followed by 1 min at 95 °C) and 1 min development in mr-Dev 600 (MicroChem, Germany). Finally, MEAs were cleaned in ultrapure water, spin-dried and dehydrated at 95 °C. Finally, 3 × 3 culture chambers in 96-well format (Greiner Bio-One GmbH, Leipzig, Germany) were bonded with biocompatible silicone LOCTITE 5366 (Henkel GmbH) onto MEAs.

Electrochemical impedance spectroscopy

For the impedimetric analysis of achievable cell signals, MEAs were placed into a self-developed multiplexer[55] frontend within a cell incubator (37 °C, 5% CO_2 in a humidified atmosphere) and impedance spectra were acquired every 5 minutes using a high-precision impedance analyzer Agilent 4294A (Agilent Technologies, Santa Clara, CA, USA) with 10 mV alternating voltage in a frequency range of 500 Hz to 5 MHz. After 24 hours, all recorded impedance spectra were analyzed by self-developed software IDAT v4.[55] The program can directly import measurement raw data files, and sort and group all electrodes according to the chosen chip layout which can be easily chosen by the user in a graphical user interface. Thus, large data sets can be analyzed within minutes instead of copying and grouping thousands of spectra manually. In the data analysis first step, the cellular contribution to the impedance magnitude spectra was extracted (relative impedance) with the help of blank value (without cells) spectra ($|Z|$covered − $|Z|$cell-free)/($|Z|$cell-free × 100%). Next, the maximum relative impedance value for every single electrode within the monitored time range of 24 hours was identified and used for statistical analysis. For each experiment with cells two to three MEAs per electrode material were used with nine electrodes of each size on each MEA.

Statistical analysis

We repeated the cell proliferation and next neighbor distance analysis for each cell ratio, growth time, and electrode material three times. In total, we analyzed 225 000 cells. Data averages are expressed as the arithmetic mean ± standard error of the mean.

Two-sample *t*-test in OriginLab software (OriginPro 2017G, OriginLab Corporation, Northampton, MA, USA) was employed to analyze statistical significance of data sets. Data values were marked as significant (*) for $p \leq 0.05$ and highly significant (**) for $p \leq 0.01$. Statistical significances were computed for data within the same cell seeding ratio groups and for the same culture time of either 1 or 3 days.

Conclusions

While single-cell cultures have the advantage of being easy to handle, they only mirror *in vivo* behavior to limited extent. In contrast, our co-culture system of neurons and glial cells makes it possible to model different brain regions *in vitro* by varying the ratio of neuronal and glial cells. Co-culture experiments with different ratios of SH-SY5Y and U-87 MG cells overall show favorable growth conditions for electrode materials composed of nanocolumnar TiN, which hint at possible *in vivo* applications of nanocolumnar TiN electrodes in future experiments. These results need to be verified in future studies involving primary mammalian neuronal and glial cells since cell lines do not fully represent physiological features of cells and tissue. Impedance spectroscopy experiments revealed higher relative impedance and improved signal-to-noise values for TiN nano in comparison with ITO. Thus, a co-culture system of neurons and glial cells in combination with MEAs is a promising brain-on-a-chip system that offers the possibility to study new agents and the effect of drugs *in vitro*.

Author contributions

Conceptualization, M. Z.; methodology, A. A., C. S., and H.-G. J.; software, A. A. and C. S.; validation, A. A., C. S., H.-G. J. and M. Z.; formal analysis, A. A., C. S., and R. F.; resources, S. S., H.-G. J. and M. Z.; data curation, A. A., C. S., H.-G. J., and M. Z.; writing—original draft preparation, A. A., and M. Z.; writing, review and editing, A. A., C. S., H.-G. J. and M. Z.; visualization, A. A.; supervision, M. Z.; project administration, M. Z. and H.-G. J.; funding acquisition, M. Z., and H.-G. J. All authors have read and agreed to the published version of the manuscript.

Conflicts of interest

There are no conflicts to declare.

Acknowledgements

References

1 V. L. Feigin, T. Vos, E. Nichols, M. O. Owolabi, W. M. Carroll, M. Dichgans, G. Deuschl, P. Parmar, M. Brainin and C. Murray, *Lancet Neurol.*, 2020, **19**, 255–265.

2 Y. Hou, X. Dan, M. Babbar, Y. Wei, S. G. Hasselbalch, D. L. Croteau and V. A. Bohr, *Nat. Rev. Neurol.*, 2019, **15**, 565–581.

3 M.-T. Heemels, *Nature*, 2016, **539**, 179–179.

4 Y. Béjot and K. Yaffe, *Neuroepidemiology*, 2019, **52**, 76–77.

5 T. Wyss-Coray, *Nature*, 2016, **539**, 180–186.

6 V. P. Calabrese, E. R. Dorsey, R. Constantinescu, J. P. Thompson, K. M. Biglan, R. G. Holloway, K. Kieburtz, F. J. Marshall, B. M. Ravina, G. Schifitto, A. Siderowf and C. M. Tanner, *Neurology*, 2007, **69**, 223–224.

7 C. P. Ferri, M. Prince, C. Brayne, H. Brodaty, L. Fratiglioni, M. Ganguli, K. Hall, K. Hasegawa, H. Hendrie, Y. Huang, A. Jorm, C. Mathers, P. R. Menezes, E. Rimmer and M. Scazufca, *Lancet*, 2005, **366**, 2112–2117.

8 A. B. Young, *J. Neurosci.*, 2009, **29**, 12722–12728.

9 P. Nikolakopoulou, R. Rauti, D. Voulgaris, I. Shlomy, B. M. Maoz and A. Herland, *Brain*, 2020, **143**, 3181–3213.

10 M. Alaylioglu, E. Dursun, S. Yilmazer and D. Gezen-Ak, *Arch. Neuropsychiatry*, 2020, **57**, 333–337.

11 A. M. Belle, H. A. Enright, A. P. Sales, K. Kulp, J. Osburn, E. A. Kuhn, N. O. Fischer and E. K. Wheeler, *Sci. Rep.*, 2018, **8**, 10820.

12 M. Seiti, P. S. Ginestra, E. Ceretti, E. Ferraris and A. Ranga, *Adv. Mater. Interfaces*, 2022, **9**, 2101297.

13 A. Ozgun, D. Lomboni, H. Arnott, W. A. Staines, J. Woulfe and F. Variola, *Biomater. Sci.*, 2022, **10**, 1134–1165.

14 M. Brofiga, M. Pisano, R. Raiteri and P. Massobrio, *J. Neural Eng.*, 2021, **18**, 041005.

15 B. M. Maoz, *APL Bioeng.*, 2021, **5**, 030902.

16 S. Bang, S. Jeong, N. Choi and H. N. Kim, *Biomicrofluidics*, 2019, **13**, 051301.

17 D. Huh, B. D. Matthews, A. Mammoto, M. Montoya-Zavala, H. Y. Hsin and D. E. Ingber, *Science*, 2010, **328**, 1662–1668.

18 D. Bavli, S. Prill, E. Ezra, G. Levy, M. Cohen, M. Vinken, J. Vanfleteren, M. Jaeger and Y. Nahmias, *Proc. Natl. Acad. Sci. U. S. A.*, 2016, **113**, E2231–E2240.

19 L. Yin, G. Du, B. Zhang, H. Zhang, R. Yin, W. Zhang and S.-M. Yang, *Sci. Rep.*, 2020, **10**, 6568.

20 M. Kitsara, D. Kontziampasis, O. Agbulut and Y. Chen, *Microelectron. Eng.*, 2019, **203–204**, 44–62.

21 H. Bahmaee, R. Owen, L. Boyle, C. M. Perrault, A. A. Garcia-Granada, G. C. Reilly and F. Claeyssens, *Front. Bioeng. Biotechnol.*, 2020, **8**, 1–17.

22 I. Risueño, L. Valencia, J. L. Jorcano and D. Velasco, *APL Bioeng.*, 2021, **5**, 030901.

23 Y. Zhu, K. Mandal, A. L. Hernandez, S. Kawakita, W. Huang, P. Bandaru, S. Ahadian, H.-J. Kim, V. Jucaud, M. R. Dokmeci and A. Khademhosseini, *Curr. Opin. Biomed. Eng.*, 2021, **19**, 100309.

24 H.-Y. Tan, H. Cho and L. P. Lee, *Nat. Biomed. Eng.*, 2021, **5**, 11–25.

25 B. Buchroithner, S. Mayr, F. Hauser, E. Priglinger, H. Stangl, A. R. Santa-Maria, M. A. Deli, A. Der, T. A. Klar, M. Axmann, D. Sivun, M. Mairhofer and J. Jacak, *ACS Nano*, 2021, **15**, 2984–2993.

26 C. T. Lee, R. M. Bendriem, W. W. Wu and R. F. Shen, *J. Biomed. Sci.*, 2017, **24**, 1–12.

27 T. Eisemann, B. Costa, J. Strelau, M. Mittelbronn, P. Angel and H. Peterziel, *BMC Cancer*, 2018, **18**, 103.

28 S. Dauth, B. M. Maoz, S. P. Sheehy, M. A. Hemphill, T. Murty, M. K. Macedonia, A. M. Greer, B. Budnik and K. K. Parker, *J. Neurophysiol.*, 2017, **117**, 1320–1341.

29 M. E. J. Obien, K. Deligkaris, T. Bullmann, D. J. Bakkum and U. Frey, *Front. Neurosci.*, 2015, **8**, 423.

30 M. E. Spira and A. Hai, *Nat. Nanotechnol.*, 2013, **8**, 83–94.

31 K. Wallace, J. D. Strickland, P. Valdivia, W. R. Mundy and T. J. Shafer, *Neurotoxicology*, 2015, **49**, 79–85.

32 Y. Han, H. Li, Y. Lang, Y. Zhao, H. Sun, P. Zhang, X. Ma, J. Han, Q. Wang, J. Zhou and C. Wang, *Neurochem. Res.*, 2017, **42**, 1394–1402.

33 H.-G. Jahnke, D. Krinke, D. Seidel, K. Lilienthal, S. Schmidt, R. Azendorf, M. Fischer, T. Mack, F. Striggow, H. Althaus, A. Schober and A. A. Robitzki, *Biosens. Bioelectron.*, 2017, **88**, 78–84.

34 D. Lam, N. O. Fischer and H. A. Enright, *Curr. Opin. Pharmacol.*, 2021, **60**, 255–260.

35 Y. Demircan Yalcin, A. J. Bastiaens, J.-P. Frimat and R. Luttge, *J. Vac. Sci. Technol., B: Nanotechnol. Microelectron.: Mater., Process., Meas., Phenom.*, 2021, **39**, 064004.

36 G. Sánchez, E. Dalchiele and A. Bologna Alles, *J. Mater. Sci.*, 2006, **41**, 3241–3247.

37 D. Krinke, H.-G. Jahnke, O. Pänke and A. A. Robitzki, *Biosens. Bioelectron.*, 2009, **24**, 2798–2803.

38 I. I. Suni, *TrAC, Trends Anal. Chem.*, 2008, **27**, 604–611.

39 A. Abend, C. Steele, S. Schmidt, R. Frank, H.-G. Jahnke and M. Zink, *Int. J. Mol. Sci.*, 2020, **21**, 6249.

40 F. A. C. Azevedo, L. R. B. Carvalho, L. T. Grinberg, J. M. Farfel, R. E. L. Ferretti, R. E. P. Leite, W. J. Filho, R. Lent and S. Herculano-Houzel, *J. Comp. Neurol.*, 2009, **513**, 532–541.

41 A. Abend, C. Steele, H.-G. Jahnke and M. Zink, *Int. J. Mol. Sci.*, 2021, **22**, 8588.

42 J.-F. Gilles, M. Dos Santos, T. Boudier, S. Bolte and N. Heck, *Methods*, 2017, **115**, 55–64.

43 Z. Molnár, G. J. Clowry, N. Šestan, A. Alzu'bi, T. Bakken, R. F. Hevner, P. S. Hüppi, I. Kostović, P. Rakic, E. S. Anton, D. Edwards, P. Garcez, A. Hoerder-Suabedissen and A. Kriegstein, *J. Anat.*, 2019, **235**, 432–451.

44 K. Kawabata, E. Bagarinao, H. Watanabe, S. Maesawa, D. Mori, K. Hara, R. Ohdake, M. Masuda, A. Ogura, T. Kato,

S. Koyama, M. Katsuno, T. Wakabayashi, M. Kuzuya, M. Hoshiyama, H. Isoda, S. Naganawa, N. Ozaki and G. Sobue, *NeuroImage*, 2022, 119263.

45 V. M. Ravi, K. Joseph, J. Wurm, S. Behringer, N. Garrelfs, P. d' Errico, Y. Naseri, P. Franco, M. Meyer-Luehmann, R. Sankowski, M. J. Shah, I. Mader, D. Delev, M. Follo, J. Beck, O. Schnell, U. G. Hofmann and D. H. Heiland, *Life Sci. Alliance*, 2019, **2**, e201900305.

46 J. C. Er, C. Leong, C. L. Teoh, Q. Yuan, P. Merchant, M. Dunn, D. Sulzer, D. Sames, A. Bhinge, D. Kim, S.-M. Kim, M.-H. Yoon, L. W. Stanton, S. H. Je, S.-W. Yun and Y.-T. Chang, *Angew. Chem., Int. Ed.*, 2015, **54**, 2442–2446.

47 C. Marin and E. Fernándes, *Front. Neuroeng.*, 2010, **3**, 1–6.

48 R. Biran, D. C. Martin and P. A. Tresco, *Exp. Neurol.*, 2005, **195**, 115–126.

49 A. Golabchi, K. M. Woeppel, X. Li, C. F. Lagenaur and X. T. Cui, *Biosens. Bioelectron.*, 2020, **155**, 112096.

50 X. Yang, T. Zhou, T. J. Zwang, G. Hong, Y. Zhao, R. D. Viveros, T.-M. Fu, T. Gao and C. M. Lieber, *Nat. Mater.*, 2019, **18**, 510–517.

51 E. Azemi, C. F. Lagenaur and X. T. Cui, *Biomaterials*, 2011, **32**, 681–692.

52 T. D. Yoshida Kozai, N. B. Langhals, P. R. Patel, X. Deng, H. Zhang, K. L. Smith, J. Lahann, N. A. Kotov and D. R. Kipke, *Nat. Mater.*, 2012, **11**, 1065–1073.

53 F. Vitale, W. Shen, N. Driscoll, J. C. Burrell, A. G. Richardson, O. Adewole, B. Murphy, A. Ananthakrishnan, H. Oh, T. Wang, T. H. Lucas, D. K. Cullen, M. G. Allen and B. Litt, *PLoS One*, 2018, **13**, e0206137.

54 F. Idris, S. Hanna Muharram, Z. Zaini and S. Diah, *bioRxiv*, 2018, 435990.

55 H.-G. Jahnke, S. Schmidt, R. Frank, W. Weigel, C. Prönnecke and A. A. Robitzki, *Biosens. Bioelectron.*, 2019, **129**, 208–215.

56 T. Schmitz, M. Schweinlin, R. T. Kollhoff, L. Engelhardt, C. Lotz, F. Groeber-Becker, H. Walles, M. Metzger and J. Hansmann, *ACS Appl. Nano Mater.*, 2018, **1**, 2284–2293.

57 A. Jalava, K. Åkerman and J. Heikkilä, *J. Cell. Physiol.*, 1993, **155**, 301–312.

58 J. Schindelin, I. Arganda-Carreras, E. Frise, V. Kaynig, M. Longair, T. Pietzsch, S. Preibisch, C. Rueden, S. Saalfeld, B. Schmid, J.-Y. Tinevez, D. J. White, V. Hartenstein, K. Eliceiri, P. Tomancak and A. Cardona, *Nat. Methods*, 2012, **9**, 676–682.

59 J. Schindelin, C. T. Rueden, M. C. Hiner and K. W. Eliceiri, *Mol. Reprod. Dev.*, 2015, **82**, 518–529.

60 D. R. Baker, M.-L. Sirbescu, V. Maneta, K. L. Webber and W. B. Simmons, *Can. Mineral.*, 2018, **56**, 625–643.

61 J. G. Berryman, *J. Appl. Phys.*, 1985, **57**, 2374–2384.

Supplementary Information

Neuronal and Glial Cell Co-culture Organization and Impedance Spectroscopy on Nanocolumnar TiN Films for Lab-on-a-Chip Devices

Alice Abend,[a] Chelsie Steele, [a] Sabine Schmidt,[b] Ronny Frank,[b] Heinz-Georg Jahnke ‡[b] and Mareike Zink ‡*[a]

[a] Research Group Biotechnology and Biomedicine, Peter Debye Institute for Soft Matter Physics, Leipzig University, 04103 Leipzig, Germany. E-mail: zink@physik.uni-leipzig.de

[b] Centre for Biotechnology and Biomedicine, Molecular Biological-Biochemical Processing Technology, Leipzig University, 04103 Leipzig, Germany.

‡These authors contributed equally to this work.
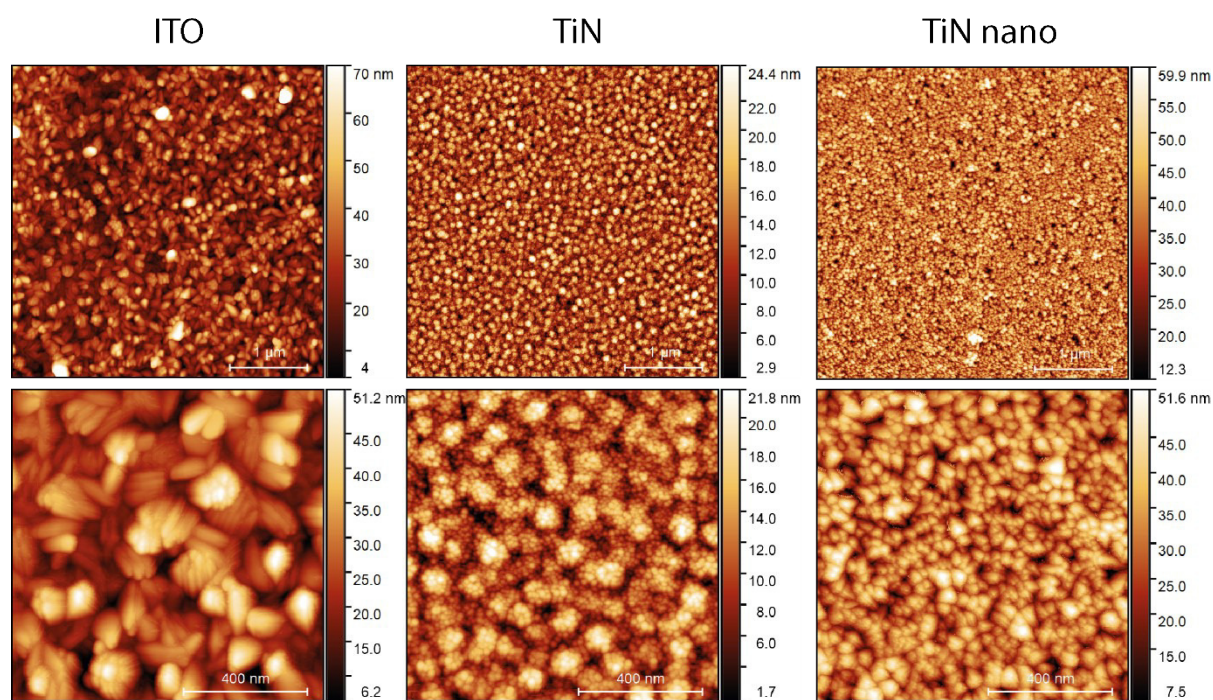
Figure S1: Atomic force microscopy-based topology characterization. The electrode materials indium tin oxide (ITO), titanium nitride (TiN), and titanium nitride with nanocolumnar structure (TiN nano) were imaged with a JPK NanoWizard 3 atomic force microscope in direct drive AC mode with a TESPAHAR cantilever (Bruker).

TiN nano   TiN   ITO

1 day

80:20

3 days

TiN nano   TiN   ITO

1 day

20:80

3 days
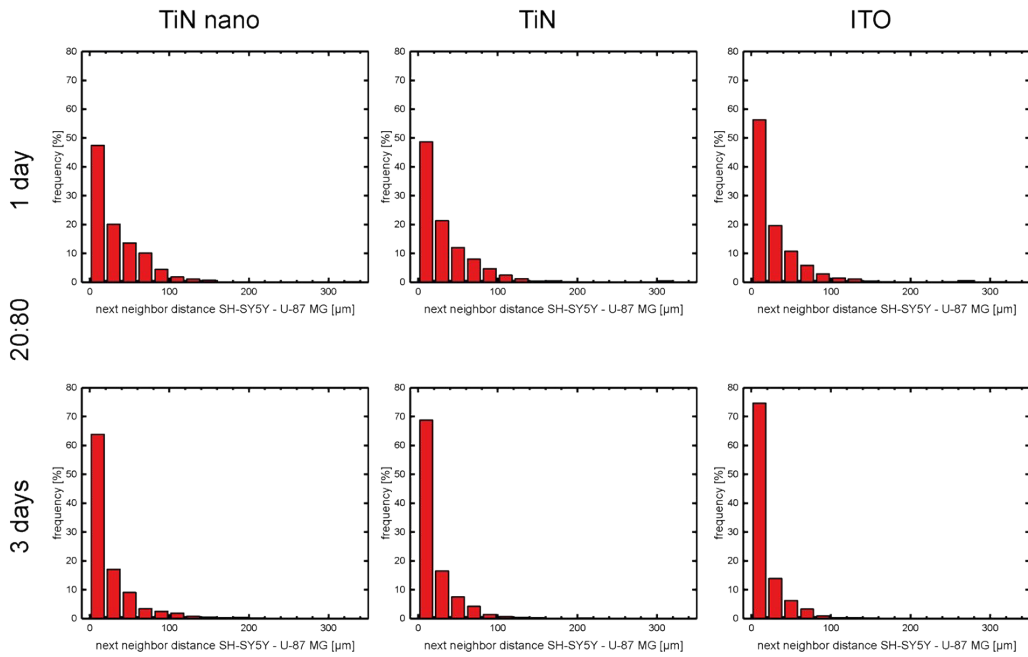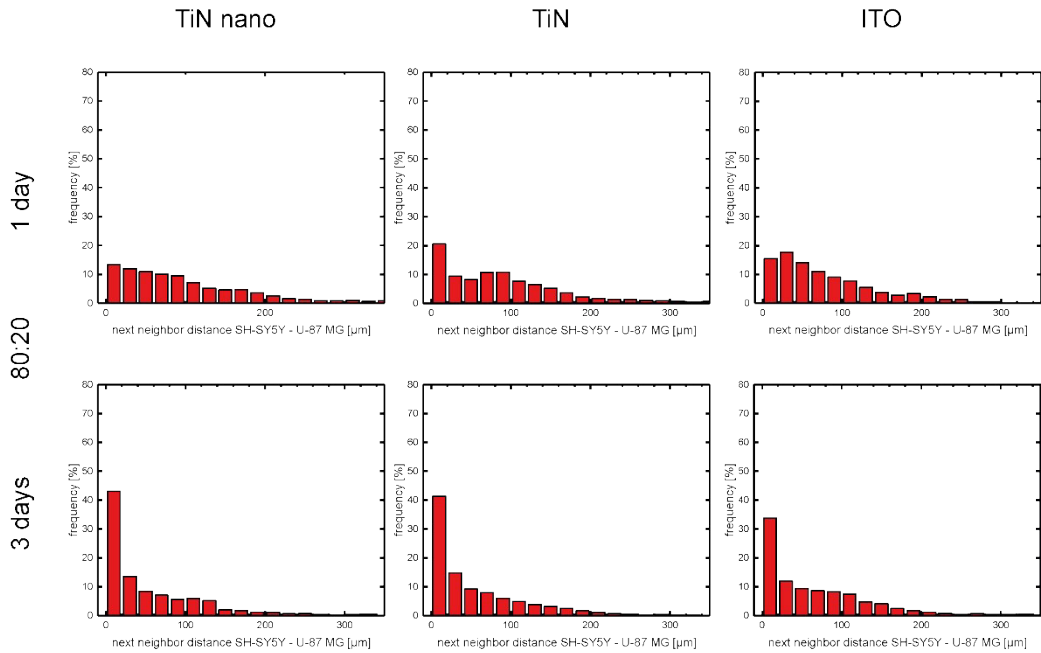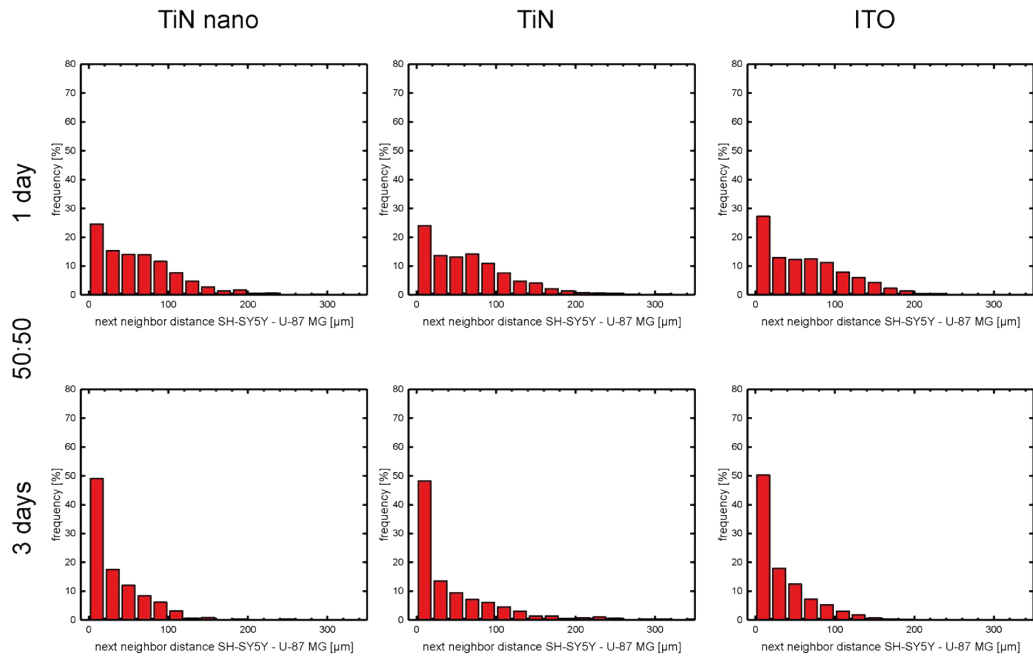
Figure S2: Histograms of center-to-center nearest neighbor distances of every neuronal cell to the next glial cell of the same data set. Cells were seeded at different ratios (80:20, 20:80, and 50:50) of SH-SY5Y to U-87 MG cells on electrode materials TiN nano, TiN, and ITO for either one or three days of culture time. Each graph represents the average of three individual samples (representing 54 experiments.
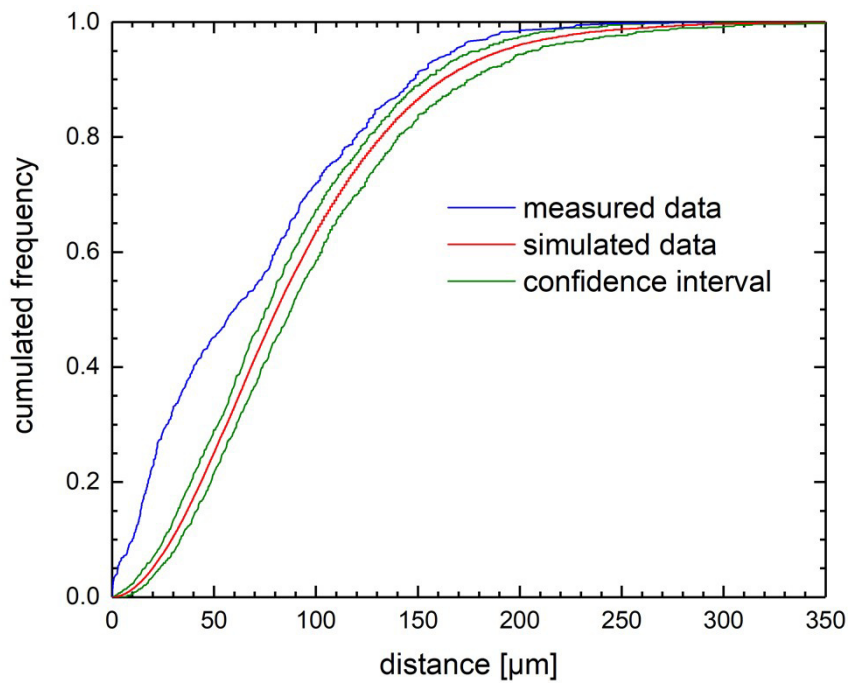
Figure S3: Cumulative distribution of center-to-center nearest neighbor distance of neuronal and glial cell nuclei. The blue curve represents the measured data, i.e. distance of nearest glial cell for every neuronal cell. We replaced the original data set of glial cell positions with 50 different simulated data sets of the same size while leaving the neuronal cell positions untouched and computed the distance of nearest glial cell for every neuronal cell (For more information about the methods see Gilles et al. [6]). The results are shown by the red curve and the 2.5 % and 97.5 % confidence interval in green. Our measured data curve is outside of the green confidence interval of randomized data meaning our results are statistically significant.
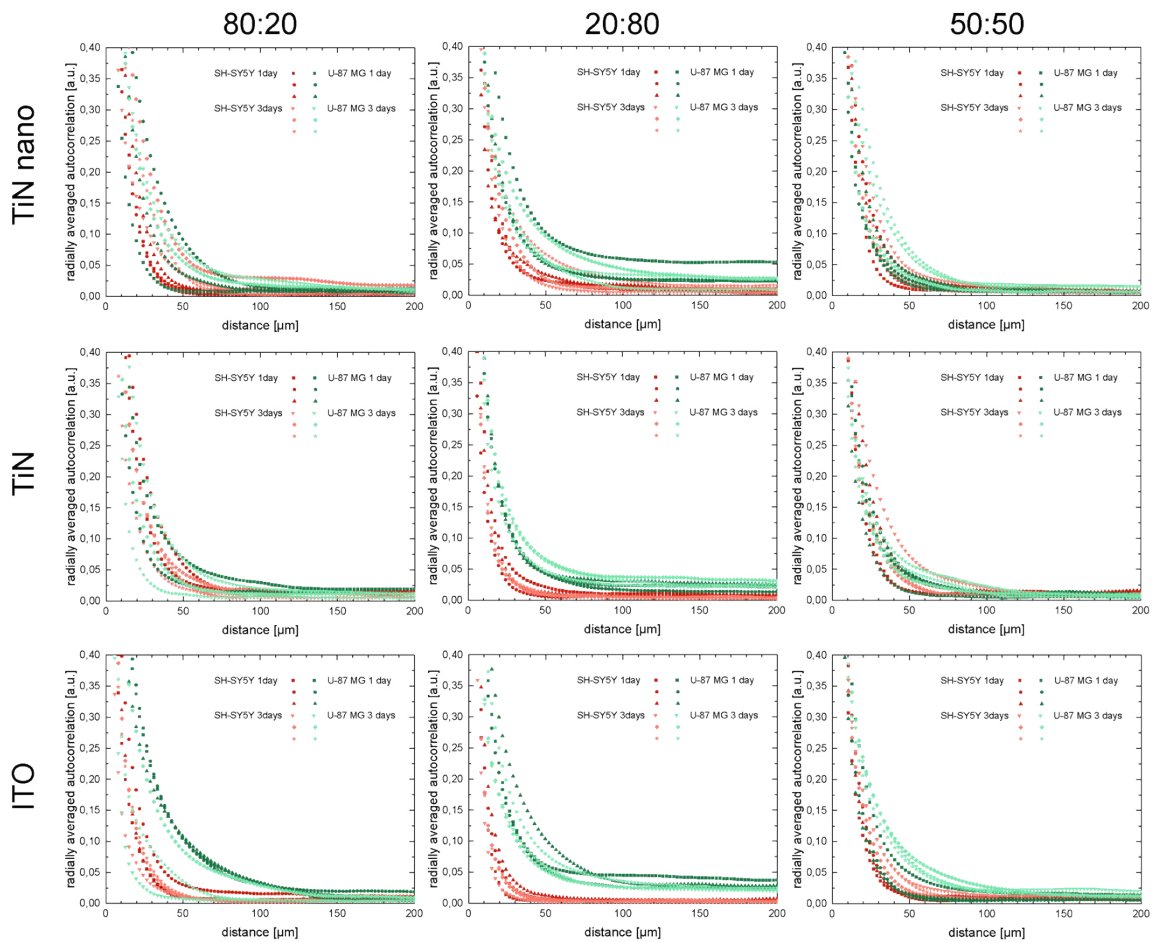
Figure S4: Radially averaged autocorrelation analysis for cell nuclei positions. Data were obtained from 54 electrode material samples (TiN nano, TiN, ITO) with varying seeding ratios of neuronal and glial cells (80:20, 20:80, and 50:50) and culture times (one day and three days). Autocorrelation curves of U-87 MG cells are shown in green and SH-SY5Y in red.

Image Analysis – Radial Autocorrelation Function:

In order to analyze the cellular network organization in terms of the nearest neighbors of each cell, the macro "Radially Averaged Autocorrelation" combined with the "Radial Profile" plugin was employed to evaluate a radially averaged two-point autocorrelation function S2 for all images as described in Abend et al.[1] Such analysis allows measurement of the average size of objects (patches of cell clusters) in conjunction with the distance between these objects as similarly shown by Baker et al. [2] and described in detail by Berryman et al.[3] Briefly, the ImageJ (Fiji distribution [4] based on ImageJ platform [5]) plugin computes the probability of finding a black pixel in increasing radial distance to an initially chosen black pixel. This process is repeated multiple times with different initial pixels. The results are radially averaged in a second step. The chosen plugin utilizes a fast Fourier transform (FFT) to reduce computation time, while simultaneously correcting for the periodicity of the FFT and finite image size, so the results do not suffer from artifacts. The results are normalized such that the value of the radially averaged autocorrelation function will always be 1 (perfect correlation) at a distance $r = 0$. It directly follows that an output value of 0 demonstrates the case of no correlation.

References

1   A. Abend, C. Steele, S. Schmidt, R. Frank, H.-G. Jahnke and M. Zink, *Int. J. Mol. Sci.*, 2020, **21**, 6249.

2   D. R. Baker, M.-L. Sirbescu, V. Maneta, K. L. Webber and W. B. Simmons, *Can. Mineral.*, 2018, **56**, 625–643.

3   J. G. Berryman, *J. Appl. Phys.*, 1985, **57**, 2374–2384.

4   J. Schindelin, I. Arganda-Carreras, E. Frise, V. Kaynig, M. Longair, T. Pietzsch, S. Preibisch, C. Rueden, S. Saalfeld, B. Schmid, J.-Y. Tinevez, D. J. White, V. Hartenstein, K. Eliceiri, P. Tomancak and A. Cardona, *Nat. Methods*, 2012, **9**, 676–682.

5   J. Schindelin, C. T. Rueden, M. C. Hiner and K. W. Eliceiri, *Mol. Reprod. Dev.*, 2015, **82**, 518–529.

6   J.-F. Gilles, M. Dos Santos, T. Boudier, S. Bolte and N. Heck, *Methods*, 2017, **115**, 55–64.

4. Summary and Conclusion

The goal of this thesis is to study the interaction of human neuronal and glial cells with different types of electrode materials such as gold, ITO, TiN, and TiN nano from a physicist's point of view. The analysis includes cellular network organization, cell distribution, adhesion, and proliferation in mono- as well as co-culture experiments with neuron-like SH-SY5Y and glia-like U-87 MG cells. Diverse techniques from physics, mathematics, biology, and computational science are used to find a new approach to analyzing bioactivity of the electrode substrates. The presented method relies on comparably fast, inexpensive, and straightforward laboratory experiments that seem basic but show their true potential once coupled with computational analysis techniques.

In the first presented study "Proliferation and Cluster Analysis of Neurons and Glial Cell Organization on Nanocolumnar TiN Substrates" [147], SH-SY5Y and U-87 MG cells are seeded onto electrode substrates in mono-culture and grown for either one or three days. Subsequently, cells are fixed and cell nuclei and actin fibers are fluorescently stained to detect cell positions in microscopy images and count cells.

The idea to use microscopy image analysis in the testing of biomaterials has been around for at least 30 years. Schreiber and Kinzl used the method already in 1991 to measure biocompatibility of biomaterials implanted in rats [150]. Their algorithm was used to identify certain cells in tissue. Results showed that the image-based method is superior to histological investigations since the findings were exactly reproducible. Small differences in biocompatibility were verifiable which other methods could not deliver at that time. Fast forward to 2010, Bratlie et al. already presented a method based on *in vivo* fluorescence imaging of mouse models that was able to measure inflammatory response to implanted biomaterials. Results were again validated through comparison with traditional histological analysis [151]. Using image analysis tools to investigate biocompatibility also *in vitro* is a step that comes fairly naturally to mind paying attention to the need to reduce the number of animal experiments. However, according to Uka et al., image analysis is not a "core capacity of a significant portion of biomaterial scientists" and mostly "ready-made tools" are used instead [152]. Additionally, the researchers reason that methods to investigate the performance and biocompatibility of biomaterials have not progressed as fast as the development of novel materials and modifications in their publication from 2021 [152]. This gap needs to be closed and the latency between the development of materials and appropriate testing methods reduced. Validation of a biomaterial's potential use in a device or lab-on-a-chip test bed is currently mainly based on the determination of its direct and indirect cytotoxic effects on specific cells [152]. However, other parameters such as cell shape and size, phenotype, and cellular secretions for example are tested during the development of novel biomaterials [152].

For the work of this thesis, straightforward fluorescence microscopy imaging is coupled with a combination of mathematical and physical methods such as the radially averaged autocorrelation function and a K-means machine learning algorithm. Together with cell proliferation data, this can be used as a quantitative tool to analyze biocompatibility of novel materials. The method is especially convenient for opaque biomaterials which are often used for medical implants. The usefulness of quantitative fluorescence imaging of cell populations for the assessment of biocompatibility has been demonstrated by Klußmann-Fricke et al. in 2021 [153]. Although the group only investigated cell proliferation and morphology instead of analyzing spatial cellular distribution on the substrates, this publication still supports my approach to the investigation of the interaction of neuron-like and glia-like cells earlier in 2020 [147].

In my publication, the autocorrelation function is used as a tool to quantify typical object size and distribution in the cell layer grown on electrode materials. The shape of the curve gives insight into cell growth patterns and cell agglomerations revealing mean object sizes and distances between them. Here, an object is either a single cell nucleus or an agglomeration of nuclei since this fluorescently labeled part of the cells has been used as a basis for image analysis. Additionally, a K-means algorithm is used to detect the size and position of cell clusters in the fluorescent images of cells. The whole spectrum of cellular growth patterns from homogeneously distributed cells to heterogeneous cell clusters can be mapped using the presented methods which deliver a unique fingerprint for each combination of electrode material and cell type. In conjunction with experimental data from different cellular growth times, the results can be used to make predictions on possible biocompatibility of the electrode substrates.

The radially averaged autocorrelation function looks roughly the same for U-87 MG cells grown on gold, ITO, TiN, and TiN nano representing the growth of fairly evenly spatially distributed glia cell agglomerations with little variation in object size indicated by the undulation of the curve for short culture times. Cells were mostly evenly distributed and only grew small agglomerations with longer culture time which is represented by the shift of the autocorrelation function to the right. The same behavior is also mirrored in the proliferation rates which are equal for all materials except for gold where cell growth is reduced. Autocorrelation functions of SH-SY5Y cells show much more variety between the substrate materials and growth times. Correlation length (transition point between steep slope and constant regime) shifts for all substrate types for longer culture times. This long-range correlation indicates the formation of cell clusters of various sizes. The undulating shape of the autocorrelation function that has been visible for short culture times is completely blurred by the existence of different-sized cell agglomerations. Especially large clusters are seen on TiN and TiN nano samples. Spatial distribution of SH-SY5Y cells was further investigated using a K-means algorithm that detects large cell agglomerations in the fluorescent images. It worked especially well and was reliable for large and dense cell clusters which were found on TiN and TiN nano samples.

However, the algorithm fails to identify small cell agglomerations as seen on gold and ITO and instead pools these data points into large but less dense clusters. This is essentially a mathematical artifact of the algorithm. In these cases, the radially averaged autocorrelation function is vital to back up the results from K-means. Together with proliferation data, K-means and the autocorrelation function provide a clear idea of variations in cellular growth on different biomaterials.

One possible explanation for the differences in cell growth on the different electrode materials could be the varying degree of their surface roughness. This parameter was measured using atomic force microscopy for the publication (see Figure 1 in [147]). Vallejo-Giraldo et al. reported that SH-SY5Y cells grew best on semi-rough (R_a = 19 nm) ITO surfaces [154]. Neuronal cells did not adhere well to very smooth (R_a = 1 nm) or especially rough (R_a = 81 nm) surfaces either. Additionally, Khan et al. drew similar conclusions while measuring the adhesion of rat cortical neurons on silicon wafers [155]. Cellular adhesion seems to increase with growing surface roughness until it reaches an optimum at a specific degree of roughness and then decreases for even coarser surfaces. In their study on neuronal cells cultured on patterned SiO_2 layers, Fan et al. found the cells to migrate to areas of optimal surface roughness [156]. Besides, Yoon et al. proved the superiority of nanostructured surfaces (i.e. carbon nanotubes) with regard to the expression of neuronal markers of differentiated SH-SY5Y cells and neural activity in MEAs in contrast with smoother graphene samples [157]. Experiments exhibited a lower differentiation-induced apoptotic rate and faster proliferation for nanostructured topographies. The group reasons that the improved performance of the samples does not originate from the material itself but rather from the surface structure. Gold and ITO exhibited the lowest and highest values respectively for root-mean-square roughness in my experiments and seem to provide the poorest growth conditions for the SH-SY5Y, and to some extend also for U-87 MG, cells. However, gold and TiN revealed very similar values for surface roughness and grain size but SH-SY5Y cells still grew quite differently on these two materials. This leads to the conclusion, that surface topography of the electrode samples cannot be the sole reason for differences in experimental outcome. Surface chemistry likely also determines cell behavior. Titanium nitride with nanocolumnar surface modification is found to deliver the most promising results concerning cell proliferation and network formation in this study.

The second paper "Adhesion of Neurons and Glial Cells with Nanocolumnar TiN Films for Brain-Machine Interfaces" [148], builds on the work of the first as it introduces the assessment of adhesion parameters of single cells into the framework of this thesis. Short-term adhesion dynamics and long-term cell spreading characteristics are assessed for neuron-like SH-SY5Y and glia-like U-87 MG cells on electrode materials. Cell adhesion is investigated using AFM-based single-cell force spectroscopy on short time scales of seconds. The maximum adhesion force exerted by single cells being detached from the substrates and the total work required to remove the individual cells is measured. Results were normalized to the cell-substrate contact area since the adhesion force usually scales with the number of

adhesion points and therewith likely correlates with the contact area [109]. Generally, larger adhesion force values were measured for all cells and substrate materials for longer contact times (30 s vs. 5 s) as expected [113]. The lowest adhesion force was found for measurements with gold substrates for both SH-SY5Y and U-87 MG cells. This is in line with findings from my first publication [147], where low proliferation rates were observed on gold substrates. Poor cell adhesion could contribute to reduced cell proliferation in these samples. The distribution of measured values is generally broader for U-87 MG cells in comparison with SH-SY5Y cells. Variability of measured cell adhesion forces could originate from differences in cell cycle phases as previously reported by Panagiotakopoulou et al. [158] and Lock et al. [159]. However, Dao et al. argue that these variations are neither associated with cell cycle phases nor do they stem from a change in adhesion behavior of cells after repetitive detachment experiments [160]. The reason could simply be cell-to-cell variation. This is exactly why single-cell measurements are needed to complement ensemble measurements. Unfortunately, the time scale of single-cell force spectroscopy was limited in my experiments since longer adhesion times resulted in exceeding the measurable force range and cells could not be completely detached from the substrate. The limiting factor here is the z-range of the piezo crystal which is 100 µm. The increase in binding strength for contact times above 30 s could be attributed to the formation of specific binding formations. Nascent adhesions and focal complexes are formed by the cells on a time scale of tens of seconds. These early adhesions mature later into focal adhesion points [99,101–104].

Due to the technical limitations and the associated impaired range of single-cell force spectroscopy measurements, judging optimal biocompatibility of electrode materials with regard to cell adhesion aspects is challenging. Defining what "good adhesion" means depends on the cell type and intended use of the biomaterial. For example, delicate cellular adhesion can be an advantage in the case of neurons [161,162]. Hence, additionally to the AFM experiments, I carried out measurements on long-term cell spreading behavior for the publication [148] to gain more insight into the possible correlations between short-term adhesion and long-term cell-surface interactions. To this end, fluorescence microscopy images of cells stained for actin fibers and cell nuclei are used to analyze cell spreading on time scales of days. Here, the same treatment procedure from the first publication [147] for cell-electrode substrate samples is used. In fact, the same samples, or more specifically the fluorescence imaging data from the first paper [147] are employed. Adding cell spreading analysis to the already proven mathematical tools gives rise to the possibility to draw even more results from one and the same, and admittedly rather simple, data set. Findings include that U-87 MG cells did not spread anymore on the substrates after one day of culture time. SH-SY5Y cells did not only spread more than their glial cell counterpart but they also spread differently depending on the electrode material substrate type. Cell area of SH-SY5Y grew the most on TiN and TiN nano samples after three days of culture time. Also, morphological changes in the cells are apparent in these two materials in comparison to gold and ITO. Cells show many more and much longer protrusions (see Figure 4 in [148]) if they are grown on

92

TiN or TiN nano for longer culture times. These neurites mainly account for the surface area increase as the cell bodies stayed roughly the same size.

In addition to the investigation of cellular behavior on different time scales, the publication [148] merges single-cell experiments with ensemble measurements. Both are important to fully understand the interaction of cells with substrate materials. Single-cell experiments give insight into cellular heterogeneity and represent variability in the response of individual cells to stimuli such as detachment from the substrate material with an AFM. Ensemble measurements of multiple cells simultaneously on the other hand, like culturing SH-SY5Y and U-87 MG cells on electrode substrates, provide a population average. They can reveal patterns or trends that might not be evident on the single-cell level.

In the third presented study "Neuronal and glial cell co-culture organization and impedance spectroscopy on nanocolumnar TiN films for lab-on-a-chip devices" [149], co-culture experiments with both SH-SY5Y and U-87 MG cells are introduced. This expands the work of the first two studies [147,148] toward more physiological cell culture conditions. Co-culture experiments enable a better understanding of the interplay between the individual cell types. Neurons and glial cells not only coexist in the human brain under physiologic conditions but also communicate closely and interact frequently. This interconnection is explored in the publication using the fluorescence microscopy-based experimental approach introduced in the first study [147]. SH-SY5Y and U-87 MG cells are seeded at three different neuron-to-glia ratios on the electrode material substrates (TiN, TiN nano, and ITO) and are subsequently fluorescently stained and imaged after either one or three days of culture. Cell ratios are chosen based on the real physiologic composition of different parts of the human brain as described by Azevedo et al. [2]. Cells were co-cultured with three different neuron-glia ratios: 50:50, 80:20, and 20:80 for the presented study. On average, human brains consist of roughly 50 % neurons and 50 % non-neuronal cells. The cerebellum contains the highest number of neurons in the human brain which results in a ratio of 80 % neurons and 20 % non-neurons. On the other hand, the cerebral cortex (grey and white matter combined) consists of roughly 20 % neurons and 80 % non-neurons. Cell ratios were chosen in this study to simulate cell growth for different areas of the brain with different characteristics.

Two-channel fluorescence microscopy reveals striking differences in the growth patterns and cellular distribution of the cell lines under mono- and co-culture conditions. Analysis of the distribution of cells is performed using the radially averaged autocorrelation approach coupled with a nearest-neighbor analysis. For the latter, the distance to the nearest neighbor cell is computed for each cell on a substrate. In this study, cells grown at a 20:80 and 50:50 neuron-glia-ratio tend to generally sit closer to cells of the complementary type instead of their own cell type resulting in fairly homogenously spatial cell distributions. However, the opposite is true for samples with 80 % SH-SY5Y and 20 % U-87 MG cells. For these experiments, neuron-like cells tend to sit closer to other neuron-like cells than glia-like cells. These findings are in line with examinations of *in vivo* brain architecture. For example, Ravi

et al. showed a homogeneous distribution of neurons and astrocytes (labeled with NeuN and GFAP) in healthy human cerebral cortex (20:80 neuron-glia-ratio) [163]. On the other hand, immunostained mouse brain slices of the cerebellum (80:20 neuron-glia ratio) presented by Er et al. show a homogenous distribution of GFAP-positive astrocytes surrounded by a NeuN-positive layer of neurons [164]. In conclusion, comparison of data generated by my co-culture experiments with the referenced publications reveals the possibility to imitate physiologic brain structures *in vitro* to some extent. The presented computer-based methods enable quantification of the cell structures.

Co-cultured SH-SY5Y do not tend to grow in huge agglomerations as seen in the mono-culture study [147]. Hence, the K-means clustering algorithm is not suitable for this kind of data. However, uniformly growing cell ensembles could be beneficial for implantation applications of the electrode materials. Yang et al. already demonstrated a bio-inspired neural probe that resulted in fairly homogeneously distributed neurons and astrocytes upon implantation into mouse brains [165]. No obvious depletion of neurons or accumulation of astrocytes at the implantation site was visible. All experimental parameters such as culture time, culture medium, and electrode substrate materials are the same for the earlier mono-culture experiments [147,148] and this co-culture study [149]. Since the only difference, except for fluorescent labeling reagents applied after fixation, is the fact that both cell types are cultured together, I conclude that the direct interaction of SH-SY5Y and U-87 MG cells is responsible for the vastly different cell growth patterns. Actually, this is backed up by other studies such as by Idris et al. where researchers found that only direct contact of cells could mimic *in vivo* blood-brain barrier conditions in an *in vitro* co-culture model [166].

The last part of the third presented study [149] incorporates electrochemical impedance spectroscopy measurements enabling the electrode materials "to be viewed in action" rounding off the study on biocompatibility. In addition to the investigation of cell adhesion and growth patterns of neuronal and glial cells on the electrode substrates, the performance of the electrode materials incorporated into multielectrode arrays is crucial. MEAs fabricated with novel materials need to be tested in electrochemical experiments before incorporating them into *in vitro* or *in vivo* applications. Electrochemical impedance spectroscopy is used to investigate the efficacy of indium tin oxide and titanium nitride with nanocolumnar surface modification in MEAs with several different electrode sizes and both cell types either in mono- or in co-culture. Here, TiN nano performs superior to ITO in terms of measured relative impedance values and signal-to-noise ratio on all electrode sizes. TiN nano reveals a consistently lowered self-impedance over a wide frequency range which is beneficial for the miniaturization of the electrodes in MEAs. Electrode arrays can be fabricated denser which increases the spatial measurement resolution of the device.

In summary, the here presented studies propose a new approach to investigate the biocompatibility of materials while placing emphasis on mathematical methods and

94

computational science. The concept is complemented and supported by tried and true cellular experimental techniques. It can be used to make the interaction of neuronal cells with electrode materials measurable and more particularly enables comparisons between different materials and cell types.

5. Outlook

The here presented study on the interaction of electrode materials with neuronal and glial cells is two-fold. First, the interplay between neuron-like SH-SY5Y and glia-like U-87 MG cells and the electrode materials gold, ITO, TiN, and TiN nano is evaluated using proliferation and cell adhesion experiments. Secondly, and perhaps more importantly, in the course thereof, a new image-based strategy to assess biocompatibility is developed that expands biomaterial scientists' toolkits of *in vitro* analysis methods. However, as usual in science, investigating problems and developing new techniques give rise to even more questions that need to be answered.

A question that easily comes to mind having completed the research for this thesis involves the issue of cell lines vs. primary cells. Using cell lines facilitates experiments and the development of new analysis methods because they are usually well-studied, and results can be compared to a lot of other researchers' work. Another advantage of cell lines is their facilitated usability for the scientist concerning cell culture in comparison with primary cells. However, the latter needs to be introduced into the experimental work at some point to gain more physiologic *in vitro* culture conditions. Cell lines might lack some crucial *in vivo* aspects [167]. Therefore, incorporating primary cells would be the logical next step for the work on the presented issues in this thesis. The behavior and growth of primary neurons and glial cells on multielectrode arrays made from TiN with nanocolumnar surface modification should be investigated.

The presented algorithms including K-means clustering, radially averaged autocorrelation function and nearest neighbor analysis could not only be applied to data sets of primary neuronal cells but should also be tested on completely different cell types. Cluster analysis or spatial autocorrelation might not be applicable to mono-cultured epithelial cells since this type usually grows in continuous layers anyway. However, nearest neighbor analysis coupled with measurements on cell contour [168] could prove useful for these epithelial cultures. On the other hand, analysis of *in vitro* co-cultures of different types of epithelial cells could still benefit from the K-means approach. Generally, the presented image-based computational approach to quantify biocompatibility is applicable to cell types other than neuronal but adjustments would need to be made to tailor the analysis method according to specific cellular requirements.

Scaling the proposed methods for experiments involving three or more different cell types is also expected to work as long as cell types can be distinguished using fluorescent labeling. Data sets from several different co-cultured cell types are separated during image processing anyway and K-means as well as the autocorrelation function run on these individual data sets. Nearest-neighbor analysis would take more effort and look more complicated. Distances of cells could still be treated as a pair-wise interaction but while two cell types (A and B) result in a single

neighbor pair (A-B is the same as B-A), three different cell types (A, B, and C) already lead to three neighbor pairs (A-B, A-C, and B-C). Hence, scaling of the nearest neighbor method for more diverse cell cultures might result in much longer computation time unless parallelization of computing is implemented.

As shown in this study, unsupervised self-learning algorithms are bound to encounter some limits in their usability. Here, the algorithm proved useful to detect large cell clusters but failed to identify small cell agglomerations. It would be interesting to see where the line is drawn between these two cases and how self-learning algorithms can be improved to deliver high-quality results on a broader range of spatial cell distribution patterns. The specification of the number of clusters in a data set coupled with the random selection of initial cluster centers could be problematic for very large data sets. Also, using the Euclidian norm as a metric for cell distances inevitably leads to the algorithm's preference for spherical clusters. Other cluster shapes are more difficult to detect without adding modifications to K-means. The experiments for the presented thesis reveal good K-means results for large and overlapping cell clusters but the method fails to detect smaller non-overlapping agglomerations. This is a common feature of K-means [169]. Moreover, the success of K-means scales with the number of clusters. More clusters lead to more errors during initialization and iterations [170]. That is one of the main reasons for K-means to fail for small agglomerations of U-87 MG cells that are located far apart on the substrates. Published work by Fränti et al. and more recently by Ikotun et al. propose possible solutions to some of the problems associated with K-means [170,171]. K-means results depend strongly on the initialization process of centroids. Once the cluster centers are set, they can only move locally but not globally during iterations of the algorithm. Hence, optimization of the initialization process would help to improve the overall clustering results. Otherwise, there is a possibility to get stuck in an inferior local minimum [170]. Another way to improve K-means results could be to restart the algorithm several times with different sets of initialized centroids and simply keep the best result [172]. That approach usually extends computation time. Finally, a possible path to the improvement of the algorithms could be the simulation of various types of cell growth and the fabrication of data sets to test modifications to the K-means code. Findings could be published in a program library where common cell types and distributions are mapped to specific versions of K-means algorithms. That would generally enable more researchers to use these methods, and perhaps more importantly, could make computational science techniques readily accessible for scientist with a background in biology instead of mathematics or physics.

Publication List – Author Contribution

<u>Alice Abend</u>, Chelsie Steele, Sabine Schmidt, Ronny Frank, Heinz-Georg Jahnke, and Mareike Zink. "Proliferation and Cluster Analysis of Neurons and Glial Cell Organization on Nanocolumnar TiN Substrates", *Int. J. Mol. Sci.* 2020.

Impact Factor Int. J. Mol. Sci. (2022): 6.208

Author contributions as declared in the publication [147]: Conceptualization, M.Z.; <u>methodology, A.A.</u>, C.S., R.F. and H.-G.J.; software, C.S.; <u>validation, A.A.</u>, C.S., H.-G.J. and M.Z.; <u>formal analysis, A.A.</u>, C.S. and R.F.; resources, S.S., H.-G.J. and M.Z.; <u>data curation, A.A.</u>, C.S., H.-G.J. and M.Z.; <u>writing—original draft preparation, A.A.</u>, H.-G.-J. and M.Z.; <u>writing—review and editing, A.A.</u>, C.S., H.-G.J. and M.Z.; <u>visualization, A.A.</u>; supervision, H.-G.J. and M.Z.; project administration, M.Z. and H.-G.J.; funding acquisition, M.Z. and H.-G.J.

I performed all cell experiments including fluorescence staining and the acquisition of fluorescence microscopy images. I did the cell proliferation analysis including data interpretation and the major part of data processing and interpretation of the radial autocorrelation method. C.S. contributed significantly to K-means data acquisition and I performed data processing and interpretation on clustering. I wrote the manuscript except for the paragraph in the results section on electrode material surface topography (2.1.) which was contributed by H.-G.J. and modified by me. I produced the graphics in the manuscript.

<u>Alice Abend</u>, Chelsie Steele, Heinz-Georg Jahnke, and Mareike Zink. "Adhesion of Neurons and Glial Cells with Nanocolumnar TiN Films for Brain-Machine Interfaces", *Int. J. Mol. Sci.* 2021.

Author contributions as declared in the publication [148]: Conceptualization, M.Z.; <u>methodology, A.A.</u>, M.Z. and H.-G.J.; software, C.S.; <u>validation, A.A.</u>, C.S., H.-G.J. and M.Z.; <u>formal analysis, A.A.</u> and C.S.; resources, H.-G.J. and M.Z.; <u>data curation, A.A.</u> and C.S.; <u>writing—original draft preparation, A.A.</u> and M.Z.; <u>writing—review and editing, A.A.</u>, C.S., H.-G.J. and M.Z.; <u>visualization, A.A.</u>; supervision, M.Z. and H.-G.J.; project administration, M.Z. and H.-G.J.; funding acquisition, M.Z. and H.-G.J.

I performed all experiments for single-cell force spectroscopy with the Cell Hesion AFM. I did the analysis and data interpretation on adhesion forces and detachment work. I performed the experiments including fluorescence staining and the acquisition of fluorescence microscopy images that were necessary for the cell spreading analysis. C.S. contributed to the cell spreading data acquisition and I performed data processing and interpretation on cell spreading. I wrote the manuscript and produced the graphics in the manuscript.

Alice Abend, Chelsie Steele, Sabine Schmidt, Ronny Frank, Heinz-Georg Jahnke, and Mareike Zink. „Neuronal and glial cell co-culture organization and impedance spectroscopy on nanocolumnar TiN films for lab-on-a-chip devices", *Biomater. Sci.* 2022.

Author contributions as declared in the publication [149]: Conceptualization, M. Z.; methodology, A. A., C. S., and H.-G. J.; software, A. A. and C. S.; validation, A. A., C. S., H.-G. J. and M. Z.; formal analysis, A. A., C. S., and R. F.; resources, S. S., H.-G. J. and M. Z.; data curation, A. A., C. S., H.-G. J., and M. Z.; writing—original draft preparation, A. A., and M. Z.; writing, review and editing, A. A., C. S., H.-G. J. and M. Z.; visualization, A.A.; supervision, M. Z.; project administration, M. Z. and H.-G. J.; funding acquisition, M. Z., and H.-G. J.

I developed the co-culturing idea including chosen cell ratios and the associated laboratory protocol for fluorescence labeling of two cell types in one culture. C.S. contributed to fluorescent staining and performed image acquisition. I did the cell proliferation analysis including data interpretation and the major part of data processing and interpretation of the radial autocorrelation method. I did the nearest neighbor analysis and data interpretation. I prepared MEAs with cells for electrochemical impedance spectroscopy which was then performed by H.-G.J. I wrote the manuscript and produced the graphics in the manuscript.

List of Abbreviations

AFM   Atomic Force Microscopy

Au   Gold

ECM   Extracellular Matrix

ITO   Indium Tin Oxide

MEA   Multielectrode Array

SNR   Signal-to-Noise Ratio

TiN   Titanium Nitride

TiN nano   Nanocolumnar Titanium Nitride

SNR   Signal-to-Noise Ratio

List of Figures

Bibliography

1. von Bartheld, C.S.; Bahney, J.; Herculano-Houzel, S. The search for true numbers of neurons and glial cells in the human brain: A review of 150 years of cell counting. *J. Comp. Neurol.* **2016**, *524*, 3865–3895, doi:10.1002/cne.24040.

2. Azevedo, F.A.C.; Carvalho, L.R.B.; Grinberg, L.T.; Farfel, J.M.; Ferretti, R.E.L.; Leite, R.E.P.; Filho, W.J.; Lent, R.; Herculano-Houzel, S. Equal numbers of neuronal and nonneuronal cells make the human brain an isometrically scaled-up primate brain. *J. Comp. Neurol.* **2009**, *513*, 532–541, doi:10.1002/cne.21974.

3. Dugger, B.N.; Dickson, D.W. Pathology of Neurodegenerative Diseases. *Cold Spring Harb. Perspect. Biol.* **2017**, *9*, a028035, doi:10.1101/cshperspect.a028035.

4. Feigin, V.L.; Vos, T.; Nichols, E.; Owolabi, M.O.; Carroll, W.M.; Dichgans, M.; Deuschl, G.; Parmar, P.; Brainin, M.; Murray, C. The global burden of neurological disorders: translating evidence into policy. *Lancet Neurol.* **2020**, *19*, 255–265, doi:10.1016/S1474-4422(19)30411-9.

5. Hou, Y.; Dan, X.; Babbar, M.; Wei, Y.; Hasselbalch, S.G.; Croteau, D.L.; Bohr, V.A. Ageing as a risk factor for neurodegenerative disease. *Nat. Rev. Neurol.* **2019**, *15*, 565–581, doi:10.1038/s41582-019-0244-7.

6. Heemels, M.-T. Neurodegenerative diseases. *Nature* **2016**, *539*, 179–179, doi:10.1038/539179a.

7. Béjot, Y.; Yaffe, K. Ageing Population: A Neurological Challenge. *Neuroepidemiology* **2019**, *52*, 76–77, doi:10.1159/000495813.

8. Wyss-Coray, T. Ageing, neurodegeneration and brain rejuvenation. *Nature* **2016**, *539*, 180–186, doi:10.1038/nature20411.

9. Ferri, C.P.; Prince, M.; Brayne, C.; Brodaty, H.; Fratiglioni, L.; Ganguli, M.; Hall, K.; Hasegawa, K.; Hendrie, H.; Huang, Y.; et al. Global prevalence of dementia: a Delphi consensus study. *Lancet* **2005**, *366*, 2112–2117, doi:10.1016/S0140-6736(05)67889-0.

10. Calabrese, V.P.; Dorsey, E.. R.; Constantinescu, R..; Thompson, J.. P.; Biglan, K.. M.; Holloway, R.. G.; Kieburtz, K..; Marshall, F.. J.; Ravina, B.. M.; Schifitto, G..; et al. Projected Number of People with Parkinson Disease in the most Populous Nations, 2005 through 2030. *Neurology* **2007**, *69*, 223–224, doi:10.1212/01.wnl.0000271777.50910.73.

11. Erkkinen, M.G.; Kim, M.-O.; Geschwind, M.D. Clinical Neurology and Epidemiology of the Major Neurodegenerative Diseases. *Cold Spring Harb. Perspect. Biol.* **2018**, *10*, a033118, doi:10.1101/cshperspect.a033118.

12. Lamptey, R.N.L.; Chaulagain, B.; Trivedi, R.; Gothwal, A.; Layek, B.; Singh, J. A Review of the Common Neurodegenerative Disorders: Current Therapeutic Approaches and the Potential Role of Nanotherapeutics. *Int. J. Mol. Sci.* **2022**, *23*, 1851, doi:10.3390/ijms23031851.

13. La Cognata, V.; Morello, G.; Cavallaro, S. Omics Data and Their Integrative Analysis to Support Stratified Medicine in Neurodegenerative Diseases. *Int. J. Mol. Sci.* **2021**, *22*, 4820, doi:10.3390/ijms22094820.

14. Wingo, T.S.; Liu, Y.; Gerasimov, E.S.; Vattathil, S.M.; Wynne, M.E.; Liu, J.; Lori, A.; Faundez, V.; Bennett, D.A.; Seyfried, N.T.; et al. Shared mechanisms across the major psychiatric and neurodegenerative diseases. *Nat. Commun.* **2022**, *13*, 4314, doi:10.1038/s41467-022-31873-5.

15. Dressman, D.; Elyaman, W. T Cells: A Growing Universe of Roles in Neurodegenerative Diseases. *Neurosci.* **2022**, *28*, 335–348, doi:10.1177/10738584211024907.

16. Young, A.B. Four Decades of Neurodegenerative Disease Research: How Far We Have Come! *J. Neurosci.* **2009**, *29*, 12722–12728, doi:10.1523/JNEUROSCI.3767-09.2009.

17. Nikolakopoulou, P.; Rauti, R.; Voulgaris, D.; Shlomy, I.; Maoz, B.M.; Herland, A. Recent progress in translational engineered in vitro models of the central nervous system. *Brain* **2020**, *143*, 3181–3213, doi:10.1093/brain/awaa268.

18. Peng, H.; Xie, P.; Liu, L.; Kuang, X.; Wang, Y.; Qu, L.; Gong, H.; Jiang, S.; Li, A.; Ruan, Z.; et al. Morphological diversity of single neurons in molecularly defined cell types. *Nature* **2021**, *598*, 174–181, doi:10.1038/s41586-021-03941-1.

19. Brofiga, M.; Massobrio, P. Brain-on-a-Chip: Dream or Reality? *Front. Neurosci.* **2022**, *16*, 1–5, doi:10.3389/fnins.2022.837623.

20. Slanzi, A.; Iannoto, G.; Rossi, B.; Zenaro, E.; Constantin, G. In vitro Models of Neurodegenerative Diseases. *Front. Cell Dev. Biol.* **2020**, *8*, 328, doi:10.3389/fcell.2020.00328.

21. Schlachetzki, J.C.M.; Saliba, S.W.; Oliveira, A.C.P. de Studying neurodegenerative diseases in culture models. *Rev. Bras. Psiquiatr.* **2013**, *35*, S92–S100, doi:10.1590/1516-4446-2013-1159.

22. Alaylioglu, M.; Dursun, E.; Yilmazer, S.; Gezen-Ak, D. A Bridge Between in vitro and in vivo Studies in Neuroscience: Organotypic Brain Slice Cultures. *Arch. Neuropsychiatry* **2020**, *57*, 333–337, doi:10.29399/npa.26139.

23. Belle, A.M.; Enright, H.A.; Sales, A.P.; Kulp, K.; Osburn, J.; Kuhn, E.A.; Fischer, N.O.; Wheeler, E.K. Evaluation of in vitro neuronal platforms as surrogates for in vivo whole brain systems. *Sci. Rep.* **2018**, *8*, 10820, doi:10.1038/s41598-018-28950-5.

24. Perlmutter, J.S.; Mink, J.W. Deep Brain Stimulation. *Annu. Rev. Neurosci.* **2006**, *29*, 229–257, doi:10.1146/annurev.neuro.29.051605.112824.

25. Marin, C. Biocompatibility of intracortical microelectrodes: current status and future prospects. *Front. Neuroengineering* **2010**, *3*, 1–6, doi:10.3389/fneng.2010.00008.

26. Zhang, A.; Lieber, C.M. Nano-Bioelectronics. *Chem. Rev.* **2016**, *116*, 215–257, doi:10.1021/acs.chemrev.5b00608.

27. Keogh, C. Optimizing the neuron-electrode interface for chronic bioelectronic interfacing. *Neurosurg. Focus* **2020**, *49*, E7, doi:10.3171/2020.4.FOCUS20178.

28. Hejazi, M.; Tong, W.; Ibbotson, M.R.; Prawer, S.; Garrett, D.J. Advances in Carbon-Based Microfiber Electrodes for Neural Interfacing. *Front. Neurosci.* **2021**, *15*, doi:10.3389/fnins.2021.658703.

29. Yang, L.; Lee, K.; Villagracia, J.; Masmanidis, S.C. Open source silicon microprobes for high throughput neural recording. *J. Neural Eng.* **2020**, *17*, 016036, doi:10.1088/1741-2552/ab581a.

30. Domínguez-Bajo, A.; Rosa, J.M.; González-Mayorga, A.; Rodilla, B.L.; Arché-Núñez, A.;
104

Benayas, E.; Ocón, P.; Pérez, L.; Camarero, J.; Miranda, R.; et al. Nanostructured gold electrodes promote neural maturation and network connectivity. *Biomaterials* **2021**, *279*, 121186, doi:10.1016/j.biomaterials.2021.121186.

31. Carnicer-Lombarte, A.; Lancashire, H.T.; Vanhoestenberghe, A. In vitro biocompatibility and electrical stability of thick-film platinum/gold alloy electrodes printed on alumina. *J. Neural Eng.* **2017**, *14*, 036012, doi:10.1088/1741-2552/aa6557.

32. Geninatti, T.; Bruno, G.; Barile, B.; Hood, R.L.; Farina, M.; Schmulen, J.; Canavese, G.; Grattoni, A. Impedance characterization, degradation, and in vitro biocompatibility for platinum electrodes on BioMEMS. *Biomed. Microdevices* **2015**, *17*, 24, doi:10.1007/s10544-014-9909-6.

33. Kim, M.-H.; Park, M.; Kang, K.; Choi, I.S. Neurons on nanometric topographies: insights into neuronal behaviors in vitro. *Biomater. Sci.* **2014**, *2*, 148–155, doi:10.1039/C3BM60255A.

34. Craighead, H.G.; James, C.D.; Turner, A.M.P. Chemical and topographical patterning for directed cell attachment. *Curr. Opin. Solid State Mater. Sci.* **2001**, *5*, 177–184, doi:10.1016/S1359-0286(01)00005-5.

35. Goldner, J.S.; Bruder, J.M.; Li, G.; Gazzola, D.; Hoffman-Kim, D. Neurite bridging across micropatterned grooves. *Biomaterials* **2006**, *27*, 460–472, doi:10.1016/j.biomaterials.2005.06.035.

36. Dowell-Mesfin, N.M.; Abdul-Karim, M.-A.; Turner, A.M.P.; Schanz, S.; Craighead, H.G.; Roysam, B.; Turner, J.N.; Shain, W. Topographically modified surfaces affect orientation and growth of hippocampal neurons. *J. Neural Eng.* **2004**, *1*, 78–90, doi:10.1088/1741-2560/1/2/003.

37. Brunetti, V.; Maiorano, G.; Rizzello, L.; Sorce, B.; Sabella, S.; Cingolani, R.; Pompa, P.P. Neurons sense nanoscale roughness with nanometer sensitivity. *Proc. Natl. Acad. Sci.* **2010**, *107*, 6264–6269, doi:10.1073/pnas.0914456107.

38. Li, Z.; Persson, H.; Adolfsson, K.; Oredsson, S.; Prinz, C.N. Morphology of living cells cultured on nanowire arrays with varying nanowire densities and diameters. *Sci. China Life Sci.* **2018**, *61*, 427–435, doi:10.1007/s11427-017-9264-2.

39. Hällström, W.; Mårtensson, T.; Prinz, C.; Gustavsson, P.; Montelius, L.; Samuelson, L.; Kanje, M. Gallium Phosphide Nanowires as a Substrate for Cultured Neurons. *Nano Lett.* **2007**, *7*, 2960–2965, doi:10.1021/nl070728e.

40. Moyen, E.; Hama, A.; Ismailova, E.; Assaud, L.; Malliaras, G.; Hanbücken, M.; Owens, R.M. Nanostructured conducting polymers for stiffness controlled cell adhesion. *Nanotechnology* **2016**, *27*, 074001, doi:10.1088/0957-4484/27/7/074001.

41. Keefer, E.W.; Botterman, B.R.; Romero, M.I.; Rossi, A.F.; Gross, G.W. Carbon nanotube coating improves neuronal recordings. *Nat. Nanotechnol.* **2008**, *3*, 434–439, doi:10.1038/nnano.2008.174.

42. Seiti, M.; Ginestra, P.S.; Ceretti, E.; Ferraris, E.; Ranga, A. Emerging Three-Dimensional Integrated Systems for Biomimetic Neural In Vitro Cultures. *Adv. Mater. Interfaces* **2022**, *9*, 2101297, doi:10.1002/admi.202101297.

43. Ozgun, A.; Lomboni, D.; Arnott, H.; Staines, W.A.; Woulfe, J.; Variola, F. Biomaterials-based strategies for in vitro neural models. *Biomater. Sci.* **2022**, *10*, 1134–1165, doi:10.1039/D1BM01361K.

44. Brofiga, M.; Pisano, M.; Raiteri, R.; Massobrio, P. On the road to the brain-on-a-chip: a review on strategies, methods, and applications. *J. Neural Eng.* **2021**, *18*, 041005, doi:10.1088/1741-2552/ac15e4.

45. Maoz, B.M. Brain-on-a-Chip: Characterizing the next generation of advanced in vitro platforms for modeling the central nervous system. *APL Bioeng.* **2021**, *5*, 030902, doi:10.1063/5.0055812.

46. Bang, S.; Jeong, S.; Choi, N.; Kim, H.N. Brain-on-a-chip: A history of development and future perspective. *Biomicrofluidics* **2019**, *13*, 051301, doi:10.1063/1.5120555.

47. Huh, D.; Matthews, B.D.; Mammoto, A.; Montoya-Zavala, M.; Hsin, H.Y.; Ingber, D.E. Reconstituting Organ-Level Lung Functions on a Chip. *Science.* **2010**, *328*, 1662–1668, doi:10.1126/science.1188302.

48. Bavli, D.; Prill, S.; Ezra, E.; Levy, G.; Cohen, M.; Vinken, M.; Vanfleteren, J.; Jaeger, M.; Nahmias, Y. Real-time monitoring of metabolic function in liver-on-chip microdevices tracks the dynamics of mitochondrial dysfunction. *Proc. Natl. Acad. Sci.* **2016**, *113*, E2231–E2240, doi:10.1073/pnas.1522556113.

49. Yin, L.; Du, G.; Zhang, B.; Zhang, H.; Yin, R.; Zhang, W.; Yang, S.-M. Efficient Drug Screening and Nephrotoxicity Assessment on Co-culture Microfluidic Kidney Chip. *Sci. Rep.* **2020**, *10*, 6568, doi:10.1038/s41598-020-63096-3.

50. Kitsara, M.; Kontziampasis, D.; Agbulut, O.; Chen, Y. Heart on a chip: Micro-nanofabrication and microfluidics steering the future of cardiac tissue engineering. *Microelectron. Eng.* **2019**, *203–204*, 44–62, doi:10.1016/j.mee.2018.11.001.

51. Bahmaee, H.; Owen, R.; Boyle, L.; Perrault, C.M.; Garcia-Granada, A.A.; Reilly, G.C.; Claeyssens, F. Design and Evaluation of an Osteogenesis-on-a-Chip Microfluidic Device Incorporating 3D Cell Culture. *Front. Bioeng. Biotechnol.* **2020**, *8*, 1–17, doi:10.3389/fbioe.2020.557111.

52. Risueño, I.; Valencia, L.; Jorcano, J.L.; Velasco, D. Skin-on-a-chip models: General overview and future perspectives. *APL Bioeng.* **2021**, *5*, 030901, doi:10.1063/5.0046376.

53. Zhu, Y.; Mandal, K.; Hernandez, A.L.; Kawakita, S.; Huang, W.; Bandaru, P.; Ahadian, S.; Kim, H.-J.; Jucaud, V.; Dokmeci, M.R.; et al. State of the art in integrated biosensors for organ-on-a-chip applications. *Curr. Opin. Biomed. Eng.* **2021**, *19*, 100309, doi:10.1016/j.cobme.2021.100309.

54. Ahmed, T. Organ-on-a-chip microengineering for bio-mimicking disease models and revolutionizing drug discovery. *Biosens. Bioelectron. X* **2022**, *11*, 100194, doi:10.1016/j.biosx.2022.100194.

55. Tan, H.-Y.; Cho, H.; Lee, L.P. Human mini-brain models. *Nat. Biomed. Eng.* **2021**, *5*, 11–25, doi:10.1038/s41551-020-00643-3.

56. Hong, N.; Nam, Y. Neurons-on-a-Chip: In Vitro NeuroTools. *Mol. Cells* **2022**, *45*, 76–83, doi:10.14348/molcells.2022.2023.

57. Obien, M.E.J.; Deligkaris, K.; Bullmann, T.; Bakkum, D.J.; Frey, U. Revealing neuronal function through microelectrode array recordings. *Front. Neurosci.* **2015**, *8*, 423, doi:10.3389/fnins.2014.00423.

58. Wallace, K.; Strickland, J.D.; Valdivia, P.; Mundy, W.R.; Shafer, T.J. A multiplexed assay for determination of neurotoxicant effects on spontaneous network activity and

viability from microelectrode arrays. *Neurotoxicology* **2015**, *49*, 79–85, doi:10.1016/j.neuro.2015.05.007.

59. Han, Y.; Li, H.; Lang, Y.; Zhao, Y.; Sun, H.; Zhang, P.; Ma, X.; Han, J.; Wang, Q.; Zhou, J.; et al. The Effects of Acute GABA Treatment on the Functional Connectivity and Network Topology of Cortical Cultures. *Neurochem. Res.* **2017**, *42*, 1394–1402, doi:10.1007/s11064-017-2190-3.

60. Tanwar, A.; Gandhi, H.A.; Kushwaha, D.; Bhattacharya, J. A review on microelectrode array fabrication techniques and their applications. *Mater. Today Chem.* **2022**, *26*, 101153, doi:10.1016/j.mtchem.2022.101153.

61. Lam, D.; Fischer, N.O.; Enright, H.A. Probing function in 3D neuronal cultures: A survey of 3D multielectrode array advances. *Curr. Opin. Pharmacol.* **2021**, *60*, 255–260, doi:10.1016/j.coph.2021.08.003.

62. Demircan Yalcin, Y.; Bastiaens, A.J.; Frimat, J.-P.; Luttge, R. Long-term brain-on-chip: Multielectrode array recordings in 3D neural cell cultures. *J. Vac. Sci. Technol. B* **2021**, *39*, 064004, doi:10.1116/6.0001297.

63. Paulk, A.C.; Kfir, Y.; Khanna, A.R.; Mustroph, M.L.; Trautmann, E.M.; Soper, D.J.; Stavisky, S.D.; Welkenhuysen, M.; Dutta, B.; Shenoy, K. V.; et al. Large-scale neural recordings with single neuron resolution using Neuropixels probes in human cortex. *Nat. Neurosci.* **2022**, *25*, 252–263, doi:10.1038/s41593-021-00997-0.

64. Wu, N.; Wan, S.; Su, S.; Huang, H.; Dou, G.; Sun, L. Electrode materials for brain–machine interface: A review. *InfoMat* **2021**, *3*, 1174–1194, doi:10.1002/inf2.12234.

65. Guido, K.; Clavijo, A.; Zhu, K.; Ding, X.; Ma, K. Strategies to Improve Neural Electrode Performance. In *Neural Interface Engineering*; Springer International Publishing: Cham, 2020; pp. 173–199.

66. Renz, A.F.; Reichmuth, A.M.; Stauffer, F.; Thompson-Steckel, G.; Vörös, J. A guide towards long-term functional electrodes interfacing neuronal tissue. *J. Neural Eng.* **2018**, *15*, 061001, doi:10.1088/1741-2552/aae0c2.

67. Moeendarbary, E.; Weber, I.P.; Sheridan, G.K.; Koser, D.E.; Soleman, S.; Haenzi, B.; Bradbury, E.J.; Fawcett, J.; Franze, K. The soft mechanical signature of glial scars in the central nervous system. *Nat. Commun.* **2017**, *8*, 14787, doi:10.1038/ncomms14787.

68. Song, E.; Li, J.; Won, S.M.; Bai, W.; Rogers, J.A. Materials for flexible bioelectronic systems as chronic neural interfaces. *Nat. Mater.* **2020**, *19*, 590–603, doi:10.1038/s41563-020-0679-7.

69. Shi, Y.; Liu, R.; He, L.; Feng, H.; Li, Y.; Li, Z. Recent development of implantable and flexible nerve electrodes. *Smart Mater. Med.* **2020**, *1*, 131–147, doi:10.1016/j.smaim.2020.08.002.

70. Woods, G.A.; Rommelfanger, N.J.; Hong, G. Bioinspired Materials for In Vivo Bioelectronic Neural Interfaces. *Matter* **2020**, *3*, 1087–1113, doi:10.1016/j.matt.2020.08.002.

71. Li, H.; Wang, J.; Fang, Y. Bioinspired flexible electronics for seamless neural interfacing and chronic recording. *Nanoscale Adv.* **2020**, *2*, 3095–3102, doi:10.1039/D0NA00323A.

72. Khalili, A.; Ahmad, M. A Review of Cell Adhesion Studies for Biomedical and Biological Applications. *Int. J. Mol. Sci.* **2015**, *16*, 18149–18184, doi:10.3390/ijms160818149.

73.   Roach, P.; Parker, T.; Gadegaard, N.; Alexander, M.R. Surface strategies for control of neuronal cell adhesion: A review. *Surf. Sci. Rep.* **2010**, *65*, 145–173, doi:10.1016/j.surfrep.2010.07.001.

74.   Ganji, M.; Kaestner, E.; Hermiz, J.; Rogers, N.; Tanaka, A.; Cleary, D.; Lee, S.H.; Snider, J.; Halgren, M.; Cosgrove, G.R.; et al. Development and Translation of PEDOT:PSS Microelectrodes for Intraoperative Monitoring. *Adv. Funct. Mater.* **2018**, *28*, 1700232, doi:10.1002/adfm.201700232.

75.   Susloparova, A.; Halliez, S.; Begard, S.; Colin, M.; Buée, L.; Pecqueur, S.; Alibart, F.; Thomy, V.; Arscott, S.; Pallecchi, E.; et al. Low impedance and highly transparent microelectrode arrays (MEA) for in vitro neuron electrical activity probing. *Sensors Actuators B Chem.* **2021**, *327*, 128895, doi:10.1016/j.snb.2020.128895.

76.   Sánchez, G.; Dalchiele, E.; Bologna Alles, A. Electrical characterization of titanium nitride surfaces for pacing electrodes. *J. Mater. Sci.* **2006**, *41*, 3241–3247, doi:10.1007/s10853-005-5477-8.

77.   Ghasemi-Mobarakeh, L.; Kolahreez, D.; Ramakrishna, S.; Williams, D. Key terminology in biomaterials and biocompatibility. *Curr. Opin. Biomed. Eng.* **2019**, *10*, 45–50, doi:10.1016/j.cobme.2019.02.004.

78.   Bernard, M.; Jubeli, E.; Pungente, M.D.; Yagoubi, N. Biocompatibility of polymer-based biomaterials and medical devices – regulations, in vitro screening and risk-management. *Biomater. Sci.* **2018**, *6*, 2025–2053, doi:10.1039/C8BM00518D.

79.   Jäkel, S.; Dimou, L. Glial Cells and Their Function in the Adult Brain: A Journey through the History of Their Ablation. *Front. Cell. Neurosci.* **2017**, *11*, doi:10.3389/fncel.2017.00024.

80.   Bear, M.F.; Connors, B.W.; Paradiso, M.A. *Neuroscience Exploring the Brain*; Fourth edi.; Wolters Kluwer, 2016; ISBN 978-0-7817-7817-6.

81.   Molnar, C.; Gair, J. *Concepts of Biology*; 1st Canadi.; BCampus, 2015; ISBN 978-1-989623-98-5.

82.   Kandel, E.R. *Principles of Neural Science*; Sixth edit.; McGraw-Hill, 2021; ISBN 978-1-25-964224-1.

83.   Morarach, K.; Mikhailova, A.; Knoflach, V.; Memic, F.; Kumar, R.; Li, W.; Ernfors, P.; Marklund, U. Diversification of molecularly defined myenteric neuron classes revealed by single-cell RNA sequencing. *Nat. Neurosci.* **2021**, *24*, 34–46, doi:10.1038/s41593-020-00736-x.

84.   Herculano-Houzel, S.; Dos Santos, S. You Do Not Mess with the Glia. *Neuroglia* **2018**, *1*, 193–219, doi:10.3390/neuroglia1010014.

85.   Vert, M.; Doi, Y.; Hellwich, K.-H.; Hess, M.; Hodge, P.; Kubisa, P.; Rinaudo, M.; Schué, F. Terminology for biorelated polymers and applications (IUPAC Recommendations 2012). *Pure Appl. Chem.* **2012**, *84*, 377–410, doi:10.1351/PAC-REC-10-12-04.

86.   Wagner, W.R.; E., S.-E.S.; Zhang, G.; Yaszemski, M.J. *Biomaterials Science*; Fourth edi.; Elsevier, 2020; ISBN 9780128161371.

87.   Pignatello, R. *Advances in Biomaterials Science and Biomedical Applications*; 1st editio.; InTech, 2013; ISBN 978-953-51-1051-4.

88.   Wang, X. Overview on Biocompatibilities of Implantable Biomaterials. In *Advances in*

Biomaterials Science and Biomedical Applications; Pignatello, R., Ed.; InTech, 2013 ISBN 978-953-51-1051-4.

89.   Castner, D.G.; Ratner, B.D. Biomedical surface science: Foundations to frontiers. *Surf. Sci.* **2002**, *500*, 28–60, doi:10.1016/S0039-6028(01)01587-4.

90.   Moeller, M.; Matyjaszewski, K. *Polymer Science: A Comprehensive Reference*; Elsevier Science, 2012; ISBN 978-0-08-087862-1.

91.   Anderson, J.M. Biocompatibility. In *Polymer Science: A Comprehensive Reference*; Matyjaszewski, K., Möller, M., Eds.; Elsevier, 2012; Vol. 9, pp. 363–383 ISBN 978-0-08-087862-1.

92.   Lotfi, M.; Nejib, M.; Naceur, M. Cell Adhesion to Biomaterials: Concept of Biocompatibility. In *Advances in Biomaterials Science and Biomedical Applications*; Pignatello, R., Ed.; InTech, 2013 ISBN 978-953-51-1051-4.

93.   Huang, W.; Anvari, B.; Torres, J.H.; Lebaron, R.G.; Athanasiou, K.A. Temporal effects of cell adhesion on mechanical characteristics of the single chondrocyte. *J. Orthop. Res.* **2003**, *21*, 88–95, doi:10.1016/S0736-0266(02)00130-4.

94.   Yu, L.M.Y.; Leipzig, N.D.; Shoichet, M.S. Promoting neuron adhesion and growth. *Mater. Today* **2008**, *11*, 36–43, doi:10.1016/S1369-7021(08)70088-9.

95.   Szekanecz, Z.; Koch, A.E. Cell-cell interactions in synovitis. Endothelial cells and immune cell migration. *Arthritis Res.* **2000**, *2*, 368–373, doi:10.1186/ar114.

96.   Perinpanayagam, H.; Zaharias, R.; Stanford, C.; Brand, R.; Keller, J.; Schneider, G. Early cell adhesion events differ between osteoporotic and non-osteoporotic osteoblasts. *J. Orthop. Res.* **2001**, *19*, 993–1000, doi:10.1016/S0736-0266(01)00045-6.

97.   Serhan, C.N.; Savill, J. Resolution of inflammation: the beginning programs the end. *Nat. Immunol.* **2005**, *6*, 1191–1197, doi:10.1038/ni1276.

98.   Hirohashi, S.; Kanai, Y. Cell adhesion system and human cancer morphogenesis. *Gann Monogr. Cancer Res.* **2004**, *52*, 13–26.

99.   Zaidel-Bar, R.; Cohen, M.; Addadi, L.; Geiger, B. Hierarchical assembly of cell–matrix adhesion complexes. *Biochem. Soc. Trans.* **2004**, *32*, 416–420, doi:10.1042/bst0320416.

100.   Hynes, R.O. Integrins: Versatility, modulation, and signaling in cell adhesion. *Cell* **1992**, *69*, 11–25, doi:10.1016/0092-8674(92)90115-S.

101.   Zimmerman, E.; Geiger, B.; Addadi, L. Initial Stages of Cell-Matrix Adhesion Can Be Mediated and Modulated by Cell-Surface Hyaluronan. *Biophys. J.* **2002**, *82*, 1848–1857, doi:10.1016/S0006-3495(02)75535-5.

102.   Geiger, B.; Yamada, K.M. Molecular Architecture and Function of Matrix Adhesions. *Cold Spring Harb. Perspect. Biol.* **2011**, *3*, a005033–a005033, doi:10.1101/cshperspect.a005033.

103.   Geiger, B.; Spatz, J.P.; Bershadsky, A.D. Environmental sensing through focal adhesions. *Nat. Rev. Mol. Cell Biol.* **2009**, *10*, 21–33, doi:10.1038/nrm2593.

104.   Parsons, J.T.; Horwitz, A.R.; Schwartz, M.A. Cell adhesion: integrating cytoskeletal dynamics and cellular tension. *Nat. Rev. Mol. Cell Biol.* **2010**, *11*, 633–643, doi:10.1038/nrm2957.

105. Zaidel-Bar, R.; Ballestrem, C.; Kam, Z.; Geiger, B. Early molecular events in the assembly of matrix adhesions at the leading edge of migrating cells. *J. Cell Sci.* **2003**, *116*, 4605–4613, doi:10.1242/jcs.00792.

106. Alberts, B.; Johnson, A.; Lewis, J.; Raff, M.; Roberts, K.; Walter, P. *Molecular Biology of the Cell*; 5th ed.; Garland Science: New York, 2007; ISBN 9780815341055.

107. Dembo, M.; Torney, D.C.; Saxman, K.; Hammer, D. The reaction-limited kinetics of membrane-to-surface adhesion and detachment. *Proc. R. Soc. London. Ser. B. Biol. Sci.* **1988**, *234*, 55–83, doi:10.1098/rspb.1988.0038.

108. Shen, Y.; Nakajima, M.; Kojima, S.; Homma, M.; Kojima, M.; Fukuda, T. Single cell adhesion force measurement for cell viability identification using an AFM cantilever-based micro putter. *Meas. Sci. Technol.* **2011**, *22*, 115802, doi:10.1088/0957-0233/22/11/115802.

109. Shinde, A.; Illath, K.; Gupta, P.; Shinde, P.; Lim, K.-T.; Nagai, M.; Santra, T.S. A Review of Single-Cell Adhesion Force Kinetics and Applications. *Cells* **2021**, *10*, 577, doi:10.3390/cells10030577.

110. Hong, S.; Ergezen, E.; Lec, R.; Barbee, K.A. Real-time analysis of cell–surface adhesive interactions using thickness shear mode resonator. *Biomaterials* **2006**, *27*, 5813–5820, doi:10.1016/j.biomaterials.2006.07.031.

111. Taubenberger, A.; Cisneros, D.A.; Friedrichs, J.; Puech, P.-H.; Muller, D.J.; Franz, C.M. Revealing Early Steps of α 2 β 1 Integrin-mediated Adhesion to Collagen Type I by Using Single-Cell Force Spectroscopy. *Mol. Biol. Cell* **2007**, *18*, 1634–1644, doi:10.1091/mbc.e06-09-0777.

112. Taubenberger, A. V.; Hutmacher, D.W.; Muller, D.J. Single-Cell Force Spectroscopy, an Emerging Tool to Quantify Cell Adhesion to Biomaterials. *Tissue Eng. Part B Rev.* **2014**, *20*, 40–55, doi:10.1089/ten.teb.2013.0125.

113. Helenius, J.; Heisenberg, C.-P.; Gaub, H.E.; Muller, D.J. Single-cell force spectroscopy. *J. Cell Sci.* **2008**, *121*, 1785–1791, doi:10.1242/jcs.030999.

114. Dufrêne, Y.F.; Viljoen, A.; Mignolet, J.; Mathelié-Guinlet, M. AFM in cellular and molecular microbiology. *Cell. Microbiol.* **2021**, *23*, 1–12, doi:10.1111/cmi.13324.

115. Viljoen, A.; Mathelié-Guinlet, M.; Ray, A.; Strohmeyer, N.; Oh, Y.J.; Hinterdorfer, P.; Müller, D.J.; Alsteens, D.; Dufrêne, Y.F. Force spectroscopy of single cells using atomic force microscopy. *Nat. Rev. Methods Prim.* **2021**, *1*, 64, doi:10.1038/s43586-021-00067-6.

116. Shen, C. *Atomic Force Microscopy for Energy Research*; 1st editio.; CRC Press: Boca Raton, 2022; ISBN 9781003174042.

117. Main, K.H.S.; Provan, J.I.; Haynes, P.J.; Wells, G.; Hartley, J.A.; Pyne, A.L.B. Atomic force microscopy—A tool for structural and translational DNA research. *APL Bioeng.* **2021**, *5*, 031504, doi:10.1063/5.0054294.

118. Heath, G.R.; Kots, E.; Robertson, J.L.; Lansky, S.; Khelashvili, G.; Weinstein, H.; Scheuring, S. Localization atomic force microscopy. *Nature* **2021**, *594*, 385–390, doi:10.1038/s41586-021-03551-x.

119. Mondarte, E.A.Q.; Tahara, H.; Suthiwanich, K.; Song, S.; Wang, F.; Hayashi, T. Lab on a Tip: Atomic Force Microscopy as a Versatile Analytical Tool for Nano-bioscience. *Sensors Mater.* **2021**, *33*, 223, doi:10.18494/SAM.2021.3069.

120. Zubar, T.I.; Fedosyuk, V.M.; Trukhanov, S. V.; Tishkevich, D.I.; Michels, D.; Lyakhov, D.; Trukhanov, A. V. Method of surface energy investigation by lateral AFM: application to control growth mechanism of nanostructured NiFe films. *Sci. Rep.* **2020**, *10*, 14411, doi:10.1038/s41598-020-71416-w.

121. Krieg, M.; Fläschner, G.; Alsteens, D.; Gaub, B.M.; Roos, W.H.; Wuite, G.J.L.; Gaub, H.E.; Gerber, C.; Dufrêne, Y.F.; Müller, D.J. Atomic force microscopy-based mechanobiology. *Nat. Rev. Phys.* **2019**, *1*, 41–57, doi:10.1038/s42254-018-0001-7.

122. Capizzi, G.; Lo Sciuto, G.; Napoli, C.; Shikler, R.; Woźniak, M. Optimizing the Organic Solar Cell Manufacturing Process by Means of AFM Measurements and Neural Networks. *Energies* **2018**, *11*, 1221, doi:10.3390/en11051221.

123. Toca-Herrera, J.L. Atomic Force Microscopy Meets Biophysics, Bioengineering, Chemistry, and Materials Science. *ChemSusChem* **2019**, *12*, 603–611, doi:10.1002/cssc.201802383.

124. Zhang, Z.; Said, S.; Smith, K.; Jervis, R.; Howard, C.A.; Shearing, P.R.; Brett, D.J.L.; Miller, T.S. Characterizing Batteries by In Situ Electrochemical Atomic Force Microscopy: A Critical Review. *Adv. Energy Mater.* **2021**, *11*, doi:10.1002/aenm.202101518.

125. Morris, V.J.; Kirby, A.R.; Gunning, P.A. *Atomic Force Microscopy For Biologists*; 2nd editio.; World Scientific Publishing Company, 2009; ISBN 9781908978219.

126. Hutter, J.L.; Bechhoefer, J. Calibration of atomic-force microscope tips. *Rev. Sci. Instrum.* **1993**, *64*, 1868–1873, doi:10.1063/1.1143970.

127. Butt, H.J.; Jaschke, M. Calculation of thermal noise in atomic force microscopy. *Nanotechnology* **1995**, *6*, 1–7, doi:10.1088/0957-4484/6/1/001.

128. Sporns, O. *Networks of the Brain*; MIT Press: Cambridge, MA, US, 2011; ISBN 978-0-262-01469-4.

129. Fornito, A.; Zalesky, A.; Bullmore, E.T. *Fundamentals of Brain Network Analysis*; Elsevier, 2016; ISBN 9780124079083.

130. MacQueen, J. Some methods for classification and analysis of multivariate observations. In *Proceedings of the fifth Berkeley symposium on mathematical statistics and probability*; Lecam, L., Neyman, J., Eds.; University of California Press: Oakland, CA, USA, 1967; pp. 281--297.

131. Jain, A.K.; Murty, M.N.; Flynn, P.J. Data clustering. *ACM Comput. Surv.* **1999**, *31*, 264–323, doi:10.1145/331499.331504.

132. Jain, A.K. Data clustering: 50 years beyond K-means. *Pattern Recognit. Lett.* **2010**, *31*, 651–666, doi:10.1016/j.patrec.2009.09.011.

133. Thorndike, R.L. Who belongs in the family? *Psychometrika* **1953**, *18*, 267–276, doi:10.1007/BF02289263.

134. Tibshirani, R.; Walther, G.; Hastie, T. Estimating the number of clusters in a data set via the gap statistic. *J. R. Stat. Soc. Ser. B* **2001**, *63*, 411–423, doi:10.1111/1467-9868.00293.

135. Rousseeuw, P.J. Silhouettes: A graphical aid to the interpretation and validation of cluster analysis. *J. Comput. Appl. Math.* **1987**, *20*, 53–65, doi:10.1016/0377-0427(87)90125-7.

136. Berryman, J.G. Measurement of spatial correlation functions using image processing techniques. *J. Appl. Phys.* **1985**, *57*, 2374–2384, doi:10.1063/1.334346.

137. Berryman, J.G.; Blair, S.C. Use of digital image analysis to estimate fluid permeability of porous materials: Application of two-point correlation functions. *J. Appl. Phys.* **1986**, *60*, 1930–1938, doi:10.1063/1.337245.

138. Baker, D.R.; Sirbescu, M.-L.; Maneta, V.; Webber, K.L.; Simmons, W.B. Quantitative Analysis of Natural and Experimental Graphic Textures. *Can. Mineral.* **2018**, *56*, 625–643, doi:10.3749/canmin.1700084.

139. Gilles, J.-F.; Dos Santos, M.; Boudier, T.; Bolte, S.; Heck, N. DiAna, an ImageJ tool for object-based 3D co-localization and distance analysis. *Methods* **2017**, *115*, 55–64, doi:10.1016/j.ymeth.2016.11.016.

140. Thomas, C.A.; Springer, P.A.; Loeb, G.E.; Berwald-Netter, Y.; Okun, L.M. A miniature microelectrode array to monitor the bioelectric activity of cultured cells. *Exp. Cell Res.* **1972**, *74*, 61–66, doi:10.1016/0014-4827(72)90481-8.

141. Spira, M.E.; Hai, A. Multi-electrode array technologies for neuroscience and cardiology. *Nat. Nanotechnol.* **2013**, *8*, 83–94, doi:10.1038/nnano.2012.265.

142. Bakkum, D.J.; Frey, U.; Radivojevic, M.; Russell, T.L.; Müller, J.; Fiscella, M.; Takahashi, H.; Hierlemann, A. Tracking axonal action potential propagation on a high-density microelectrode array across hundreds of sites. *Nat. Commun.* **2013**, *4*, 2181, doi:10.1038/ncomms3181.

143. Müller, J.; Ballini, M.; Livi, P.; Chen, Y.; Radivojevic, M.; Shadmani, A.; Viswam, V.; Jones, I.L.; Fiscella, M.; Diggelmann, R.; et al. High-resolution CMOS MEA platform to study neurons at subcellular, cellular, and network levels. *Lab Chip* **2015**, *15*, 2767–2780, doi:10.1039/C5LC00133A.

144. Leach, J. Bridging the divide between neuroprosthetic design, tissue engineering and neurobiology. *Front. Neuroeng.* **2010**, *2*, 1–19, doi:10.3389/neuro.16.018.2009.

145. Wang, S.; Zhang, J.; Gharbi, O.; Vivier, V.; Gao, M.; Orazem, M.E. Electrochemical impedance spectroscopy. *Nat. Rev. Methods Prim.* **2021**, *1*, 41, doi:10.1038/s43586-021-00039-w.

146. Weber, S.G. Signal-to-noise ratio in microelectrode-array-based electrochemical detectors. *Anal. Chem.* **1989**, *61*, 295–302, doi:10.1021/ac00179a004.

147. Abend, A.; Steele, C.; Schmidt, S.; Frank, R.; Jahnke, H.-G.; Zink, M. Proliferation and Cluster Analysis of Neurons and Glial Cell Organization on Nanocolumnar TiN Substrates. *Int. J. Mol. Sci.* **2020**, *21*, 6249, doi:10.3390/ijms21176249.

148. Abend, A.; Steele, C.; Jahnke, H.-G.; Zink, M. Adhesion of Neurons and Glial Cells with Nanocolumnar TiN Films for Brain-Machine Interfaces. *Int. J. Mol. Sci.* **2021**, *22*, 8588, doi:10.3390/ijms22168588.

149. Abend, A.; Steele, C.; Schmidt, S.; Frank, R.; Jahnke, H.-G.; Zink, M. Neuronal and glial cell co-culture organization and impedance spectroscopy on nanocolumnar TiN films for lab-on-a-chip devices. *Biomater. Sci.* **2022**, doi:10.1039/D2BM01066F.

150. Schreiber, H.; Kinzl, H.-P. Microscope Image Analysis in Biomaterial Testing. In *Interfaces in Medicine and Mechanics—2*; Springer Netherlands: Dordrecht, 1991; pp. 474–482 ISBN 978-94-011-3852-9.

112

151. Bratlie, K.M.; Dang, T.T.; Lyle, S.; Nahrendorf, M.; Weissleder, R.; Langer, R.; Anderson, D.G. Rapid Biocompatibility Analysis of Materials via In Vivo Fluorescence Imaging of Mouse Models. *PLoS One* **2010**, *5*, e10032, doi:10.1371/journal.pone.0010032.

152. Uka, A.; Ndreu Halili, A.; Polisi, X.; Topal, A.O.; Imeraj, G.; Vrana, N.E. Basis of Image Analysis for Evaluating Cell Biomaterial Interaction Using Brightfield Microscopy. *Cells Tissues Organs* **2021**, *210*, 77–104, doi:10.1159/000512969.

153. Klußmann-Fricke, B.-J.; Reske, T.; Schmitz, K.-P.; Siewert, S.; Khaimov, V. Quantitative evaluation of cell morphology and material interactions on opaque biomaterials. *Curr. Dir. Biomed. Eng.* **2021**, *7*, 664–667, doi:10.1515/cdbme-2021-2169.

154. Vallejo-Giraldo, C.; Pampaloni, N.P.; Pallipurath, A.R.; Mokarian-Tabari, P.; O'Connell, J.; Holmes, J.D.; Trotier, A.; Krukiewicz, K.; Orpella-Aceret, G.; Pugliese, E.; et al. Preparation of Cytocompatible ITO Neuroelectrodes with Enhanced Electrochemical Characteristics Using a Facile Anodic Oxidation Process. *Adv. Funct. Mater.* **2018**, *28*, 1605035, doi:10.1002/adfm.201605035.

155. Khan, S.P.; Auner, G.G.; Newaz, G.M. Influence of nanoscale surface roughness on neural cell attachment on silicon. *Nanomedicine Nanotechnology, Biol. Med.* **2005**, *1*, 125–129, doi:10.1016/j.nano.2005.03.007.

156. Fan, Y.W.; Cui, F.Z.; Chen, L.N.; Zhai, Y.; Xu, Q.Y.; Lee, I.S. Adhesion of neural cells on silicon wafer with nano-topographic surface. *Appl. Surf. Sci.* **2002**, *187*, 313–318, doi:10.1016/S0169-4332(01)01046-7.

157. Yoon, S.-B.; Lee, G.; Park, S.B.; Cho, H.; Lee, J.-O.; Koh, B. Properties of differentiated SH-SY5Y grown on carbon-based materials. *RSC Adv.* **2020**, *10*, 19382–19389, doi:10.1039/D0RA03383A.

158. Panagiotakopoulou, M.; Lendenmann, T.; Pramotton, F.M.; Giampietro, C.; Stefopoulos, G.; Poulikakos, D.; Ferrari, A. Cell cycle–dependent force transmission in cancer cells. *Mol. Biol. Cell* **2018**, *29*, 2528–2539, doi:10.1091/mbc.E17-12-0726.

159. Lock, J.G.; Jones, M.C.; Askari, J.A.; Gong, X.; Oddone, A.; Olofsson, H.; Göransson, S.; Lakadamyali, M.; Humphries, M.J.; Strömblad, S. Reticular adhesions are a distinct class of cell-matrix adhesions that mediate attachment during mitosis. *Nat. Cell Biol.* **2018**, *20*, 1290–1302, doi:10.1038/s41556-018-0220-2.

160. Dao, L.; Weiland, U.; Hauser, M.; Nazarenko, I.; Kalt, H.; Bastmeyer, M.; Franz, C.M. Revealing non-genetic adhesive variations in clonal populations by comparative single-cell force spectroscopy. *Exp. Cell Res.* **2012**, *318*, 2155–2167, doi:10.1016/j.yexcr.2012.06.017.

161. Betz, T.; Koch, D.; Lu, Y.-B.; Franze, K.; Kas, J.A. Growth cones as soft and weak force generators. *Proc. Natl. Acad. Sci.* **2011**, *108*, 13420–13425, doi:10.1073/pnas.1106145108.

162. Kerstein, P.C.; Nichol IV, R.H.; Gomez, T.M. Mechanochemical regulation of growth cone motility. *Front. Cell. Neurosci.* **2015**, *9*, 1–16, doi:10.3389/fncel.2015.00244.

163. Ravi, V.M.; Joseph, K.; Wurm, J.; Behringer, S.; Garrelfs, N.; Errico, P. d'; Naseri, Y.; Franco, P.; Meyer-Luehmann, M.; Sankowski, R.; et al. Human organotypic brain slice culture: a novel framework for environmental research in neuro-oncology. *Life Sci. Alliance* **2019**, *2*, e201900305, doi:10.26508/lsa.201900305.

164. Er, J.C.; Leong, C.; Teoh, C.L.; Yuan, Q.; Merchant, P.; Dunn, M.; Sulzer, D.; Sames, D.;

Bhinge, A.; Kim, D.; et al. NeuO: a Fluorescent Chemical Probe for Live Neuron Labeling. *Angew. Chemie Int. Ed.* **2015**, *54*, 2442–2446, doi:10.1002/anie.201408614.

165. Yang, X.; Zhou, T.; Zwang, T.J.; Hong, G.; Zhao, Y.; Viveros, R.D.; Fu, T.-M.; Gao, T.; Lieber, C.M. Bioinspired neuron-like electronics. *Nat. Mater.* **2019**, *18*, 510–517, doi:10.1038/s41563-019-0292-9.

166. Idris, F.; Hanna Muharram, S.; Zaini, Z.; Diah, S. Establishment of murine in vitro blood-brain barrier models using immortalized cell lines: co-cultures of brain endothelial cells, astrocytes, and neurons. *bioRxiv* **2018**, 435990, doi:10.1101/435990.

167. Pan, C.; Kumar, C.; Bohl, S.; Klingmueller, U.; Mann, M. Comparative Proteomic Phenotyping of Cell Lines and Primary Cells to Assess Preservation of Cell Type-specific Functions. *Mol. Cell. Proteomics* **2009**, *8*, 443–450, doi:10.1074/mcp.M800258-MCP200.

168. Heller, D.; Hoppe, A.; Restrepo, S.; Gatti, L.; Tournier, A.L.; Tapon, N.; Basler, K.; Mao, Y. EpiTools: An Open-Source Image Analysis Toolkit for Quantifying Epithelial Growth Dynamics. *Dev. Cell* **2016**, *36*, 103–116, doi:10.1016/j.devcel.2015.12.012.

169. Fränti, P.; Sieranoja, S. K-means properties on six clustering benchmark datasets. *Appl. Intell.* **2018**, *48*, 4743–4759, doi:10.1007/s10489-018-1238-7.

170. Fränti, P.; Sieranoja, S. How much can k-means be improved by using better initialization and repeats? *Pattern Recognit.* **2019**, *93*, 95–112, doi:10.1016/j.patcog.2019.04.014.

171. Ikotun, A.M.; Ezugwu, A.E.; Abualigah, L.; Abuhaija, B.; Heming, J. K-means clustering algorithms: A comprehensive review, variants analysis, and advances in the era of big data. *Inf. Sci. (Ny).* **2023**, *622*, 178–210, doi:10.1016/j.ins.2022.11.139.

172. Duda, Richard O and Hart, P.E. and others *Pattern classification and scene analysis*; Wiley New York, 1973; ISBN 978-0471223610.

Acknowledgments

First and foremost, I thank Prof. Mareike Zink for offering me the opportunity to work in her group on this exciting topic. I am grateful for her consistently supporting me academically, financially, and also morally. We went through a lot of ups and downs together during my time as a PhD student, but all challenges always ended up in progress. Mareike encouraged me to go beyond the scientifically beaten tracks and gave me the freedom to pursue my own ideas.

The second most important person who helped me succeed is my (back then) student Chelsie Steele. She is one of the most hard-working and academically gifted students I have ever met at university. Her support in coding and lab work is highly appreciated. Chelsie also made the long days in the lab quite a bit more fun.

I am thankful for the scientific and moral support of all the people in the Zink lab. Our conversations at the lunch table and in the lab made the whole PhD time more enjoyable. I even made new friends along the way.

A special thanks goes to Prof. Josef Käs for giving me access to quite a bit of expensive lab equipment and the expertise of the people of the Käs lab. Thomas Fuhs needs to be mentioned here for offering guidance and support at the AFM. Bernd Kohlstrunk, Undine Dietrich, and Claudia Brück saved me from a lot of technical and administrative work.

I am also grateful for the collaboration with the Molecular Biological-Biochemical Processing Technology group at the BBZ formerly headed by Prof. Andrea Robitzki. Especially Dr. Heinz-Georg Jahnke, Dr. Sabine Schmidt, and Dr. Ronny Frank helped move this research forward.

My thanks go to family and friends who provided support and encouragement during my time as a PhD student. We celebrated the good times and endured the hard times together. You always cheered on me.

Finally, my trustworthy companion Sir Isaac Newton supported me emotionally along the way. His successor Qui-Gon Jinn now follows in his pawprints and keeps the good work up.

Selbstständigkeitserklärung

Ich erkenne die Promotionsordnung der Fakultät für Physik und Geowissenschaften der Universität Leipzig an und versichere, dass ich die vorliegende Arbeit ohne unzulässige Hilfe und ohne Benutzung anderer als der angegebenen Hilfsmittel angefertigt habe und dass die aus fremden Quellen direkt oder indirekt übernommenen Gedanken in der Arbeit als solche kenntlichgemacht wurden.

Alle Personen, welche bei der Vorbereitung, Durchführung und Auswertung der Experimente sowie der Publikationen Unterstützung geleistet haben sind namentlich genannt.

Ich bestätige weiterhin, dass keine weiteren Personen bei der geistigen Herstellung der vorliegenden Arbeit beteiligt waren. Insbesondere habe ich nicht die Hilfe eines Promotionsberaters in Anspruch genommen. Weitere Personen haben weder von mir selbst noch in meinem Auftrag weder unmittelbar noch mittelbar geldwerte Leistungen für Arbeiten erhalten, die im Zusammenhang mit dem Inhalt der vorgelegten Dissertation stehen.

Die hier vorliegende Arbeit oder Teile davon wurden bisher weder im Inland noch im Ausland in gleicher oder ähnlicher Form einer Prüfungsbehörde zum Zweck einer Promotion oder eines anderen Prüfungsverfahrens vorgelegt.

Ich versichere, dass keine früheren erfolglosen Promotionsversuche stattgefunden haben.

Ort, Datum   Alice Abend

Interaction of Electrode Materials with Neuronal and Glial Cells

The brain is the most complex organ of a human being and it is not yet completely understood [1, 2]. Many of its essential biochemical functions are still under investigation [3, 4]. Especially in light of rising numbers of patients with neurodegenerative diseases, studies on architecture and function of the brain and its progressive deterioration in the case of degenerative illnesses are mandatory [5]. Employing suitable platforms to investigate neuronal function *in vitro* is a promising approach to closing these knowledge gaps [6]. Function of such lab-on-a-chip designs depends on suitable characteristics at the brain-machine interface. Biomaterials have to provide appropriate chemical and physical conditions for the neuronal cells. Hence, characteristics of the cell-machine interface need to be studied to effectively employ new biomaterials. Such well-developed brain-on-a-chip devices could potentially reduce the number of necessary animal experiments and would also help to solve associated problems such as high cost, low throughput, optical non-transparency, and ethical concerns. Overall, *in vitro* platform assays could accelerate future research activities. Suitable lab-on-a-chip designs to study neuronal function include for example multielectrode arrays (MEAs). More detailed measurements of cellular function on smaller spatial scales require miniaturization of MEAs. That can be achieved by developing new biomaterials with advantageous electrical characteristics like a lowered self-impedance for example. The interaction of these biomaterials with cells needs to be investigated to ensure good cell adhesion, proliferation, and electrical coupling.

For the project of this thesis, I studied and characterized the interaction of

human neuronal and glial cells (neuron-like SH-SY5Y and glia-like U-87 MG cells) with the electrode material titanium nitride with nanocolumnar surface topography (TiN nano) and its advantages in terms of electric and bioactive properties compared to gold (Au) and indium tin oxide (ITO) which are currently employed for MEAs and neuroelectrodes. The overall goal of the presented study is to leave the beaten tracks of classical biochemistry assays and explore new ways to assess biocompatibility in a more computational approach. To this end, I employ techniques from theoretical physics, mathematics, and computer science to implement a new image-based method that relies on minimal experimental effort but nevertheless provides key information on biocompatibility of the material. Generally, cellular networks and spatial cell distribution are investigated. To this end, autocorrelation function, unsupervised self-learning algorithms, and nearest neighbor analysis are employed to detect cell patterns and agglomerations. This novel approach is combined with tried and true techniques to monitor cell adhesion and electrochemical features like single-cell force spectroscopy and electrochemical impedance measurements. Single-cell experiments are combined with ensemble measurements to map a broader spectrum of cellular behavior. This project started with mono-culture for SH-SY5Y and U-87 MG cells respectively to establish the proposed algorithms. I expanded the experiments subsequently to co-culture measurements to gain a better understanding of the interplay between

both cell types. Neurons and glial cells do not merely coexist under physiology in vivo conditions but communicate and interact constantly.

Results of this study show the superiority of TiN nano as a potential biomaterial employed for *in vitro* lab-on-a-chip designs as well as for *in vivo* neural stimulation. TiN nano exhibits favorable growth conditions for neuronal cells as well as improved electrical characteristics like impedance magnitude and signal-to-noise ratio in comparison with other electrode materials.

The proposed image-based computational analysis of spatial cellular distribution proves to enable quantification of growth patterns. Both small and large cell agglomerations are detected and cell positions relative to each other can be observed. Interestingly, SH-SY5Y and U-87 MG reveal very different spatial distributions under mono- and co-culture conditions. The established method is universally applicable to cell types other than neuronal and quantifies the interaction of cells with biomaterials.

References

[1] von Bartheld, C.S.; Bahney, J.; Herculano Houzel, S. The search for true numbers of neurons and glial cells in the human brain: A review of 150 years of cell counting. *J. Comp. Neurol.* 2016, *524*.

[2] Lisman, J. The Challenge of Understanding the Brain: Where We Stand in 2015. *Neuron* 2015, *86*.

[3] Poldrack, R.A.; Farah, M.J. Progress and challenges in probing the human brain. *Nature* 2015, *526*.

[4] Batista-García-Ramó, K.; Fernández-Verdecia, C.I. What we know about the brain structure-function relationship. *Behav. Sci. (Basel).* 2018, *8*.

[5] Feigin, V.L.; Vos, T.; Nichols, E.; Owolabi, M.O.; Carroll, W.M.; Dichgans, M.; Deuschl, G.; Parmar, P.; Brainin, M.; Murray, C. The global burden of neurological disorders: translating evidence into policy. *Lancet Neurol.* 2020, *19*.

[6] Nikolakopoulou, P.; Rauti, R.; Voulgaris, D.; Shlomy, I.; Maoz, B.M.; Herland, A. Recent progress in translational engineered in vitro models of the central nervous system. *Brain* 2020, *143*.

Publication List – Author Contribution

<u>Alice Abend</u>, Chelsie Steele, Sabine Schmidt, Ronny Frank, Heinz-Georg Jahnke, and Mareike Zink. "Proliferation and Cluster Analysis of Neurons and Glial Cell Organization on Nanocolumnar TiN Substrates", *Int. J. Mol. Sci.* 2020.

Impact Factor Int. J. Mol. Sci. (2022): 6.208

Author contributions as declared in the publication [147]: Conceptualization, M.Z.; <u>methodology, A.A.,</u> C.S., R.F. and H.-G.J.; software, C.S.; <u>validation, A.A.,</u> C.S., H.-G.J. and M.Z.; <u>formal analysis, A.A.,</u> C.S. and R.F.; resources, S.S., H.-G.J. and M.Z.; <u>data curation, A.A.,</u> C.S., H.-G.J. and M.Z.; <u>writing—original draft preparation, A.A.,</u> H.-G.-J. and M.Z.; <u>writing—review and editing, A.A.,</u> C.S., H.-G.J. and M.Z.; <u>visualization, A.A.;</u> supervision, H.-G.J. and M.Z.; project administration, M.Z. and H.-G.J.; funding acquisition, M.Z. and H.-G.J.

I performed all cell experiments including fluorescence staining and the acquisition of fluorescence microscopy images. I did the cell proliferation analysis including data interpretation and the major part of data processing and interpretation of the radial autocorrelation method. C.S. contributed significantly to K-means data acquisition and I performed data processing and interpretation on clustering. I wrote the manuscript except for the paragraph in the results section on electrode material surface topography (2.1.) which was contributed by H.-G.J. and modified by me. I produced the graphics in the manuscript.

<u>Alice Abend</u>, Chelsie Steele, Heinz-Georg Jahnke, and Mareike Zink. "Adhesion of Neurons and Glial Cells with Nanocolumnar TiN Films for Brain-Machine Interfaces", *Int. J. Mol. Sci.* 2021.

Author contributions as declared in the publication [148]: Conceptualization, M.Z.; <u>methodology, A.A.,</u> M.Z. and H.-G.J.; software, C.S.; <u>validation, A.A.,</u> C.S., H.-G.J. and M.Z.; <u>formal analysis, A.A.</u> and C.S.; resources, H.-G.J. and M.Z.; <u>data curation, A.A.</u> and C.S.; <u>writing—original draft preparation, A.A.</u> and M.Z.; <u>writing—review and editing, A.A.,</u> C.S., H.-G.J. and M.Z.; <u>visualization, A.A.;</u> supervision, M.Z. and H.-G.J.; project administration, M.Z. and H.-G.J.; funding acquisition, M.Z. and H.-G.J.

I performed all experiments including single-cell force spectroscopy with the Cell Hesion AFM. I did the analysis and data interpretation on adhesion forces and detachment work. I performed the experiments including fluorescence staining and the acquisition of fluorescence microscopy images that were necessary for the cell spreading analysis. C.S. contributed to the cell spreading data acquisition and I performed data processing and interpretation on cell spreading. I wrote the manuscript and produced the graphics in the manuscript.

Alice Abend, Chelsie Steele, Sabine Schmidt, Ronny Frank, Heinz-Georg Jahnke, and Mareike Zink. „Neuronal and glial cell co-culture organization and impedance spectroscopy on nanocolumnar TiN films for lab-on-a-chip devices", *Biomater. Sci.* 2022.

Impact Factor Biomater. Sci. (2022): 7.590

Author contributions as declared in the publication [149]: Conceptualization, M. Z.; methodology, A. A., C. S., and H.-G. J.; software, A. A. and C. S.; validation, A. A., C. S., H.-G. J. and M. Z.; formal analysis, A. A., C. S., and R. F.; resources, S. S., H.-G. J. and M. Z.; data curation, A. A., C. S., H.-G. J., and M. Z.; writing—original draft preparation, A. A., and M. Z.; writing, review and editing, A. A., C. S., H.-G. J. and M. Z.; visualization, A.A.; supervision, M. Z.; project administration, M. Z. and H.-G. J.; funding acquisition, M. Z., and H.-G. J.

I developed the co-culturing idea including chosen cell ratios and the associated laboratory protocol for fluorescence labeling of two cell types in one culture. C.S. contributed to fluorescent staining and performed image acquisition. I did the cell proliferation analysis including data interpretation and the major part of data processing and interpretation of the radial autocorrelation method. I did the nearest neighbor analysis and data interpretation. I prepared MEAs with cells for electrochemical impedance spectroscopy which was then performed by H.-G.J. I wrote the manuscript and produced the graphics in the manuscript.

Collaborations

Atomic Force Microscopy: Dr. Thomas Fuhs provided valuable feedback on single-cell force spectroscopy measurements to me. Dr. Ronny Frank performed AFM imaging of the surfaces of the electrode materials at the BBZ for me.

Electrochemical Impedance Spectroscopy: Heinz-Georg Jahnke performed electrochemical impedance spectroscopy measurements at the BBZ after I prepared the multielectrode arrays in cell culture at the Peter Debye Institute. He provided support for data analysis and interpretation for these measurements.

Electrode Materials: Dr. Sabine Schmidt produced the electrode material substrates for me at the BBZ in Leipzig.

Algorithm Development: Chelsie Steele wrote a major part of the algorithm of K-means cluster analysis for me. She also contributed to data analysis of the spatial cell distributions.

Supervision and Institutes

My PhD thesis was supervised by Prof. Mareike Zink at the Peter Debye Institute for Soft Matter Physics at Leipzig University. My work was part of a collaborative project with the Molecular Biological-Biochemical Processing Technology group at the Centre for Biotechnology and Biomedicine (BBZ) in Leipzig. This thesis was developed in collaboration with Prof. Josef A. Käs at the Peter Debye Institute. I used his cell culture lab, chemistry lab, the Cell Hesion AFM, and the spinning disk microscope for fluorescence imaging.